THE UNIVERSITY OF CALGARY

Improvement of SPECT using Radionuclide Transmission Attenuation Maps

by

Damini Dey

A DISSERTATION

SUBMITTED TO THE FACULTY OF GRADUATE STUDIES

IN PARTIAL FULFILMENT OF THE REQUIREMENTS FOR THE

DEGREE OF DOCTOR OF PHILOSOPHY

DEPARTMENT OF PHYSICS AND ASTRONOMY

CALGARY, ALBERTA

MAY, 1998

National Library of Canada
Acquisitions and Bibliographic Services
395 Wellington Street
Ottawa ON K1A 0N4
Canada

Bibliothèque nationale du Canada
Acquisitions et services bibliographiques
395, rue Wellington
Ottawa ON K1A 0N4
Canada

Your file Votre référence

Our file Notre référence

0-612-34667-6

Canada

ABSTRACT

The diagnostic accuracy of Single Photon Emission Computed Tomography (SPECT) is limited by physical effects such as photon attenuation and scatter, and the lack of anatomical reference corresponding to the SPECT images. Since the heart is surrounded by organs of varying density, attenuation correction in cardiac SPECT, in particular, requires measured attenuation maps. These are commonly obtained by radionuclide transmission (RNT) imaging, using transmission line sources. The goal of this work is to critically evaluate different methods and approaches to improve SPECT images corrupted by non-uniform attenuation and scatter, using RNT attenuation maps. Another objective is to evaluate unconventional use of RNT attenuation maps, in the integration of SPECT with anatomical CT data.

SPECT scans simulating normal and defect myocardial studies of an anthropomorphic phantom were acquired. X-ray CT images and RNT attenuation maps of the phantom were also obtained. The effect of using Ordered Subsets Expectation Maximization (OSEM) and Chang's attenuation correction was quantitatively compared using this data. The effect of using attenuation maps obtained from poor quality RNT images, acquired using a transmission flood source, to using CT and scanning transmission line source attenuation maps, was also quantitatively compared. To perform these comparisons, it was necessary to register the SPECT and CT images. A novel, fully automated method for three-dimensional registration of SPECT and CT images, utilizing RNT attenuation maps, was used in this thesis. This image registration method was evaluated and found to be comparable to registration using fiducial markers.

OSEM and Chang's attenuation correction are found to be quantitatively equivalent, with comparable calculation times. However, OSEM attenuation correction provides a more correct radiotracer distribution and is, therefore, preferred. Attenuation maps obtained from poor quality RNT images are comparable to CT and scanning transmission line source attenuation maps, and can be used in cardiac SPECT without significant loss in quantitative accuracy. In addition, RNT attenuation maps can be utilized for robust, automatic three-dimensional SPECT-CT registration. This registration method is independent of features or quality of the SPECT images and avoids difficulties

associated with fiducial markers. It can potentially be extended to SPECT imaging of various organs.

ACKNOWLEDGEMENTS

This thesis would not have been possible without the active help and support of several individuals and I would like to thank them. To begin with, I would like to thank Dr. L. J. Hahn for his help throughout this project. I would like to thank Dr. R. Kloiber for discussing and pointing out the clinical perspectives of my research, and Dr. J. S. Murphree for his advice and support. Thanks to Dr. C. J. Bland for his help over the years. Thanks also to the staff of the departments of Nuclear Medicine, Nuclear Cardiology and CT at Foothills Hospital who assisted me in several ways. I would like to give special thanks to Dr. Anna Celler at Vancouver Hospital, for shipping the anthropomorphic phantom to me, often at only 2 days' notice. My experiments would have been extremely difficult to perform and analyze if it had not been for this anthropomorphic phantom. I want to thank Richard Larkin his help with OSEM.

I would like to thank all my friends at Nuclear Diagnostics, of Stockholm, Sweden, for their help and advice. Special thanks to Jan Bertling for the use of a Pentium workstation with Hermes software on which most of my image analysis was done. It would be very difficult to analyze my images if it had not been for this software package. To Jan, Anders, Sue, Steve, and Jill – many thanks and a big skol! Thanks to Peter and Mira Dey for their active help with my experiments. Thanks to Lynne for her help in literature searches. Special thanks to Piotr for all his help.

Finally, I wish to thank friends and family, without whom I would not have survived the last five years; to my parents, Lynne, Joyoni and Rukmini, Piotr, Eshamashi, Manjumashi, Dragana and her family, Peter and Paulette, Hannah, Anne-Lise, Maria, Anurag, Koushik, Suchitra, Janice, and Tazman – my everlasting gratitude. I would like to dedicate this thesis to my parents with the following words of the great Bengali poet Rabindranath Tagore:

amar mukti aloy aloy ei aakashe
Amar mukti dhulai dhulai ghashe ghashe ...
Jibon jeno dii ahuti mukti aashe.

TABLE OF CONTENTS

LIST OF TABLES

LIST OF FIGURES

LEGEND OF ACRONYMS AND SYMBOLS

SPECT	Single Photon Emission Computed Tomography
PET	Positron Emission Tomography
MRI	Magnetic Resonance Imaging
CT	Computed Tomography
3-D	Three-dimensional
CAD	Coronary Artery Disease
TCT	Transmission Computed Tomography
MLEM	Maximum Likelihood Expectation Maximization
OSEM	Ordered Subsets Expectation Maximization
Tc-99m	Technetium-99m
Tl-201	Thallium-201
PMT	Photomultiplier tube
ADC	Analog-to-digital Converter
FBP	Filtered Backprojection
FOV	Field-Of-View
TEW	Triple Energy Window
TDCS	Transmission Dependent Convolution Subtraction
RCA	Right Coronary Artery
RNT	Radionuclide transmission
TLS	Dual scanning transmission line source attenuation map
TFS	Transmission flood source attenuation map
CTFILL	Segmented CT attenuation map
TFSFILL	Segmented TFS attenuation map
UNIF	SPECT study simulating normal myocardium
DEF25	SPECT study simulating RCA defect with contrast 75%
DEF50	SPECT study simulating RCA defect with contrast 50%
DEF75	SPECT study simulating RCA defect with contrast 25%
ARM	Average Radial Maximum
MDC	Maximum Defect Contrast

CHAPTER 1: INTRODUCTION

1.1. Introduction

Clinical diagnosis, and planning and evaluation of surgery or therapy, are often supported by several medical imaging modalities. Different modalities usually provide complementary information. Examples of such modalities are X-ray Computed Tomography (CT), Magnetic Resonance Imaging (MRI), Ultrasound (US) and Nuclear Medicine. Nuclear Medicine is a medical imaging technique which uses a variety of radioactively tagged agents (radiopharmaceuticals) to image the human body and treat diseases. In contrast with imaging techniques such as Computed Tomography (CT) or Magnetic Resonance Imaging (MRI), which are primarily based upon anatomy, Nuclear Medicine imaging depicts organ function and structure. It may provide medical information that may otherwise be unavailable, require surgery, or necessitate more expensive diagnostic tests. It can cost-effectively provide unique information about both the function and structure of most organ systems within the body. For example, Nuclear Medicine can be effectively used in staging and detection of cancer, in brain imaging for diagnosing psychiatric disorders and epileptic seizures, for diagnosing coronary artery disease, gastro-intestinal disorders, and for assessing lung function and renal function. There are approximately 12-13 million nuclear medicine imaging and therapeutic procedures performed each year in North America, with the number of cardiac scans per year ranging from 1 to 2 million.

Nuclear medicine images are formed by photons emitted from a radioisotope detected by a scintillation camera (gamma camera) or Positron Emission Tomography (PET) camera. The scintillation camera is an imaging device that detects and spatially registers gamma rays. It consists of a collimator, a large NaI(Tl) crystal coupled to an array of photomultiplier tubes, and associated electronics. Like other radiation detectors, it detects emitted photons within a preset energy window; however, the scintillation camera also records the position of the emission event. Thus, the images indicate both the distribution and projected radioactivity in the organ. Planar (two-dimensional) or three-dimensional (tomographic) distribution of the photons can be obtained using the scintillation camera.

Tomographic distribution of the photons are obtained by acquiring a series of two-dimensional images (projections) from several angles around the patient. This technique is called Single Photon Emission Computed Tomography (SPECT). The scintillation camera rotates around the patient and acquires the projections at several angles. The acquired projections are reconstructed using mathematical algorithms to obtain a stack of transverse images. Tomographic images can be also obtained with a PET camera.

The quality of SPECT images is limited by several physical phenomena and detector characteristics. The images are of relatively low resolution (typically 9-15 mm), due to imperfect collimation of the detected photons, Compton scatter of photons in the patient and intrinsic limitations of the gamma camera. Only a small number of photons are used to create the images and the distribution of such photons is governed by Poisson statistics. Therefore, the images are noisy. Typical photon energies useful in nuclear medicine are in the range of 70 keV to 511 keV. Prior to being detected, the emitted photons can be attenuated and scattered in the body. The primary cause of these physical effects is photon interaction with body tissue via Compton scatter and photoelectric absorption [1]. Attenuation of the emitted photons depends on the imaging geometry and attenuating properties of the body, as well as the relative position of the photon emitting organ, which is not known without performing additional measurements. Attenuation and scatter introduces artifacts to the reconstructed images. The images are often difficult to interpret because of these degrading effects, and because of the lack of anatomical reference corresponding to the SPECT images. Thus, improving image quality is of primary importance in the interpretation of Nuclear Medicine images and for clinical diagnosis.

SPECT imaging of the heart is a widely-used procedure for diagnosing coronary artery disease. In cardiac SPECT, attenuation is inhomogeneous since the heart is surrounded by tissues with various attenuating properties such as lungs, bones and muscle. Attenuation artifacts in cardiac SPECT images are especially detrimental since they can confound clinical diagnosis. Reduction of such image artifacts is therefore of primary importance. The extent, severity and location of such artifacts varies from patient to patient as a function of the anatomy. Therefore, correction for attenuation in cardiac SPECT requires patient-specific anatomical information.

Improvements to the standard SPECT imaging system have been proposed, which allow acquisition of an additional set of anatomical images during the same imaging session. These images can define the three-dimensional distribution of the photon attenuation coefficients in the patient body. This is most typically accomplished by acquiring images of another radioisotope, which is placed outside of the patient. The fraction of the photons transmitted through patient body is imaged by the gamma camera positioned on the other side. Such images, analogous to standard X-ray images, are acquired from several angles in a tomographic mode. These measurements allow the estimation of a map of attenuation coefficients in the patient, called radionuclide transmission (RNT) attenuation maps. Such measured attenuation maps can be then incorporated in mathematical algorithms that reconstruct the emission image, to correct for non-uniform photon attenuation through the body. Several issues arise in implementing this technique clinically, such as the additional time, cost and complexity of the imaging procedure, the need for new imaging hardware, the accuracy of correction and the clinical impact of such correction.

Non-uniform attenuation correction of SPECT images has been the area of intense research over the last few years. Many designs of such imaging systems have been proposed and there is currently no consensus with respect to established protocols for acquisition of such images. Similarly, various mathematical attenuation correction and image reconstruction algorithms have been developed. In particular, the trade-off between faster and simpler image acquisition and reconstruction methods and image accuracy is an important issue. In addition, the simultaneous availability of patient attenuation maps corresponding to anatomy offers new possibilities of improving the clinical value of SPECT imaging, beyond typical use for non-uniform attenuation correction.

In this thesis, I am exploring some of the current approaches and methods used in non-uniform attenuation correction for cardiac SPECT. Using images of a human-like phantom, I quantitatively compare two non-uniform attenuation correction methods. The results of the comparison would establish if both attenuation correction methods are equivalent, or if one is superior to the other. I also compare attenuation maps obtained from poor quality radionuclide transmission images to higher-resolution X-ray CT and

transmission line source attenuation maps. The results of such a comparison would establish if poor quality attenuation maps can be used without significant loss in quantitative accuracy. In addition, I utilize transmission attenuation maps for mapping the SPECT images to anatomical CT images. Such merging of functional and anatomical images is important in clinical diagnosis, as well as evaluation of surgery or therapy. Several methods to perform such mapping have been proposed, but they are either specific to the type or quality of SPECT scan, or require external markers or stereotactic frames, which may not be clinically feasible.

1.2. Thesis objective

Attenuation correction in cardiac SPECT requires patient-specific attenuation maps, which are commonly obtained by radionuclide transmission imaging. The objective of this thesis is to critically evaluate different methods and approaches to improve SPECT images corrupted by non-uniform attenuation and scatter, using radionuclide transmission attenuation maps. An additional objective of this thesis is to evaluate unconventional use of radionuclide transmission attenuation maps, in the integration of SPECT with anatomical CT data. Based on these two principal objectives, this thesis is divided into two parts.

More specifically, an aim in the first part of this thesis is to quantitatively compare the effect of using OSEM (Ordered Subsets Expectation Maximization) and Chang's attenuation correction method in cardiac SPECT. Chang's method is a widely used post-reconstruction attenuation correction method. OSEM is a recently-proposed accelerated iterative reconstruction method, based on the well-known MLEM (Maximum Likelihood Expectation Maximization) algorithm. Both methods have been described in Chapter 2. Another specific objective in the first part of this thesis is to quantitatively compare the effect of using attenuation maps obtained by a simplified method, from poor quality radionuclide transmission images, to using attenuation maps obtained from X-ray CT and scanning transmission line sources. Although not used in routine clinical practice, attenuation maps obtained from X-ray CT images have the best spatial resolution. In clinical practice, attenuation maps are usually obtained using scanning or stationary

transmission line sources. Acquiring such maps requires additional transmission imaging hardware and can complicate the acquisition procedure. Methods used to estimate attenuation maps are reviewed in Chapter 3.

To perform these quantitative comparisons, it is necessary to co-register (or map) the SPECT and X-ray CT images to common spatial data co-ordinates. The second part of the thesis addresses co-registration of images obtained from different modalities. The aim of the second part of the thesis is to evaluate a novel, fully automated method for three-dimensional registration of SPECT and CT images, using radionuclide transmission attenuation maps. Automatic volume registration using two convergence criteria are compared to manual landmark-based registration using markers. The method proposed in this thesis is independent of abnormal features or quality of the SPECT images; it also avoids difficulties associated with the use of external markers and stereotactic frames. It can potentially be extended to SPECT imaging of a wide range of organs.

1.3. Original contributions of this thesis

Several problems studied in this thesis have not been reported before in the literature. The quantitative comparison of OSEM attenuation correction with Chang's method, using CT attenuation map, is new. The quantitative comparison of the effect of using poor quality radionuclide transmission attenuation maps to using X-ray CT and scanning transmission line source attenuation maps is also new. In addition, this thesis proposes a novel automated method for 3-D image registration, which is potentially applicable to SPECT imaging of various organs.

1.4. Thesis Outline

Chapter 1 is a general introduction to the thesis. The objectives of this dissertation have been described in the preceding section. Chapter 2 describes the basic physical principles behind SPECT imaging. In this chapter the basic principles of the scintillation camera are described, and an overview of commonly used reconstruction techniques is

presented. Common non-uniform attenuation correction techniques are described, and a review of scatter correction methods is presented.

The thesis is then organized into two parts, corresponding to the two principal objectives of this dissertation. The first part addresses the use of attenuation maps in quantitative myocardial perfusion SPECT imaging. In the first part, Chapter 3 describes the technical aspects of quantitative myocardial perfusion SPECT. This chapter describes methods used to acquire and process myocardial perfusion images; and presents a review of methods of estimating attenuation maps. Chapter 4 presents a comparison of OSEM attenuation correction with Chang's attenuation correction method. Chapter 5 presents a comparison of poor quality RNT attenuation maps acquired using a transmission flood source to attenuation maps obtained using X-ray CT and scanning transmission line sources. In the second part, Chapter 6 describes the basic principles of correlative image registration. A review of image registration methods is presented in this chapter. Chapter 7 presents an evaluation of a fully automated method for 3-D image registration of CT and SPECT, using radionuclide transmission attenuation maps. An overall discussion and conclusions of this dissertation are provided in Chapter 8. The implications of this research for patient studies are discussed, with directions for future work.

CHAPTER 2: BASIC PHYSICAL PRINCIPLES OF SPECT IMAGING

2.1. Radioisotopes used in Nuclear Medicine

In Nuclear Medicine imaging, a pharmaceutical labeled with a radioisotope is administered to the patient. The most commonly used radioisotope in Nuclear Medicine is Technetium –99m (Tc-99m), a metastable state of Tc-99. Tc-99m decays to Tc-99, by emitting gamma rays of 140 keV. The half-life of Tc-99m is 6.0 hours. Tc-99m is widely used in Nuclear Medicine because of its low energy, short half-life and ready availability. Tc-99m can be obtained from Molybdenum-99 (Mo-99) generators, which are shipped from a nuclear reactor to the nuclear medicine department on a regular basis [2]. Another radioisotope often used in cardiac imaging is Thallium-201 (Tl-201), which emits k-shell x-rays between 69 and 83 keV, and gamma rays at 167 keV. Tl-201 has a half-life of 72 hours. Other commonly used radioisotopes include Iodine-123 (I-123), Iodine-131 (I-131), Gallium-67 (Ga-67), Indium-111 (In-111).

The physical principles of SPECT imaging, and mathematical techniques for SPECT reconstruction and attenuation correction have been described in this chapter. Only the most commonly used techniques have been described in detail.

2.2. Basic principles of the scintillation camera

The first imaging device in Nuclear Medicine was a rectilinear scanner, which consisted of a single-bore collimator coupled to a gamma ray detector. The rectilinear scanner had to perform a raster scan over the patient to obtain a planar image. The scintillation camera, an instrument that detects and spatially registers gamma rays, was first introduced in 1958 by Anger at the University of California [3]. The invention of the gamma camera revolutionized nuclear medicine, because of its ability to perform rapid dynamic imaging. Since then, scintillation camera design has evolved significantly due to improvements in technology and the integration of analog and digital circuitry.

Fig. 2.1 illustrates the principles of operation of the scintillation camera. The radiation detector in the scintillation camera consists of a large NaI(Tl) scintillation crystal, coupled to an array of photomultiplier (PMT) tubes. A collimator is positioned between the radionuclide, which emits photons (gamma rays) and the scintillation crystal. Collimators are needed to relate the sites of photon absorption in the crystal to their origin in the patient. They are usually made of lead alloys or tungsten. Gamma rays parallel to the collimator holes pass through the collimator and interact with the scintillation crystal; other photons are absorbed in the collimator's septa (walls separating two collimator holes). The most common used type is the parallel-hole collimator, which is used for general-purpose imaging, especially for larger organs. Other commonly used collimators include fan-beam and pinhole collimators.

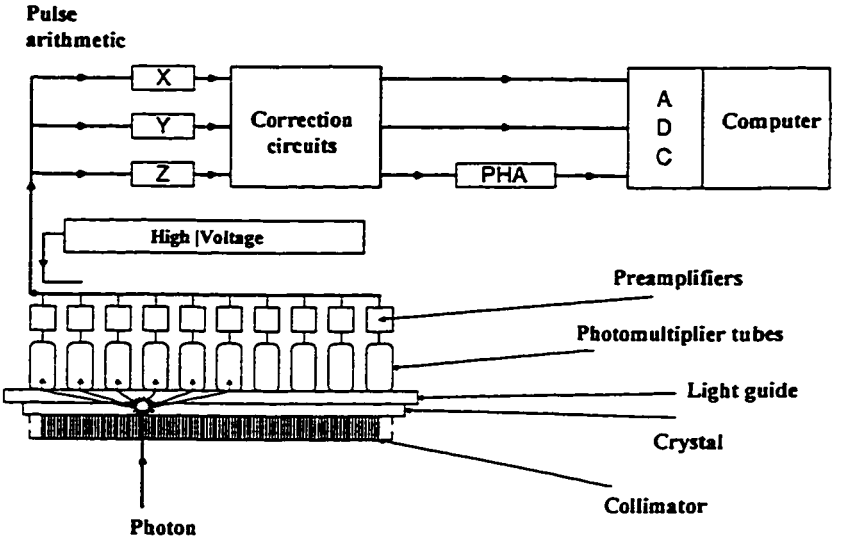

Fig. 2.1. Schematic diagram of a scintillation camera. Reproduced with permission from reference [4].

The NaI(Tl) scintillation crystal absorbs gamma rays that passed through the collimator and re-emits their energy as visible light (scintillation). The light intensity of each scintillation event is proportional to the energy of the incident photon. NaI(Tl) is used

because it provides high gamma ray absorption and scintillation efficiency via photo-electric effect. NaI(Tl) crystals are produced in several diameters at thicknesses of 0.63 cm (1/4 inch) to 1.3 cm (1/2 inch). Thicker crystals have better absorption, but have a greater tendency to diffuse light and increased Compton scatter.

The crystal is optically coupled at its back surface to an array of PMTs. Between 19 to 91 PMTs are arranged in the array. Each scintillation event is registered by several PMTs, with the PMTs close to the event receiving more light. The PMT converts the light signal to an electrical signal proportional to the amount of incident light. The electrical signal from each PMT is transmitted to a separate pre-amplifier. The gains of the PMTs are monitored and adjusted periodically so that each PMT provides the same response to similar light pulses [2, 5-7].

The amplified electrical signals pass through a resistor matrix which encodes the response of the PMT array as X,Y spatial position signals. The amplified current pulses from the PMT array are summed to form the Z signal or the energy signal. The Z signal is proportional to the energy deposited in the crystal by the incident gamma ray. The X, Y position signals are normalized by the amplitude of the Z signal. This normalization must be done; otherwise, the size of the X,Y position signals for low-energy gamma-emitting radionuclides (such as Tl-201), which generate smaller amounts of light per scintillation event, would be smaller than the position signals for higher-energy gamma emitters (such as I-131, which emits gamma rays at 364 keV). This would result in a smaller image for lower energy gamma-emitting radionuclides [2]. Normalization for energy also allows image acquisition in two or more energy windows [2]. The energy signal, Z, is passed to the pulse-height analyzer (PHA), which classifies the signal according to preset energy limits (energy window). The PHA is used to reject events generated by photons of undesirable energy, such as scattered photons, or photons emitted by other radioisotopes. Most scintillation cameras provide at least 3 non-overlapping energy windows. In many cameras, the X,Y and Z signals are adjusted by separate correction circuits for energy, linearity and uniformity [7]. In state-of-the-art cameras, digital correction methods to correct for such distortions are used.

All modern cameras are connected to a computer system. The X and Y signals are then passed through analog-to-digital converters (ADC) and finally to the computer, in which,

the software increments the count value at the appropriate image matrix position. Hardcopies of acquired images are often recorded on radiographic film.

2.3. SPECT imaging

Single Photon Emission Computed Tomography (SPECT) yields three-dimensional (3-D) images of radionuclide distributions. The gamma camera moves in a circular, elliptical or contoured orbit about the patient and acquires radionuclide images (or projections) from many angles. These multiple projections are subsequently reconstructed using mathematical algorithms and three-dimensional (3-D) images of radionuclide distributions are obtained (Fig. 2.2).

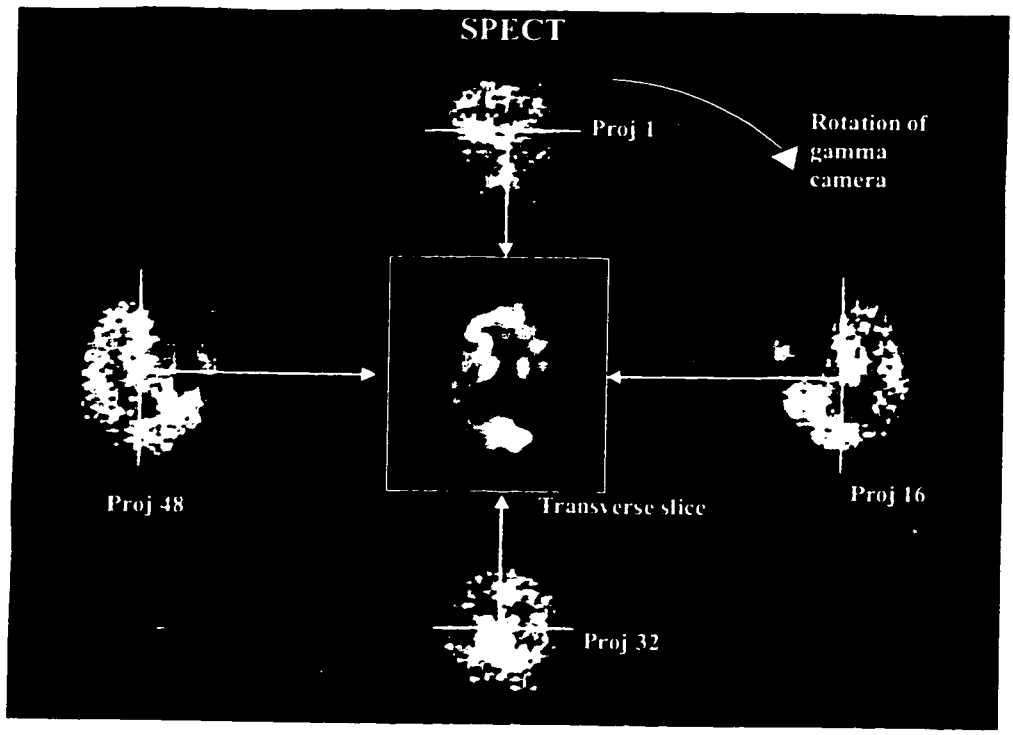

Fig. 2.2. Figure illustrating SPECT acquisition. This brain study was acquired at 64 projections over 360°.

2.4. Image reconstruction from projections

The analytic solution to the problem of calculating a 3-D distribution from 2-D projection data was first described by Radon in 1917 by an integral equation. Several mathematical approaches have been proposed to solve this problem. They can be broadly classified into analytical and iterative techniques. Some examples of analytical techniques are the Fourier reconstruction method and the filtered backprojection method. The most commonly used reconstruction technique in SPECT is the filtered backprojection (FBP) method, because of its speed and acceptable image quality [2, 8]. This method has been described in section 2.4.1. Although FBP has been used extensively, it has some inherent limitations. In many analytical reconstruction techniques such as FBP, it is assumed that each 2-D projection image is a sum of emitted photon intensities along a direction normal to the camera plane, or a ray sum of pixel intensities. This is incorrect. Photon attenuation through the body has a significant effect on the projections; to obtain a true activity distribution, correction for attenuation must be made [9]. Other effects that degrade SPECT images are scatter, and spatial resolution of the camera, which decreases with depth, and partial volume effect [2], which arises from the low spatial resolution. With FBP, therefore, additional correction for attenuation and scatter must be performed to obtain the true radioactivity distribution.

Many iterative techniques have been described for image reconstruction from projections. In general, a typical iterative reconstruction method consists of an underlying statistical model of the data acquisition, a projector/ backprojector pair which models the geometry and physics of the image formation, and a scheme for iteration. These techniques have the advantage that the effects of attenuation, scatter and depth-dependent spatial resolution can be directly incorporated into the weight matrix and the reconstruction algorithm [10, 11]. They also exhibit fewer streaking artifacts than FBP and can be applied to sparse projection data.

Of the proposed iterative methods, the Maximum Likelihood Expectation Maximization (MLEM) reconstruction method has been applied widely to SPECT, and with the most success [10]. The application of the Maximum Likelihood Expectation Maximization (MLEM) to medical imaging was developed independently by Shepp and

Vardi [12] and Lange and Carson [13]. The MLEM algorithm has been described in section 2.4.2. It assumes that radioactive emission is governed by Poisson statistics. As in other iterative reconstruction techniques, MLEM has the potential to incorporate a model of the emission and detection process. Though applied widely to SPECT and PET image reconstruction, until recently the reconstruction times for MLEM were too long for routine clinical use of the algorithm. In recent years strategies to accelerate the MLEM algorithm have been proposed, making it clinically feasible to use this algorithm [14]. Some other iterative reconstruction methods have also been applied to SPECT. A few implementations of weighted least squares conjugate gradient (WLS-CG) techniques have been reported [15-17]. The weighted least squares reconstruction method assumes a Gaussian noise distribution for radioactive emission. The function to be minimized in each iteration is a least-squares estimate [15]. In a comparison of MLEM and WLS-CG reconstruction methods for SPECT, Tsui et al [15] have found that the WLS-CG algorithm converges about ten times faster than MLEM. However, WLS-CG shows increased noise at higher iterations [15-16]. To reduce noise and smooth the reconstructed images, Fessler has introduced a penalty function within the reconstruction [18]. This penalized weighted least squares reconstruction technique have been applied to PET [18], SPECT and transmission data [19].

2.4.1. Filtered Back-Projection (FBP)

In filtered backprojection, as the name suggests, there are two operations applied to the projection data, filtering and backprojection. The projections are first pre-filtered by a deconvolution filter. This is a ramp filter, whose frequency response rises linearly up to some frequency cutoff. The ramp filter is used to remove the foggy blur caused by the backprojection step. The counts in each projection bin are then backprojected along a ray perpendicular to the gamma camera plane. The backprojection step is illustrated in Fig. 2.3. Each pixel in the reconstructed slice is formed by adding the ray sums from all projections that pass through that pixel (Fig. 2.3).

The ramp filter, by its very definition, amplifies noise at high spatial frequencies. For this reason, the ramp filter is usually modified by a smoothing window function, for

example, a Butterworth, Parzen or Shepp-Logan window [9]. Although the use of the window reduces noise, it also smoothes the image, which results in loss of spatial resolution. The cutoff frequency has to be chosen such that there is a compromise between noise reduction and loss of spatial resolution.

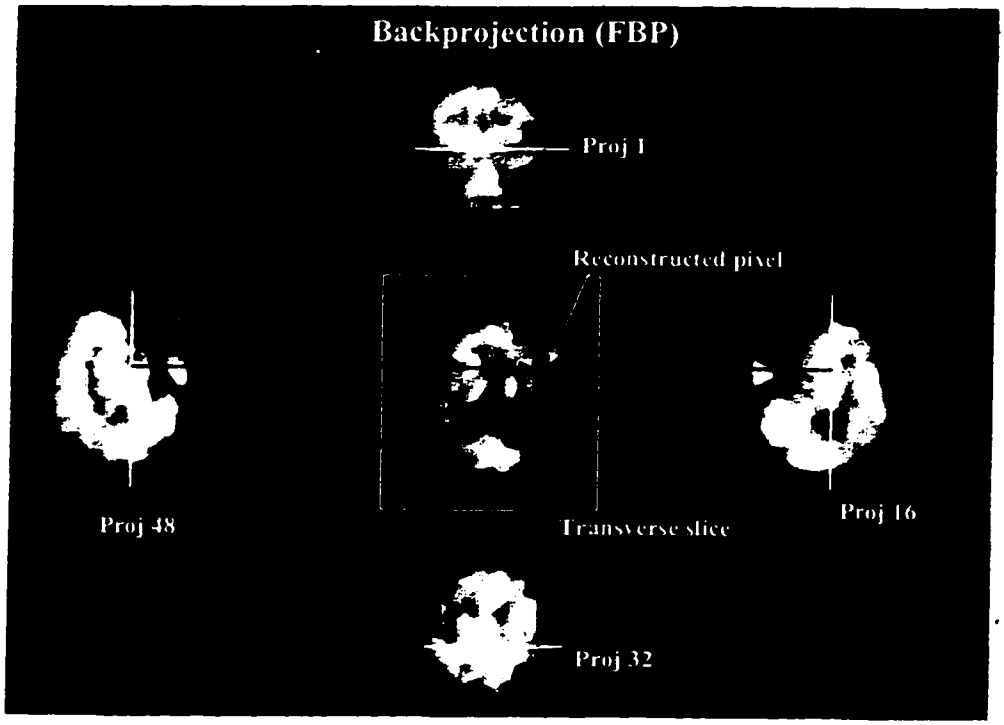

Fig. 2.3. Figure illustrating the backprojection step in filtered backprojection reconstruction. All projections are backprojected, only 4 projections are shown in this figure.

2.4.2. Maximum Likelihood Expectation Maximization (MLEM)

In matrix formulation, the problem in image reconstruction from projections is to solve

$$P = WI \qquad (2.1)$$

where P is the measured projections, I is the source activity distribution, and W is a matrix of weights, computed for a given imaging geometry, whose elements describe the contributions of each pixel to the measured ray-sum. These elements represent the probability of detecting a photon emitted from a given pixel by a given detector element and can include effects of source-dependent attenuation, scatter and depth-dependent spatial resolution.

Equation (1) can be re-written as:

$$P_j = \sum_{i=1}^{N} w_{ij} I_i \qquad (2.2)$$

where I_i is the source intensity of pixel i, P_j is the counts in projection bin j, and w_{ij} is the probability that a photon emitted at source point i will be detected at projection position j.

Fig. 2.4 shows a flow-chart for the MLEM reconstruction algorithm. The MLEM algorithm is an iterative process, with each iteration consisting basically of two steps. First, based on the source-detector geometry and the measured attenuating properties of the patient, the weight matrix is computed, and an initial estimate of the source activity distribution is assumed. This initial source activity distribution is often a uniform image or the image obtained by filtered backprojection reconstruction of the projections. The first step in the algorithm (often referred to as the E step or the forward projection step) determines the expected projections by forward projecting the current estimate of the source activity distribution using the weight matrix. The difference between the expected and measured projections is calculated. The second step (often called M step or the backprojection step) minimizes this difference to calculate a new estimate of the activity distribution. This is done by maximizing the logarithm of a statistical function called the likelihood function. For MLEM, the likelihood function is based on the Poisson noise distribution. The new difference in projections, found by maximizing this log-likelihood function, is then backprojected using the weight matrix, and the reconstructed image is updated. As the algorithm progresses to a more accurate estimate of the activity distribution we would expect the estimated projections to get closer to the measured projections.

The final solution is given by [13]:

$$I_i^{k+1} = (\sum_{j=1}^{N_p} w_{ij})^{-1} I_i^k \sum_{m=1}^{N_p} P_m w_{im} (\sum_{l=1}^{N_s} I_l^k w_{lm})^{-1} \qquad (2.3)$$

where I_i^k is the ith pixel of the estimated source distribution at iteration k, N_p is the total number of projection elements, N_s is the total number of source elements.

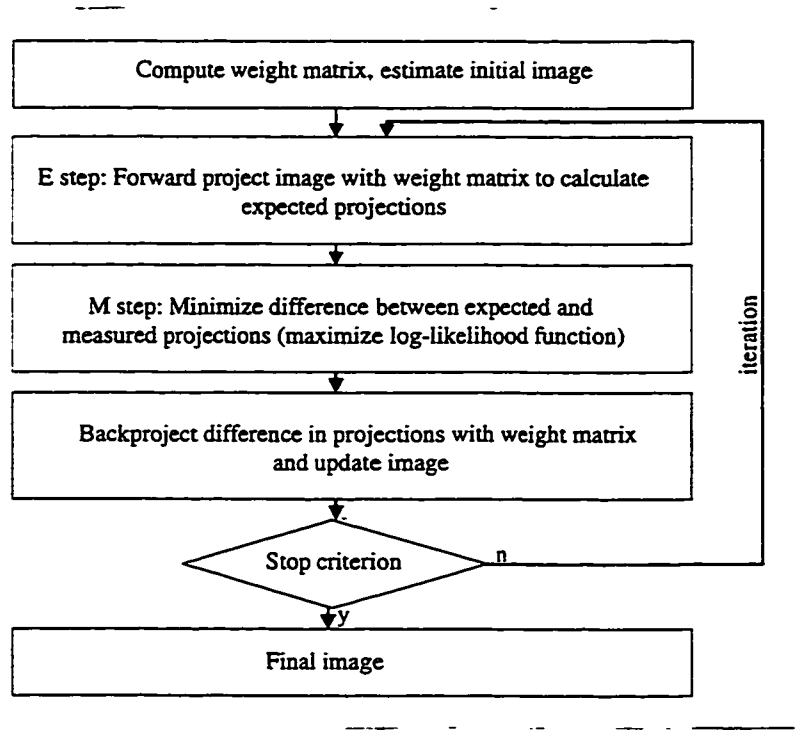

Fig. 2.4. Flowchart of the MLEM algorithm.

For real imaging situations, a noise contribution must be included in Equation 2.1. For noisy data which is typical for SPECT, there is usually a compromise between the recovery of fine detail in the reconstructed image, which improves with iteration, and noise, which also increases with the number of iterations. It has been shown that as the MLEM reconstruction passes a certain number of iterations, the reconstructed images begin to deteriorate due to noise [10-11]. How to control noise in MLEM reconstruction is a matter of current debate [10-11]. Suggestions to control noise include stopping the

algorithm at an arbitrary number of iterations, use of a stopping rule to determine when to halt iteration, or the use of regularization (filters or noise penalty functions inside the reconstruction algorithm) [10-11, 20-23]. Clinical practice is to stop the reconstruction algorithm at a set number of iterations before the maximum likelihood solution is reached. The set number of iterations is usually between 30 and 100 [10, 22].

2.4.3. Acceleration of the MLEM algorithm by the use of Ordered Subsets

A few strategies have been suggested to accelerate MLEM reconstruction. Acceleration using ordered subsets, known as OSEM (Ordered Subsets Expectation Maximization), has been proposed by Hudson et al [14], and applied to SPECT and PET data [11, 24-25].

In OSEM, the projection data is divided into ordered subsets. Each subset contains a set of maximally separated projections. Suppose we consider a total of 64 projections, and 8 subsets. Table 2.1 shows a possible grouping scheme of such projection data into subsets. The standard MLEM algorithm is applied to each subset in turn. The resulting reconstruction becomes the starting estimate for the next subset. A single iteration through all the subsets involves an amount of computation equivalent to one iteration of MLEM, yet yields a reconstructed image similar to N iterations of MLEM, where N is the number of subsets used. The rate of convergence is almost identical to that using all the projections. There is, therefore, a significant speed improvement over conventional MLEM, typically a factor of 10 or more [14].

For OSEM to converge, a pre-requisite condition is that there be subset balance, i.e., the sum of counts of projections forming the subsets be equal for all subsets. In clinical practice this is met provided that the subset size is not too small. However, good quality reconstructions have been reported even in the subset size of two, where subset balance is not necessarily maintained [10, 14].

MLEM is a special case of OSEM with the number of subsets equal to 1. The ordered subsets approach is not confined to EM reconstruction only, it can be applied to other algorithms as well. Hudson et al [14] have applied this approach to Maximum-A-Posteriori (MAP) reconstruction.

Table 2.1. Ordered Subsets grouping for 64 projections

Subset number	Projections in subset
1	0 8 16 24 32 40 48 56
2	4 12 20 28 36 44 52 60
3	2 10 18 26 34 42 50 58
4	6 14 22 30 38 46 54 62
5	1 9 17 25 33 41 49 57
6	5 13 21 29 37 45 53 61
7	3 11 19 27 35 43 51 59
8	7 15 23 31 39 47 55 63

Other approaches have been proposed to accelerate MLEM reconstruction. Among them, the rescaled block iterative method described by Byrne [26] appears to be a more generalized method, with no requirement for subset balance. This method has been shown to converge for any choice of subsets; it reduces to OSEM when the subset balance condition holds.

2.5. Attenuation correction methods

Photon attenuation arises from the interaction of emitted gamma rays with body tissue, via Compton scatter and photoelectric absorption [1]. It causes an apparent relative decrease of activity in regions located deeper in the body. The attenuating tissue can be uniform, with the same linear attenuation coefficient, as for example soft tissue in the case of liver SPECT, or non-uniform, with varying attenuation coefficients, such as soft tissue, bone and lungs in the case of cardiac SPECT, and soft tissue and skull in the case of brain SPECT. Conventional attenuation correction methods in SPECT assume a constant uniform attenuation coefficient distribution. For the cardiac region, which contains tissues with markedly different attenuation coefficients, these methods prove to

be inadequate [27]. For cardiac SPECT, correction for attenuation requires obtaining patient-specific attenuation maps as well as some modifications to attenuation correction algorithms. Attenuation maps are usually obtained by additional transmission measurements. Methods of estimating attenuation maps have been described and reviewed in section 3.3.1 of this thesis. This section discusses commonly used attenuation correction algorithms, with special emphasis on their implementation in the case of non-uniform attenuating media.

Let us consider a monochromatic photon beam incident on and interacting with a material of thickness x. If N_0 is the number of incident photons, the number of photons transmitted through the material, N, is given by:

$$N = N_0 e^{-\mu x} \tag{2.4}$$

where μ is the linear attenuation coefficient of the material. The linear attenuation coefficient μ depends on the attenuating material, the energy of the incident photon beam, and the source-detector geometry. If both the source of the photons and the detector are well-collimated, the geometry and the linear attenuation coefficients are known as narrow-beam. However if the source and the detector are not well-collimated, the linear attenuation coefficients are not equal to the narrow-beam linear attenuation coefficients (for the same attenuator and photon energy); the imaging geometry and the linear attenuation coefficients are known as broad-beam. For Tc-99m photons, the narrow beam attenuation coefficient for water is measured to be 0.153 1/cm. For broad-beam geometry, the linear attenuation coefficient values depend on the amount of scatter, but in general is smaller. For water an effective broad-beam linear coefficient value is often taken to be 0.12 1/cm. For clinical imaging situations, since the imaged regions are distributed and include scatter, broad-beam values are more appropriate [28]. However, if scatter correction is performed, use of narrow-beam attenuation coefficients is common [29].

In cardiac SPECT, since the attenuating medium is non-uniform, the linear attenuation coefficient corresponding to each pixel may be different. For cardiac SPECT, therefore, attenuation correction algorithms for uniform media have to be modified to trace through each pixel. This is illustrated in Fig. 2.5. If C_o is the original number of photons in source element *(i,j)*, and C_j is the counts detected in projection bin *j*, the effect of attenuation can be described in equation 2.4. The ratio C_j/C_o , known as the transmitted fraction, is given by:

$$\frac{C_j}{C_o} = e^{\sum_{l=1}^{N_r} -\mu_{lj} d_{lj}} \qquad (2.5)$$

where μ_{lj} is the linear attenuation coefficient for source element *(l,j)* , d_{lj} is the distance through source element *(l,j)*, along the ray from source element *(i,j)* to projection bin *j* (Fig. 2.5). *l* increases along this ray and N_r is the number of pixels traced by this ray.

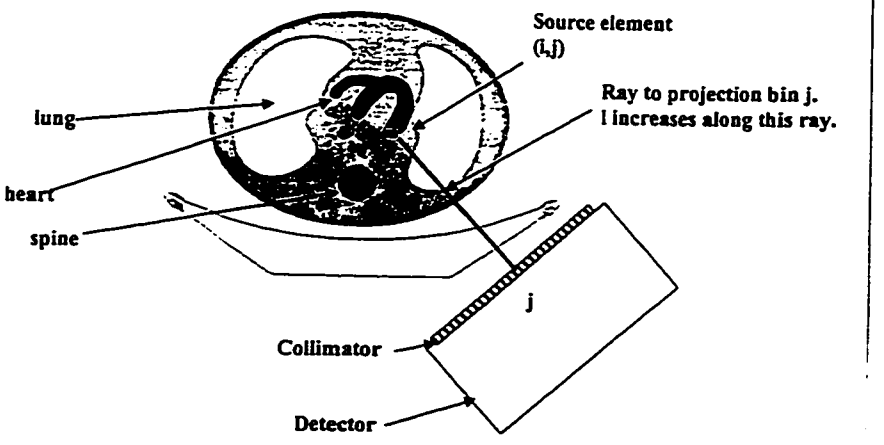

Fig. 2.5. Figure showing ray tracing for non-uniform attenuation in SPECT.

A number of algorithms have been developed for attenuation compensation. A few iterative attenuation correction algorithms have been used in conjunction with filtered back projection reconstruction [30-32]. When FBP is used, attenuation correction can be applied prior to reconstruction, such as the iterative pre-reconstruction technique proposed by Morizumi et al [32], or post-reconstruction, such as Chang's iterative method [30]. The effect of non-uniform attenuation can also be incorporated into the weight matrix for iterative statistically-based reconstruction techniques (such as MLEM and OSEM), or penalized weighted least squares or conjugate gradient reconstruction techniques [11-14, 17-18].

Chang's method is a post-reconstruction attenuation correction algorithm. It was initially proposed for uniform attenuating media [30], and later adapted for non-uniform attenuators [27, 31]. Chang's method has been illustrated in Fig. 2.6. Each pixel value in the reconstructed transverse image is multiplied by a correction factor. This correction factor is calculated as follows. For each pixel, the average transmission factor over all projections is calculated. The correction factor is the inverse of this average transmission factor. It is given by:

$$c_{ij} = \frac{1}{\frac{1}{N_p}\sum_{k=1}^{N_p} e^{\sum_{l=1}^{N_r} -\mu_{ij} d_{ij}}} \qquad (2.6)$$

where N_p is the total number of projections, and the other variables are as defined in equation (2.5). Since the average transmission factor is used, the correction is only approximate. Chang's method can be applied iteratively [30]. The corrected slices can be subsequently reprojected, and the resulting projections subtracted from the real projections. These "error" projections can be reconstructed using filtered backprojection and the attenuation correction algorithm applied again. The resulting image is added to the attenuation corrected image obtained from the previous iteration. Problems with convergence have been reported, however, and only one iteration is recommended [10]. The main advantage of Chang's method is its speed, which makes use of this algorithm clinically feasible [10, 27].

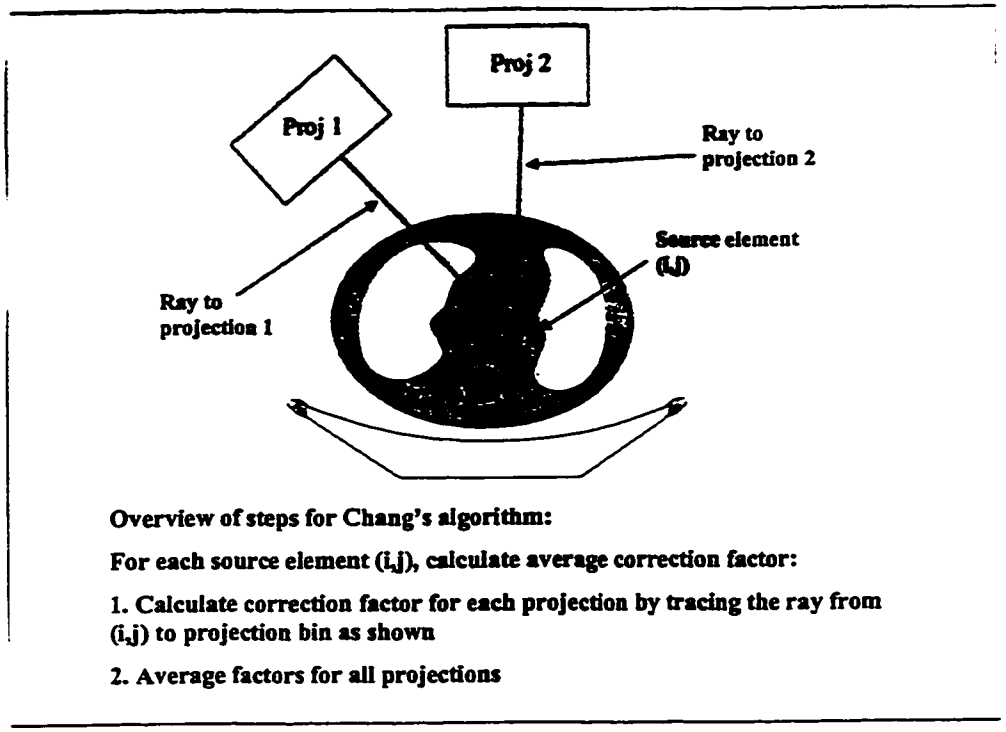

Fig. 2.6. Figure illustrating Chang's algorithm for non-uniform attenuation correction.

Morizumi et al [32] and Maze et al [31] have described an iterative pre-correction (IPC) algorithm for attenuation correction, which is applied prior to reconstruction on projection data. In this method, each projection bin is multiplied by a correction factor. For each projection bin, the average transmission factor through the attenuator is calculated. The correction factor is the inverse of the average transmission factor. The corrected projections are reconstructed using filtered backprojection. This method can also be applied iteratively, and the correction is also approximate. Maze et al [31] have shown that results and computation times for IPC and Chang's method are comparable. Chang's method was found to produce noisier images, and required one more iteration than IPC for similar image quality [31].

For iterative reconstruction techniques, such as MLEM or OSEM, the probability that a photon emitted at a given source point will be detected at a given projection bin is described by a number called a "weight" (equations 2.1-2.2). These weights are calculated based on known geometry and physical characteristics of the imaging system. The effect of attenuation can be incorporated into the weight matrix utilizing attenuation

maps, and attenuation correction performed during reconstruction. The correction is mathematically exact. The main disadvantage of MLEM are its long computing times, but as mentioned in Chapter 2, acceleration techniques and the increasing speed of current computers makes this less of a problem [10-11]. Tsui et al [27] have compared MLEM and Chang's method for a heart-lung phantom and a patient study. They found that MLEM provides a more correct radiotracer distribution, better anatomic object definition, fewer streaking artifacts and less noise.

In addition to these methods, analytical attenuation correction algorithms that solve the attenuated Radon transform have been reported. Examples of such algorithms are Bellini's method [33] and Tanaka's weighted backprojection method [34]. Bellini's method has been adapted for non-uniform attenuating media.

2.6. Scatter correction techniques

The energy resolution of a typical gamma camera is about 10-12% at 140 keV. At such energy resolution, a significant number of counts from scattered photons are included in the photopeak. The inclusion of scatter events reduces spatial resolution resulting in image blurring. Scatter degrades contrast of lesions and hence their detection, and biases quantitation of activity [35].

Several scatter correction techniques have been developed. For scatter correction, the amount of scatter has to be estimated on a pixel-by-pixel basis. Several investigators have estimated the amount of scatter per pixel by analyzing the entire energy spectrum: by statistical analysis [36], by factor analysis [37-38], or by polynomial fitting [39]. These methods have the common disadvantage that the images have to be acquired simultaneously in 10 or more energy windows. Since most gamma cameras can only acquire data in 3 or 4 energy windows, these methods cannot be implemented without extensive modifications to camera hardware.

Some investigators have used two or three energy windows to predict the amount of scatter per pixel. A widely used scatter correction method is dual energy window scatter subtraction, described by Jaszczak et al [35]. In this method projections are acquired in a lower scatter energy window in addition to the photopeak. A fraction of the counts in the

scatter window is subtracted from the photopeak projections. This fraction, k, is usually assumed to be 0.5. The difficulty with this method is the need to approximate the scatter fraction, which depends on the source size and density, with the constant default value of 0.5. Koral et al [40] have shown that while a constant scatter fraction is a good first approximation, for accurate quantification the scatter fraction has to be estimated on a pixel by pixel basis. Another widely used method is the Triple-Energy Window (TEW) technique, proposed by Ogawa et al [41]. This method utilizes 2 narrow scatter rejection windows on either side of the photopeak to estimate the amount of scatter for each pixel. The TEW method does not assume a fixed scatter fraction and can be implemented easily. However, the use of the narrow scatter rejection windows leads to a noisy scatter estimate [42]. For single-isotope studies with Tc-99m, a common technique to reduce noise in the scatter corrected images is to use the lower energy scatter window photopeak only [43-44]. King et al [42] have shown that applying low-pass filtering to the TEW scatter estimate decreases the normalized mean square error. Their investigation also shows that the incorporation of the scatter estimate directly into OSEM reconstruction results in a lower normalized mean square error than subtraction of the scatter estimate from the photopeak prior to reconstruction [42].

Axelsson et al [45] have described a convolution subtraction technique, in which the scatter contribution is estimated by a mono-exponential function with parameters that can be determined from experimental measurements of a line source in water. Meikle et al [46] have described an iterative scatter correction method called Transmission Dependent Convolution Subtraction (TDCS). This method is based on convolution subtraction and incorporates transmission data. An initial estimate of scatter is calculated by convolving the photopeak projections with a radially symmetric mono-exponential function. Transmission factors from attenuation maps are used to estimate the scatter fraction corresponding to each pixel. Such position-dependent scatter fraction values account for differences in the scatter fraction due to object size and density variations.

A comparison of nine scatter correction methods by Buvat et al [47] has shown that multi-energy factor analysis provides the most accurate scatter correction. This comparison also shows that dual energy window scatter subtraction offers the best compromise between accuracy and ease of implementation, and that the TEW method is

more accurate than dual energy window subtraction. A recent study comparing TDCS methods to the TEW method has shown that TDCS using the sum of a mono-exponential function and a Gaussian function provides greater accuracy [44]. The advantage of convolution subtraction techniques is that they are immune to the noise in emission data, and therefore are particularly applicable to low-count emission studies [44].

In a recent study, Iida et al [24] have applied non-uniform attenuation correction with TEW and TDCS scatter correction to I-123 IMP brain SPECT studies of 6 normal volunteers. Regional cerebral blood flow (rCBF) values were calculated from attenuation and scatter corrected SPECT images, guided by drawing regions of interest (ROI) on registered MRI images. SPECT rCBF values were compared to "gold standard" $H_2{}^{15}O$ PET rCBF values. They found that with appropriate attenuation and scatter corrections, excellent agreement could be achieved between I-123 IMP and PET rCBF values. The rCBF values for TEW and TDCS were found to be not significantly different, but the TEW method showed noisier images. This study showed that with scatter correction, assuming a uniform narrow beam attenuation coefficient for the brain shows little loss in accuracy. It also showed that scatter correction is required for the rCBF values and gray-to-white matter ratios to approach those of PET.

2.7. Depth-dependent spatial resolution compensation

In SPECT imaging, spatial resolution varies with depth (distance from the gamma camera) across the transverse slice. The objective of depth-dependent resolution compensation is, to improve resolution and more importantly, to improve the uniformity of resolution over the area of the myocardium [48-49]. Several compensation methods have been used. The effect of depth-dependent spatial resolution has been incorporated into the weight matrix in iterative reconstruction techniques [50]. The frequency distance principle has been used with analytical reconstruction techniques [51]. Use of the post-reconstruction depth-dependent Kalman filter in conjunction with filtered backprojection has also been reported [52].

2.8. The anthropomorphic phantom used in this thesis

An anthropomorphic phantom (Data Spectrum Corporation, Chapel Hill, North Carolina) with lung, cardiac and spine inserts was used in this work. SPECT measurements of the phantom were performed simulating uniformly distributed myocardial activity, as in a normal patient, as well as myocardium with defects (areas of decreased activity). To simulate uniform myocardial activity, the cardiac insert was filled with a known amount of radioactivity. To simulate defects, the cardiac insert was filled with a known amount of radioactivity, with corresponding amounts of activity in a fillable defect chamber. Fig. 2.7 shows a photograph of the phantom with the various inserts as well as the defect used. Several attenuation maps of the phantom were also acquired.

For clarity, the data and methods relevant to each chapter have been described in that chapter. The entire set of experiments performed is described in Chapter 5. The data in the other chapters are subsets of the data described in Chapter 5.

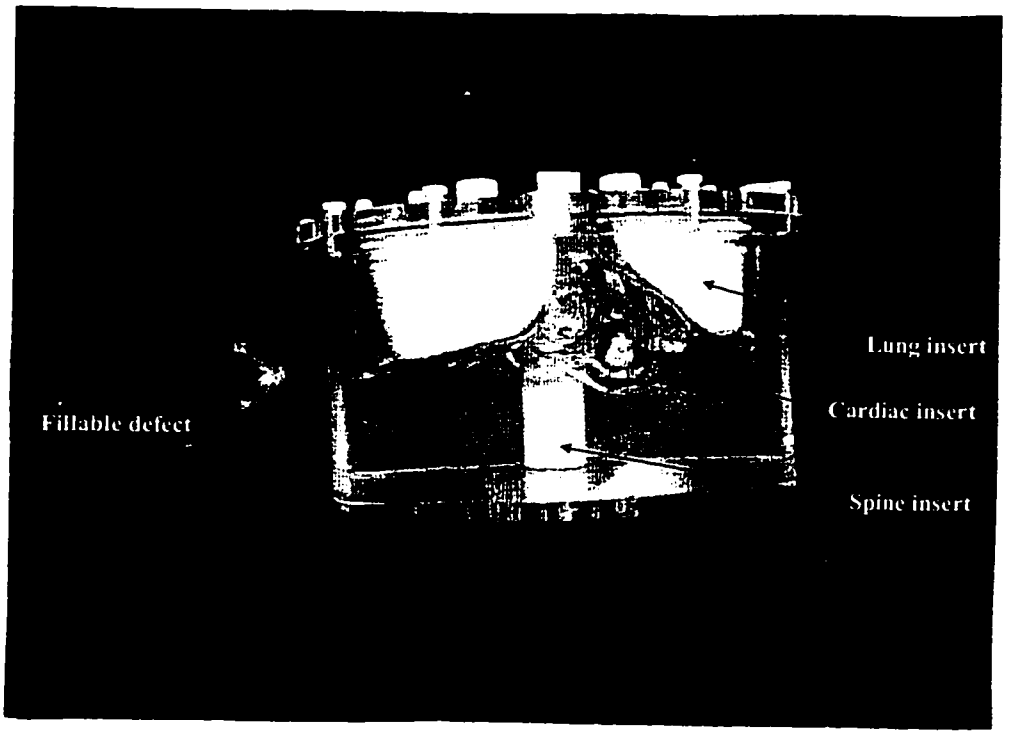

Fig. 2.7. Photograph of the anthropomorphic phantom used in this thesis.

PART I: ATTENUATION CORRECTION OF MYOCARDIAL PERFUSION SPECT

CHAPTER 3: QUANTITATIVE MYOCARDIAL PERFUSION SPECT IMAGING – a literature review

3.1. Myocardial Perfusion SPECT Imaging

Coronary artery disease (CAD), which is widespread in North America and Europe, is caused by narrowing or blockage of the coronary arteries. In a given patient, CAD may result in myocardial infarction (tissue damage) or transient myocardial ischemia (decreased blood supply). Symptoms of ischemia (chest pain on exertion) may be atypical and in some cases, absent. In the absence of resting ischemia, blood flow to the myocardium is normal when the patient is at rest. Under stress, however, there is an increased demand for oxygen, which requires increased blood flow. Normal vessels dilate, resulting in increased blood flow by a factor of 2-3 [53]. Diseased vessels cannot respond to the increased demand, and regions of the myocardium supplied by diseased arteries therefore show a relative decrease in myocardial perfusion. This decrease can be visualized using myocardial perfusion agents, which distribute proportional to blood flow. Myocardial perfusion imaging at stress and rest, therefore, provides valuable information towards diagnosis and prognosis of coronary artery disease (CAD) [54].

SPECT is a widely used and accepted technique for imaging myocardial perfusion. Myocardial perfusion SPECT images are acquired under stress and rest conditions. The heart is stressed either by symptom-limited treadmill exercise [55], or by using pharmaceuticals [56-58]. On myocardial perfusion images, the presence of a defect (area of hypoperfusion) can relate to either infarction or ischemia. Detection of a significant defect at stress, which is either absent or less severe at rest, indicates ischemia.

The "gold standard" test in the assessment and treatment of CAD is coronary angiography [59-60]. Coronary angiography is an imaging technique that uses X-rays and enables visualization of arteries after an intravascular injection of contrast material. It

requires cardiac catheterization. Angiography can accurately show vessel anatomy, including stenosis (narrowing of vessel). However, it is an invasive procedure with potential risks and complications [61] and is therefore warranted only when symptoms are severe. Myocardial perfusion SPECT can provide an objective method for non-invasive screening of patients. Since myocardial perfusion SPECT images perfusion at tissue level, it can also be used to evaluate if the myocardial tissue is viable (potentially salvagable), to assess the significance of borderline stenosis in coronary angiography, and to non-invasively assess treatment of CAD.

This review discusses current technical aspects of quantitative myocardial perfusion SPECT imaging, with special emphasis on attenuation correction.

3.1.1. Imaging agents and protocols

The most established agent for myocardial perfusion imaging is Thallium-201 (Tl-201) [55]. However, Technetium-based agents with better imaging characteristics (Tc-99m-sestamibi [62-63], Tc-99m-teboroxime [62, 64] and Tc-99m tetrofosmin) are also used routinely. Tc-99m based agents provide advantages over Tl-201. The main photon emissions for Tl-201 are at energies between 69 and 83 keV, and at 167 keV. Technetium-99m emits photons at 140 keV, which are more suited to the typical gamma camera, and also result in less scatter and attenuation. With Tc-99m, greater activity can be injected due to the shorter half-life (6 hours versus 3 days) [65]. As a result spatial resolution, count statistics and image quality are improved. Also, since most other Nuclear Medicine procedures are performed with Tc-99m, the radionuclide is readily available [62].

Since the myocardial kinetics of Tl-201 and the Tc-99m labeled agents differ from each other, imaging protocols also differ depending on the type of agent. The distribution of Tl-201 in the myocardium is not static but changes as a function of time. Following exercise, the initial accumulation of Tl-201 in the heart is proportional to regional myocardial blood flow and myocardial mass [66], and then it redistributes. The patient is

injected at stress. Stress images are acquired first, usually 10 minutes after exercise. Rest (or redistribution) images are acquired 3 to 24 hours later [55].

The distribution of Tc-99m-sestamibi is also proportional to regional myocardial blood flow and myocardial mass, however, it does not redistribute. Therefore two separate injections are required for stress and rest. Usually, a smaller dose is injected at rest and a larger dose is injected several hours later at stress [63]. In some clinics, the stress and rest studies are performed on two separate days. The 2-day stress-rest protocol consists of injecting the same dose for the stress study on day 1 and the rest study on day 2 [65]. Some researchers have developed dual isotope Tl-201/Tc-99m techniques to acquire rest and stress images simultaneously [67] or sequentially [68], which can potentially simplify the imaging protocol.

3.1.2. SPECT acquisition

SPECT acquisitions are usually performed over 180° orbit between right anterior oblique and left posterior oblique positions (Fig. 3.1). It has been argued that 180° acquisition shows improved spatial resolution and image contrast by avoiding high scatter and attenuation at posterior positions [69]. It has also been shown that geometric distortion due to attenuation, scatter and depth-dependent spatial resolution of the gamma camera is accentuated for acquisition over 180° compared with 360° [49]. The realtive merits of 180° versus 360° orbits are currently subject to debate [70]. LaCroix et al [71] have shown that if attenuation correction is performed, acquisition over 180° and 360° orbits are comparable for Tl-201 SPECT. Ficaro et al [72] have found no significant difference between 180° and 360° images of patients using Tc-99m sestamibi with respect to diagnostic accuracy or defect contrast. Standard acquisition parameters range from 32 to 64 projections, with each projection acquired for 20 to 30 seconds [65]. To improve count statistics and shorten acquisition time, improved gamma camera design such as orthogonal or L-shaped dual heads, or triple head systems are often used [73].

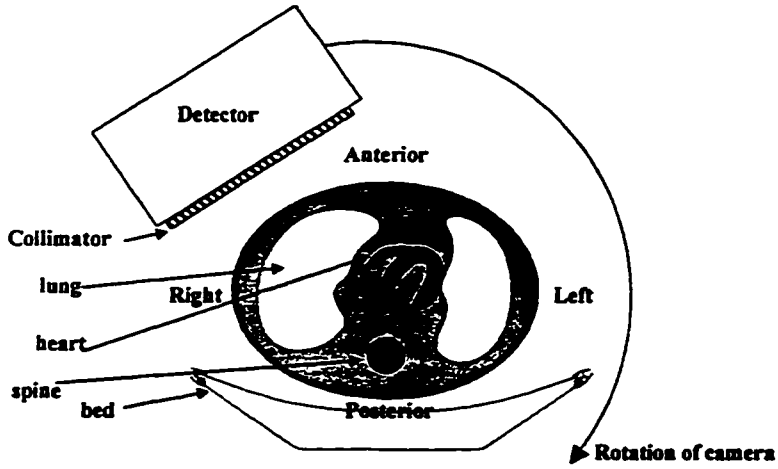

Fig. 3.1. Acquisition of myocardial perfusion SPECT over 180°.

3.1.3. Image processing

SPECT projections are usually reconstructed by a filtered backprojection algorithm into a stack of transverse planes. Depending on the capabilities of the software, various types of filters and reconstruction options are available. Separate optimization of reconstruction parameters for stress and rest studies is recommended because of the difference in count statistics [65]. The reconstructed images are reoriented into short-axis, horizontal long-axis and vertical long-axis views [74], orthogonal to the axes of the heart, to provide a standardized format for display and comparison of scans. Reorientation of the myocardium has been illustrated in Fig. 3.2.

In the last five years, significant advances have been made in the area of non-uniform attenuation correction, and such attenuation correction is now available from the gamma camera vendors as an option [75]. The requirements and methods for non-uniform attenuation correction in SPECT have been discussed in detail in Section 3.3. If

attenuation correction is performed on SPECT data, then attenuation corrected transverse images are reoriented into short axis, horizontal long axis and vertical long axis views, for visualization and quantitation in a standard format.

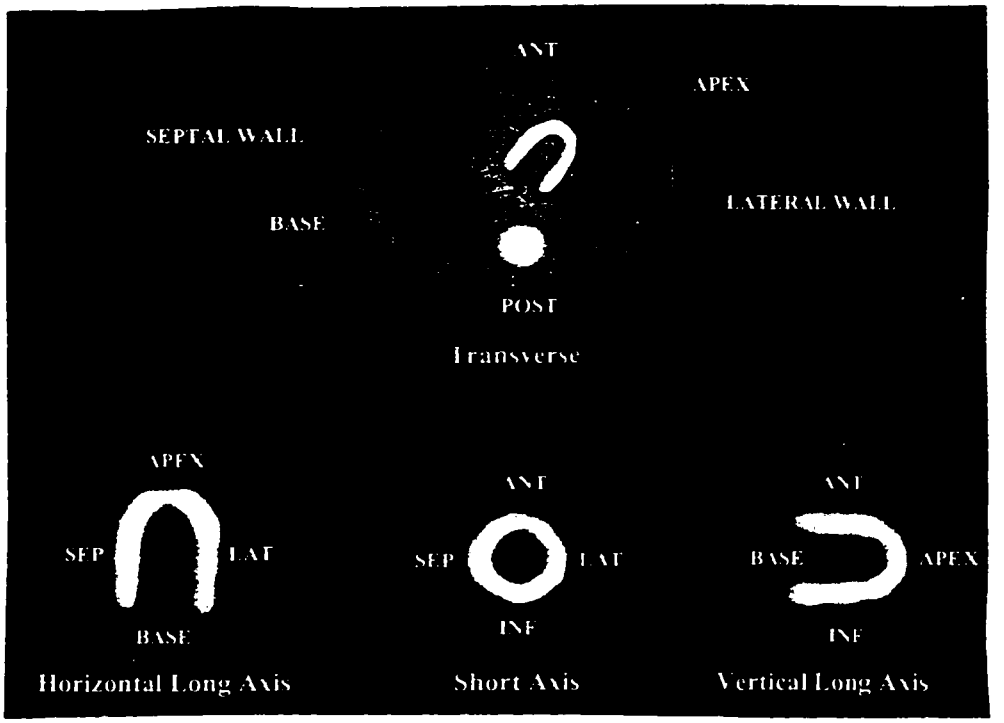

Fig. 3.2. Figure illustrating reorientation of the transverse slices of the myocardium into short axis, horizontal long axis, and vertical long axis views.

3.2. Limitations of myocardial SPECT

3.2.1. Attenuation and scatter

Photon attenuation and scatter are believed to be the most significant cause of image degradation and artifacts in myocardial SPECT [76]. Attenuation of photons causes a relative decrease of the observed activity in regions located deeper in the body. The contribution of scatter and attenuation increases from the apex to the base of the heart. Thus, hypoperfused regions in basal areas may be more difficult to detect. In both men

and women, diaphragmatic attenuation can result in lowered inferior wall activity [76]. This inferior wall attenuation artifact is illustrated in Fig. 3.3. Fig 3.3 shows images of the myocardial insert with uniformly distributed Tc-99m, reconstructed using the OSEM algorithm. When no attenuation correction is performed, the inferior wall shows decreased activity. The artifact improves when attenuation correction is included in the reconstruction algorithm. Additionally, in women, photon attenuation through breasts can cause lowered activity in the anterior wall of the myocardium. Since breasts vary in size, position, configuration and density, breast-attenuation artifacts are extremely variable in appearance [76].

The effect of attenuation is more severe for Tl-201 than for Tc-99m based agents. Table 3.1 shows linear attenuation coefficient values for air, muscle, lung and bone for Tc-99m and Tl-201 [77]. The location, extent and severity of attenuation artifacts varies from patient to patient as a function of their anatomy. The variation in the radiotracer distribution of normal patients is thus increased, resulting in more false positive diagnoses. At any given level of true positives (sensitivity), attenuation correction can reduce this variation, thus lowering the number of false positives and increasing the specificity [78].

Table 3.1. Linear attenuation coefficient values (in 1/cm) for Tc-99m and Tl-201. From the Radiological Health Handbook (reference [77]).

	Air	Muscle	Lung	Bone
μ for Tl-201 (73 keV)	0.0002	0.191	0.063	0.429
μ for Tc-99m (140 keV)	0.0002	0.153	0.051	0.286

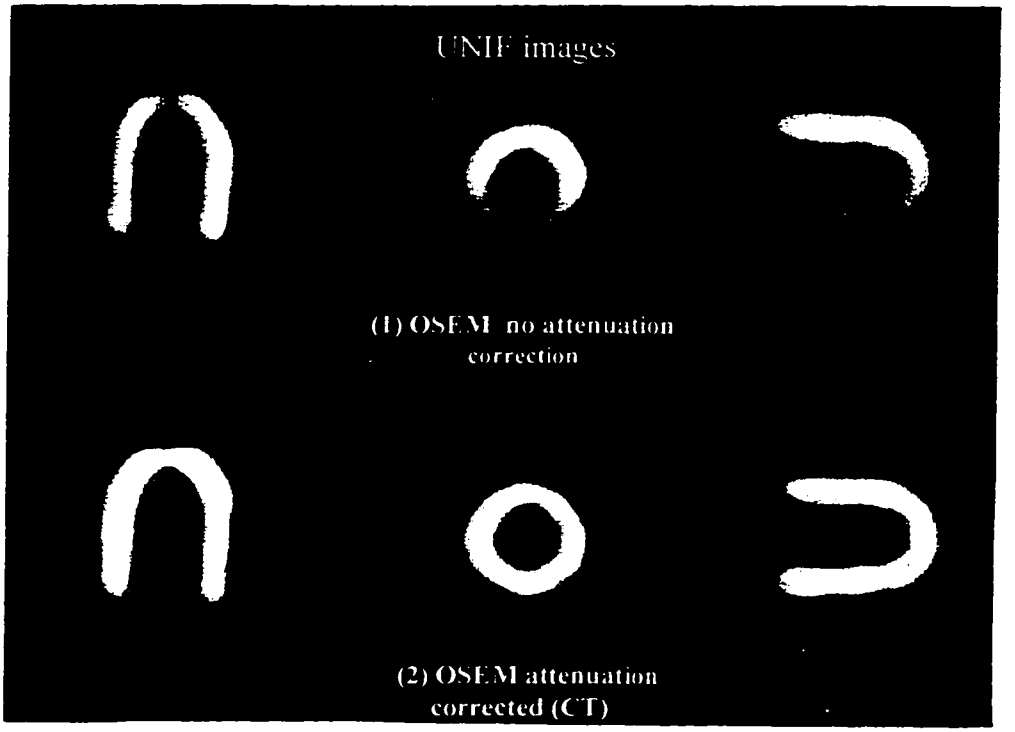

Fig. 3.3. Images of anthropomorphic phantom with uniformly distributed activity in myocardial insert, illustrating inferior wall attenuation artifact. (1) Reconstructed using OSEM with no attenuation correction, (2) Reconstructed using OSEM with attenuation correction (CT attenuation map).

Scatter can also cause artifacts in myocardial SPECT images. In particular, it is recognized that the artifacts introduced by scatter can be more serious after correction for non-homogeneous attenuation is performed [10, 29]. In myocardial perfusion imaging, significant liver uptake can occur with both Tl-201 and Tc-99m-based agents. In filtered backprojection reconstruction without attenuation correction, SPECT images of normal male patients frequently show decreased activity in the inferior myocardial wall [79]. After attenuation correction is performed, however, in some cases, the activity in the inferior wall is elevated [80-81]. It has been shown that one possible cause of this hot inferior wall artifact is scatter counts from liver uptake [80-81]. King et al [81] have shown that both non-uniform attenuation and scatter correction are required to overcome the major sources of such apparent myocardial count changes associated with liver uptake.

3.2.2. Other limitations and sources of artifacts

SPECT acquisition requires that the patient lie still through the duration of the scan to provide consistent projections over all angles. Patient motion results in artifacts on the reconstructed images, which may result in a false diagnosis. Analysis and cine display of raw projection images is recommended to reveal such errors [76]. It is possible to detect and partially correct for some patient motion after acquisition, using motion correction algorithms [82-83]. Shorter acquisition times and devices providing proper arm support reduce chances of patient motion.

During a standard myocardial perfusion SPECT acquisition, the images are blurred due to normal movement of heart walls. Gated SPECT imaging enables acquisition of separate 3-D images corresponding to several parts of the cardiac cycle. In gated SPECT, image acquisition is synchronized with the electrocardiogram (ECG) signal. Each projection is divided into a number of images (usually 8 to 16) corresponding to particular segments of the cardiac cycle. Although the gated segments contain fewer counts than conventional SPECT images, the effect of heart motion is reduced. Gated frames can be summed to produce images for evaluation of myocardial perfusion. Gated SPECT can improve the diagnostic accuracy that can be obtained from conventional cardiac SPECT [84]. The motion and thickening of the heart walls can also be observed in a cine display. In addition, changes between end-systolic and end-diastolic tomographic images can be quantified and parameters such as ejection fraction estimated [85].

Frequently, there is radiotracer uptake in the liver and intestines. It has been shown that if the liver activity is high enough, filtered backprojection can cause an artifactual decrease in inferior wall uptake in the reconstructed images [86]. After reconstruction, abdominal activity superimposed on the heart may degrade image quality and lead to increased counts in the inferior wall. Such uptake can mask a defect on either the stress or rest study. An unusual shape or contraction of the heart can also cause artifacts on both stress and rest studies [87]. There are also some physiological factors which may affect myocardial perfusion SPECT images. If the patient is not stressed adequately, the images

may not be representative of the actual myocardial perfusion at stress. Noncoronary diseases of the heart such as left bundle branch block or myocardial hypotrophy can lead to artifacts in myocardial perfusion SPECT images [76].

3.3. Non-uniform attenuation correction

Attenuation correction in cardiac SPECT requires patient-specific attenuation maps corresponding to SPECT transverse slices. Methods of estimating attenuation maps are described and reviewed in section 3.3.1. Algorithms used for non-uniform attenuation correction have been described in Chapter 2. Among them, Chang's method, IPC and MLEM are used by gamma camera vendors for non-uniform attenuation correction. Methods for scatter correction have also been reviewed in Chapter 2. Among them, the dual energy window scatter subtraction, TEW and TDCS methods can be implemented easily for myocardial perfusion SPECT.

3.3.1. Methods of estimating Attenuation maps

For attenuation correction in cardiac SPECT, transmission imaging is usually used to estimate patient specific attenuation maps that are registered with SPECT data [78]. This section describes each transmission source configuration, and discusses the advantages and disadvantages of each.

3.3.1 A. Attenuation maps from X-ray CT

Attenuation maps have been obtained from X-ray CT images by some investigators [88-89]. CT images are obtained by a CT scanner. A typical CT scanner uses a collimated beam from an x-ray tube and an array of collimated detectors (usually CsI, or bismuth germanate) in a circular configuration. CT attenuation maps have spatial resolution superior to that of attenuation maps obtained by radionuclide transmission. However, most cardiac patients do not have CT procedures performed [78]. For patients who have recent CT images available, the following difficulties have to be overcome: CT images

have to be registered to SPECT, and the CT voxel values have to be converted to linear attenuation coefficients corresponding to the energy of the radioisotope used for SPECT imaging [78]. CT voxel values (often called CT numbers) are usually in terms of a unit called Hounsfeld Unit (*HU*). It is defined as follows:

$$HU \equiv \frac{\mu - \mu_w}{\mu_w} 1000 \qquad (3.1)$$

where μ = linear attenuation coefficient of the material at the effective energy of the CT scanner, and μ_w = linear attenuation coefficient of water at the effective energy of the CT scanner. Water has, by definition, a CT number of zero. For most CT scanners, air has a CT number of approximately -1000, dense bone has a CT number of approximately 1000, and soft tissue ranges from –100 to +100.

Because of the problems mentioned above, CT maps are not often used for non-uniform attenuation correction in clinical practice. However, a few investigators have used attenuation maps obtained from CT images. Fleming has used external markers to register CT and SPECT images for phantom and patient studies [88]. Hasegawa et al [89] have developed a prototype research emission-transmission CT system, which can perform both SPECT and CT. Since the images can be acquired in the same spatial orientation, the need to register SPECT and CT attenuation maps is eliminated. Currently, the long scan times of this system prevent its clinical use [89]. To convert CT numbers to linear attenuation coefficients, simple linear energy translation based on the attenuation coefficient for water has been implemented by a few investigators [89-90]. In this method, the CT numbers are converted to linear attenuation coefficients corresponding to the effective energy of the CT scanner. The linear attenuation coefficients are then scaled by a factor, equal to the ratio of the linear attenuation coefficient of water corresponding to SPECT energy, to that corresponding to the effective energy of the CT scanner [90]. Linear energy translation is known to provide inaccurate linear attenuation coefficients for high density materials such as bone [90]. Using linear energy translation and simulated data, LaCroix et al [90] have shown that despite significant overestimation of the linear attenuation coefficient for bone, CT attenuation maps provide accurate myocardial activity concentration.

3.3.1 B. Attenuation maps obtained by radionuclide transmission

To obtain attenuation maps by radionuclide transmission, hardware such as transmission sources, associated electronics, special collimators and software have been added to present SPECT systems. Most current gamma camera systems use one stationary or dual scanning collimated line sources to acquire attenuation maps simultaneously with SPECT. In addition, several other transmission sources have been used, such as multiple line sources, and collimated and uncollimated sheet sources. Whether acquired simultaneously or sequentially, transmission images are acquired in the same spatial orientation as SPECT. Fig. 3.4 shows four configurations of radionuclide sources and collimators used in transmission imaging.

For transmission line sources, Gd-153 is usually used for Tc-99m-perfusion agents, and Gd-153, Co-57, Am-241 or Tc-99m are used for Tl-201 agents. Table 3.2 shows the physical characteristics of common transmission radionuclides. If Gd-153 is used for transmission imaging and Tc-99m for SPECT, the transmission data is contaminated with scattered radiation from the Tc-99m photopeak, which causes inaccuracies in the attenuation maps. For Tl-201 SPECT, the emission data is contaminated by scattered photons from transmission sources. Usually such contamination is corrected by simple subtraction-based correction methods [78, 91]. For stationary line sources, the total activities of the line source(s) vary from 20 to 150 mCi, and for scanning line sources 250 – 800 mCi [75]. For scanning line sources the activities are higher, since the source has to scan the entire camera field-of-view (FOV). For line sources with activities higher than 500 mCi, the sources are covered with attenuating material that is gradually removed as the source decays, thus prolonging the use of the source [75]. Depending on the orientation of the line source, the transmission geometry is parallel or fan-beam (Fig. 3.4.A and Fig. 3.4.B). Table 3.3 shows several aspects of non-uniform attenuation correction methods that are currently available from the gamma camera manufacturers [75].

Table 3.2. Physical characteristics of common transmission radionuclides. From the Radiological Health Handbook (reference [77]).

Radionuclide	Gamma Energy (keV)	Half-life	Used with emission radionuclide
Gd-153	99	242 days	Tc-99m, Tl-201
Co-57	122	270 days	Tl-201
Am-241	60	458 years	Tc-99m, Tl-201

The transmission data can be obtained simultaneously or sequentially with respect to SPECT. A few studies have been reported where attenuation maps have been obtained sequentially [92-93]. Sequential transmission and emission imaging allows for an accurate pixel-by-pixel correction of contamination of transmission data. The events acquired in the transmission energy window during emission imaging can be used to estimate the amount of contamination from scattered emission data in the transmission attenuation maps. The patient acquisition time is increased by about 5 minutes [93]. However, patient motion between the emission and transmission scan can cause registration errors and artifacts [94-95].

A common transmission set-up consists of two scanning line sources opposite detectors with parallel-hole collimators [96]. This approach was first proposed by Tan and Bailey [96] and adopted by several gamma camera vendors. It is illustrated in Fig. 3.4 A. For each projection, during acquisition, the line source scans from one end of the detector to the other. The camera head opposite to the collimated line source is electronically windowed to accept events in a narrow region opposite the line source only. The emission images are also electronically windowed to store events only when the transmission source is not opposite to the detected event. This reduces both the amount of scatter in transmission data and minimizes contamination of transmission data by scattered radiation from the SPECT energy window [96]. Further advantages of this configuration are: (i) the entire camera FOV is used for transmission imaging, reducing possibility of truncation of attenuation maps (which can happen in fan-beam transmission

geometry for patients larger than the transmission field-of-view); (ii) the line source is not required to be at a fixed distance because parallel collimators are used; (iii) only a line source (as opposed to a sheet source) needs to be filled, stored, shielded and mounted on the system thus making handling more managable and reducing exposure to workers. The disadvantages of such transmission geometry is the requirement to modify gamma camera systems to move the source mechanically and to perform electronic windowing. On modern gamma camera systems, these difficulties are resolved by the manufacturers [78]. The transmission images are also of lower quality and spatial resolution than those acquired by a stationary line source (fan-beam transmission geometry) [78].

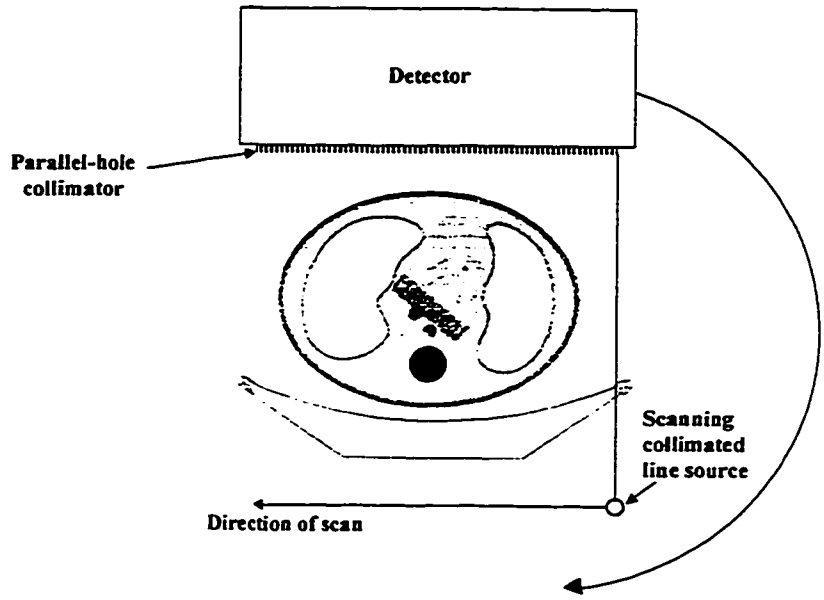

Fig. 3.4. Common transmission configurations for non-uniform attenuation correction in SPECT. **A.** Scanning collimated line source (parallel geometry).

Another common transmission geometry is a stationary collimated line source at a fixed position away from the camera equipped with a fan-beam collimator [92, 97-100]. The line source can be at the focal point of the collimator (fan-beam geometry) [92, 97-

99], or at one side (asymmetric fan-beam geometry) [100]. The imaging set-ups are illustrated in Fig 3.4.B and 3.4.C. Manglos et al [101] have also used a point source opposite a detector equipped with a cone-beam collimator. In this case the geometry is that of cone-beam.

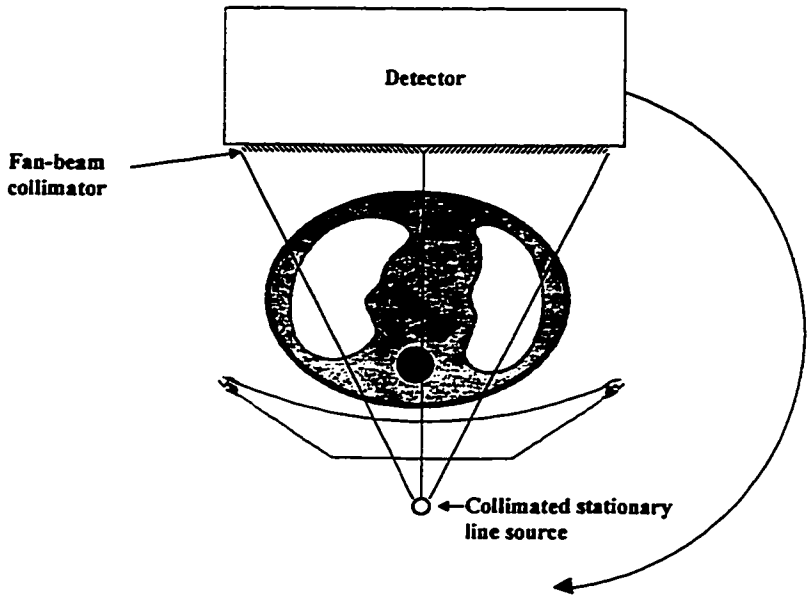

Fig. 3.4. B. Stationary collimated line source (fan-beam geometry).

The fan-beam transmission geometry has the following advantages: (i) the need for lateral motion of the source is eliminated; (ii) convergent collimation provides attenuation maps and emission images with spatial resolution superior to that obtained with parallel collimation [78]; and (iii) only line sources (as opposed to sheet sources) need to be handled, shielded, or mounted on the system [78]. The potential disadvantages are: (i) an increased truncation of the field-of-view (FOV) over that of parallel collimation on the same detector; (ii) the lack of electronic windowing to assist in correction of cross-contamination between transmission and emission imaging; (iii) the need to keep the source at the focal point of the collimator, which makes it difficult to

allow body contouring acquisitions [78]. This difficulty can be overcome by moving the source radially with motion of the opposed camera head.

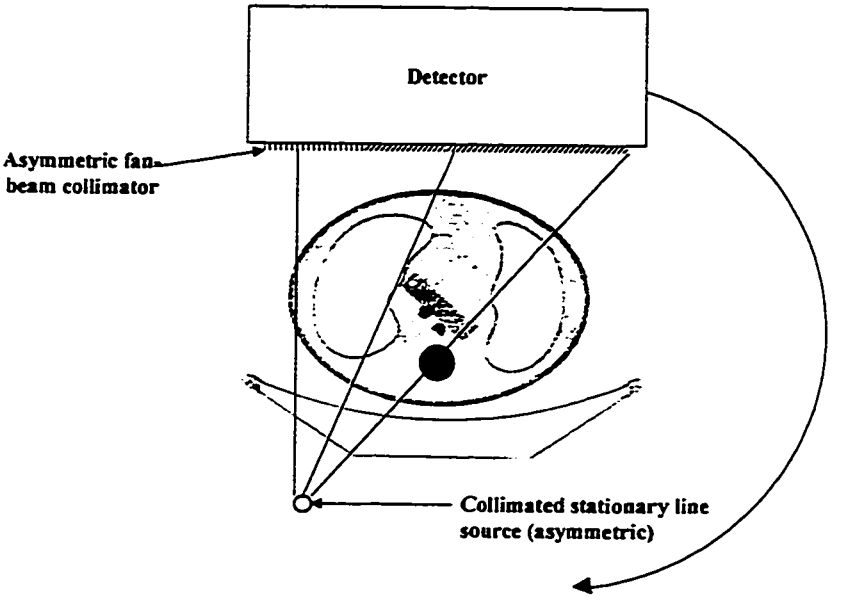

Fig. 3.4. C. Asymmetric collimated line source (asymmetric fan-beam geometry).

The main problem with the use of convergent collimation for estimation of attenuation maps is that of truncation. If filtered backprojection is used to reconstruct the images, the reconstruction is limited to only the field-of-view at every angle (or the fully sampled region). With FBP, truncation results in a "pile-up" of information at the edge of the region, and any detail outside the edge is cut off. If MLEM is used, then this pile-up is not present, and there are non-zero pixel values outside the fully sampled region; however, the area outside the fully sampled region is distorted [78]. It has been shown that the attenuation maps can be significantly improved by constraining the MLEM reconstruction to the actual area of the attenuator [97-98, 102]. The use of body outline and other information obtained by one or more parallel hole collimators in addition to the fan-beam collimators, has been shown to improve the accuracy of estimating the attenuation maps in the regions truncated by fan-beam collimators [103-104].

Truncation is also a problem for large patients on small FOV cameras with parallel transmission geometry. The question is whether using truncated attenuation maps introduces significant inaccuracies in attenuation corrected cardiac SPECT data. It has been reported that even when the attenuation map is significantly distorted outside the fully sampled region, the attenuation sums (exponential of the sums of the attenuation coefficients times path lengths) for locations in the fully sampled region are estimated fairly accurately with iterative reconstruction [97, 102]. Thus, if the heart is within the fully sampled region, a reasonably accurate attenuation correction can be found. Gregoriou et al [105] have shown that for truncation in fan-beam geometry, myocardial defect detection is affected only when there is severe truncation close to the heart. Tsui et al [106] have reported similar results using dual small FOV L-shaped detectors with parallel geometry.

Truncation effects can be reduced by using asymmetric fan-beam collimators (Fig. 3.4. C). In this configuration, by rotating 360 degrees around the patient, conjugate views fill in the region to the extent that a fully sampled region equivalent to that using parallel collimators can be obtained [100].

An array of collimated stationary line sources aligned with the axis of rotation of the camera have been proposed by Celler et al [107]. This transmission geometry has been adopted by one gamma camera vendor (Table 3.3).

Some investigators have used a sheet transmission source opposite a detector with a parallel hole collimator to estimate attenuation maps [27, 108-110]. This transmission setup is illustrated in Fig. 3.4. D. The advantages of this method are: (i) the entire FOV of the camera is used for transmission imaging, thus the possibility of truncation of attenuation maps is reduced, (ii) the transmission source is not required to be a fixed distance from the detector as with a convergent collimator, (iii) no lateral motion of the source is necessary because the whole FOV is covered by the source. The disadvantages of using the sheet source are: (i) the linear attenuation coefficients are broad-beam because the imaging geometry leads to inclusion of scattered transmission photons in the transmission energy window; (ii) if a radionuclide with a short half-life is used, such as Tc-99m, then the source must be prepared and mounted every day requiring a technologist's time and exposure; (iii) the sheet source requires an additional holder to

keep the source opposite the detector and this can be cumbersome when used clinically. The sheet source can be collimated to reduce scatter and patient exposure to transmission photons. For multi-headed cameras the sheet source can partially or wholly block the other heads.

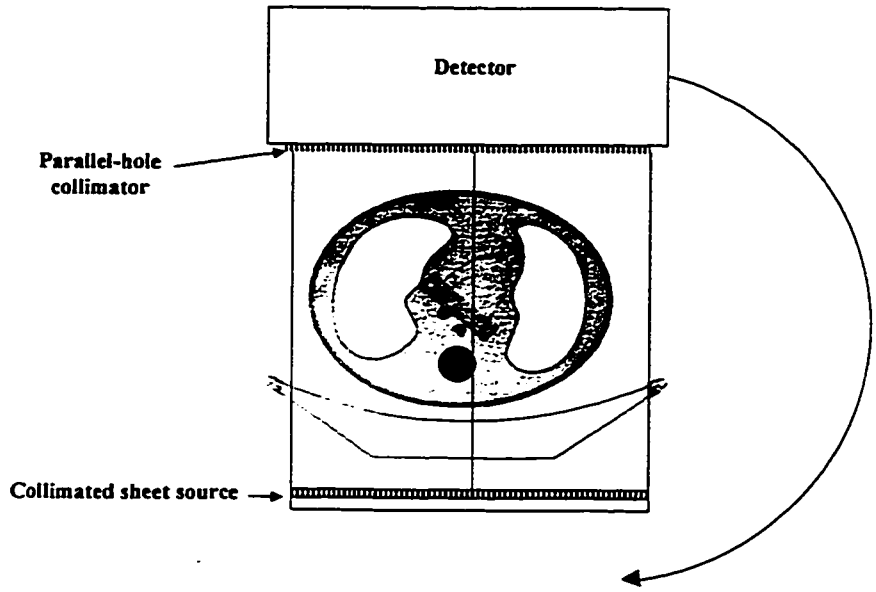

Fig. 3.4. D. Collimated sheet source (parallel geometry).

However, for single-headed gamma cameras, none of the gamma camera vendors offer transmission hardware to acquire attenuation maps [75]. If the camera head has a counter-balance, some of the problems of keeping the transmission source fixed opposite the detector can be easily overcome. Kemp et al [99] have also used a stationary collimated line source with a single-headed gamma camera equipped with a fan-beam collimator.

3.3.1 C. Attenuation maps obtained without transmission imaging

Attenuation maps have been estimated by alternative methods to transmission imaging in an attempt to simplify data acquisition. One method is to inject Tc-99m macroaggregated albumin (MAA) after SPECT, and image the patient again [111-112]. Since Tc-99m MAA is localized in the lungs, the position and extent of the lungs can be obtained by segmentation. The body outline can be obtained either by an external wrap smeared with Tc-99m [111], or by segmenting scatter window data [112]. The attenuation map is formed by assigning linear attenuation coefficients to lung and soft tissue regions. The advantage of this method is that no modification to the SPECT system is required to obtain attenuation maps, however, a second radiopharmaceutical must be administered and additional imaging performed.

Pan et al [113] have estimated attenuation maps by segmenting the body and lung regions from the scatter energy window and photopeak images. This method was applied to an anthropomorphic phantom and 16 patient studies. In these studies, lungs regions were visually estimated from scatter energy data, with additional anatomic information of the myocardium region, the spine and sternum locations, the liver and ribcage, from the photopeak window data. Attenuation maps estimated in this way were determined to agree well with those obtained by transmission imaging with a slant-hole collimator, for one patient. The advantages of this method are that no modification to the SPECT system is required, and re-imaging the patient is not necessary as in the emission-based techniques. The potential limitation of this method is the visual estimation of the regions from scatter window and photopeak data, which is not automated and is observer-dependent [113].

Table 3.3. Commercially available non-uniform attenuation correction methods.

(**Abbreviations in this table**: Trans - transmission; emis - emission; DSCL - dual scanning collimated line; wrt – with respect to; SCL - scanning collimated line; Cl - collimated line; MCLA -multiple collimated line array; US - uncollimated sheet; Asymm. – asymmetric; emis. – emission; Acq. – Acquisition; Sim – simultaneous; seq – sequential; AC – Attenuation correction; MLEM – Maximum Likelihood Expectation Maximization; OSEM – Ordered Subsets Expectation Maximization; FBP – filtered backprojection; IPC – Iterative pre-correction; IC – Iterative Chang.)

Gamma camera manufacturer	No. of heads on gamma camera	Source	Geometry	Trans. Isotope (for Tc-99m emis.)	Activity (mCi)	Acq. mode (wrt SPECT)	AC algorithm
ADAC	2	DSCL	parallel	Gd-153	250	Sim	MLEM
Elscint	2	DSCL	parallel	Gd-153	300	Sim	IPC + FBP
GE	2	DSCL	parallel	Gd-153	500	Seq	MLEM
Picker (STEP 2000)	2	SCL	parallel	Gd-153	800	Sim	MLEM/ OSEM
Picker (STEP 3000)	3	CL	Fan-beam	Gd-153	60	Sim/Seq	MLEM/ OSEM
Siemens (Profile)	2	MCLA	Parallel	Gd-153	150	Sim	IPC + FBP
Siemens (Music)	3	CL	Asymm. fan-beam	Am-241	150	Sim	IPC + FBP
SMV	2	DSCL	Parallel	Tc-99m/ Gd-153	300	Sim	FBP + IC
Toshiba	2	US	Parallel	Tc-99m/ Gd-153	25	Sim	FBP + IC

3.3.2. Effect of attenuation correction in myocardial perfusion SPECT on detection of CAD

Clinical trials published to date indicate that attenuation correction of myocardial perfusion images results in significantly improved specificity for the detection of coronary artery disease [19, 93, 114]. Prvulovich et al [93] have shown that the use of attenuation correction yields improved homogeneity of Tl-201 distribution in 36 patients with low risk of CAD. This investigation was done using an L-shaped dual-detector SPECT system with a dual scanning line source. Kluge et al [114] have shown that the use of attenuation correction increases the specificity for detection of coronary artery disease, for a given sensitivity level. This study was done using an L-shaped dual-detector SPECT system with a dual scanning line source, on 25 male patients with >= 50% stenoses of the right coronary artery and/ or the right circumflex artery. In both studies, the attenuation correction algorithm used was MLEM. Ficaro et al [19] have shown that the use of attenuation correction significantly improves the diagnostic accuracy of myocardial perfusion imaging using Tc-99m sestamibi, for the detection and localization of coronary artery disease. This study was done using a triple-detector SPECT system with fan-beam transmission geometry, on 60 patients with angiographically verified coronary artery disease and 59 patients with low likelihood of CAD. In this study, an iterative penalized weighted least squares algorithm was used for reconstructing the transmission attenuation maps and for attenuation correction.

3.4. Quantitation methods

Quantitative methods have been developed to standardize analysis of cardiac SPECT images. Patient images are usually compared to a database of normal patient images that are acquired and processed using the same protocols [115-116]. A popular method for visualization and quantitation is the polar map or bull's-eye scheme [115-117]. In this method, maximal count values are found in the myocardium along vectors perpendicular to the long axis of the ventricle. These values are mapped into a 2-D circular plot. The

center of the polar map represents the apex and the outermost circle represents the base of the myocardium. Thus each concentric ring in the polar plot represents one short-axis slice. Individual polar maps are constructed for stress and rest images. Polar maps can further be divided into sectors and the maximal count values in each sector analyzed [19, 93]. Quantitative techniques based on polar maps have been validated extensively for Tl-201 [118] and for Tc-99m sestamibi [119]. In these methods, a normal database of gender-matched patients were built, and an average normal polar map was created. Polar maps of abnormal patients were then compared to the average normal polar map. The differences were displayed on the polar map in color (with pixels color-coded to the number of standard deviations below normal maximal count value) and blackout polar maps indicating abnormal regions were generated.

Other investigators have developed alternate approaches to myocardial perfusion quantitation. Maublant et al [70] have used a segment map consisting of 36 sectors to determine regional myocardial count distribution. Slomka et al [120-121] have developed a fully automated cardiac reorientation and quantitation method in which stress and rest composite reference templates are built from gender-matched normal patients. Abnormal patient scans are registered to the corresponding normal template, and compared with the template on a voxel-by-voxel basis. Abnormal regions are visualized directly on the short-axis, horizontal long axis and vertical long axis slices and also in 3-D on the volume rendered myocardium. Quantitative parameters such as the severity and volume of the defect are reported. The myocardium can also be divided into 9 segments and the average radial maximum in each segment reported. In comparison to polar map visualization and quantitation, this method is three-dimensional and voxel-based, and the defects are visualized on the patient images [121]. This quantitation method has been utilized in this thesis.

3.5. Summary

In summary, attenuation and scatter correction are required to reduce artifacts and improve quantitation in SPECT. Several methods have been proposed to estimate

attenuation maps, each has its advantages and disadvantages. The use of stationary or scanning line source(s) to estimate attenuation maps is common, but multiple line sources, transmission flood sources, emission based methods and scatter window-based methods have been reported. Common attenuation correction algorithms are Chang's method and iterative pre-correction method, both used in conjunction with filtered back projection, and MLEM reconstruction. Several methods for scatter correction have also been proposed, among them, the dual energy window scatter subtraction, TEW and TDCS methods can be implemented easily for myocardial perfusion SPECT. Polar map representation is a popular and established quantitation method. Recently, automated 3-D quantitation methods have been described using voxel-by-voxel statistical comparison with reference normal templates.

CHAPTER 4: COMPARISON OF ORDERED SUBSETS EXPECTATION MAXIMIZATION AND CHANG'S ATTENUATION CORRECTION METHOD IN QUANTITATIVE CARDIAC SPECT[1]

4.1. Introduction

As mentioned in Chapter 3, photon attenuation is known to be one of the primary factors causing image degradation and artifacts in myocardial perfusion SPECT images [76]. Several attenuation correction algorithms have been described in the literature [12-13, 30-32]. Among them, a widely used method is Chang's method, which was proposed initially for uniform attenuating media [30], and later adapted for non-uniform attenuators [27, 31]. The Maximum Likelihood Expectation Maximization (MLEM) algorithm has been used for non-uniform attenuation compensation [27], but until recently the reconstruction times were too long to be clinically feasible. Hudson et al [14] have recently described Ordered Subsets Expectation Maximization (OSEM) algorithm, which utilizes ordered subsets of projection data to accelerate the MLEM reconstruction. Such acceleration techniques, combined with the increasing speed of modern computers, have made the MLEM algorithm clinically applicable [10-11].

As mentioned before, attenuation correction in cardiac SPECT requires patient-specific attenuation maps. These are usually obtained by radionuclide transmission measurements, using a transmission line source [96, 98]. Attenuation maps have been obtained from X-ray CT images. CT provides the best spatial resolution, however, to obtain attenuation maps from CT, the following difficulties have to be overcome: CT images have to be registered to SPECT, and the CT numbers have to be converted to linear attenuation coefficients corresponding to SPECT energy [10].

The purpose of this work was to compare, for an anthropomorphic phantom, the effect of using OSEM and Chang's attenuation correction on quantitative results. The results of the

---

[1] The contents of this chapter have been submitted for publication. Comparison of Ordered Subsets Expectation Maximization and Chang's attenuation correction method in quantitative cardiac SPECT: a phantom study. Dey D, Slomka PJ, Hahn LJ, Kloiber R. Nucl Med Comm, submitted.

comparison would establish if both attenuation correction methods are equivalent, or if one is superior to the other. CT attenuation maps were used because of their superior spatial resolution. Experiments were performed simulating defects of various activity concentrations in a region of the myocardial insert corresponding to the area supplied by the right coronary artery (RCA). This region has been known to be particularly prone to attenuation artifacts [114]. The activity concentration in the defect and the rest of the myocardium were known from experiment. CT attenuation maps were registered to SPECT using automatic image registration. Quantitative parameters were calculated and compared using automated three-dimensional (3-D) methods.

4.2. Methods

4.2.1. Acquisition

An anthropomorphic phantom (Data Spectrum Corporation, Chapel Hill, North Carolina) with lung, cardiac and spine inserts was used for all acquisitions. For all the acquisitions the lung inserts were filled with dry Styrofoam beads.

4.2.1 A. SPECT acquisition

All SPECT studies were performed with Tc-99m, to simulate Tc-99m sestamibi clinical studies. No background activity was placed in the phantom. "Normal" studies (studies with no myocardial defect) and "defect" studies (studies with myocardial defects of varying specific activity) were acquired. A fillable plastic chamber spanning 180° was used for all defects. The volume of this chamber was 11.2 ml (9.3% of myocardial volume). The defect was placed in the infero-basal region and was designed to simulate hypoperfusion due to occlusion of a dominant right coronary artery (RCA).

Four types of patient situations were simulated experimentally. These were: a study with no myocardial defect (UNIF), a study in which the decrease in activity per unit volume between the myocardium and the defect was 75% (DEF75), a study in which the decrease in activity per unit volume between the myocardium and the defect was 50% (DEF50), and

a study in which the decrease in activity per unit volume between the myocardium and the defect was 25% (DEF25). For UNIF, 660 microcuries of Tc-99m was placed in the myocardial insert. This activity was found to give myocardial count statistics comparable to a typical patient imaging situation for the stress sestamibi protocol (1.8 million counts per study). For the defect studies, the myocardial insert was filled with 600 microcuries of Tc-99m and corresponding ratios in fillable defect. SPECT acquisitions were performed using a single-headed ADAC Genesys gamma camera. All acquisitions were performed in two energy windows: a 20% window centered on the 140 keV Tc-99m peak, and a 20% scatter window centered at 100 keV. The acquisition parameters for all SPECT studies were 128x128 matrix, 120 stops over 360 degrees, 15 seconds per stop, and pixel width of 4.73 mm. Table 4.1 lists the acquired SPECT images.

Table 4.1. Explanation of acronyms of SPECT images used in this chapter.

Acronym used	Explanation
UNIF	Study simulating normal myocardial perfusion
DEF75	Study simulating RCA defect with contrast 75%
DEF50	Study simulating RCA defect with contrast 50%
DEF25	Study simulating RCA defect with contrast 25%

4.2.1 B. CT acquisition

CT images of the phantom were acquired on a GE Hispeed CT scanner (General Electric, Milwaukee, Wisconsin), using a voltage of 120 kVp, 512x512 matrix, pixel width of 0.94 mm and contiguous slices with a slice thickness of 5 mm. CT attenuation maps were acquired sequential to SPECT, with no activity in the cardiac insert.

4.2.2. Data processing

All images were analyzed on a Pentium Pro 200 MHz workstation running Hermes (Nuclear Diagnostics, Stockholm, Sweden). Image analysis was done using Hermes software. The OSEM reconstruction package used was Hermes OSEM reconstruction software written by Richard Larkin [14]. Chang's non-uniform attenuation correction algorithm was written in C. Hermes Multimodality software was used for all image registration and comparison [122]. Segmental analysis was performed by using the PERFIT program (Hermes, Nuclear Diagnostics, Sweden) [120-121].

4.2.2. A. Image registration

For each SPECT study, it was necessary to perform two separate image registrations. All attenuation maps had to be registered to SPECT images for attenuation correction, and attenuation corrected SPECT images had to be registered to a reference SPECT image (UNIF) for quantitation.

Automatic three-dimensional volume registration was used for all image registrations in this study. This was done by adopting a special technique [123, see also Chapter 7 of this thesis]. Briefly, all SPECT acquisitions were performed in pairs of SPECT- RNT, using an uncollimated transmission flood source. Following each SPECT acquisition, an uncollimated flood source filled with 20 mCi of Tc-99m was fastened opposite the camera head and a transmission scan of the phantom in the same orientation as SPECT was done. The same acquisition parameters as SPECT were used for these scans. These RNT images corresponding to SPECT scans were contaminated by counts from emission data and were used not as attenuation maps, but as reference for registration only. Despite contamination due to emission counts, attenuation maps could be successfully registered to these images using automated volume registration. These images were used in this study for registering attenuation maps to each SPECT acquisition, and for registering reconstructed SPECT images to the reference normal SPECT image.

Each image registration was performed in two steps. First an approximate image alignment was done by using a technique based on principal-axes transformation [124]. Then a simplex minimization algorithm [125] was applied to the initial principal axes

transformed image by independently adjusting six transformation parameters: X shift, Y shift, Z shift, XY tilt, XZ tilt, and YZ tilt. The convergence criterion used was count-difference (sum of absolute differences) [120]. Since the pixel sizes were known, scaling in X,Y, and Z were constrained for all registrations.

The result of each automated alignment was assessed visually on all image slices in different orientations simultaneously. Two visual presentation techniques were used to verify registered image accuracy: a roving window display technique [120], and image overlay of the registered image with the image to be registered to [120].

4.2.2 B. Attenuation map processing

Prior to scanning, the GE CT scanner was calibrated for beam hardening effects with a cylindrical water phantom of diameter 20 cm [126]. To convert CT images to attenuation maps for 140 keV, the linear attenuation coefficient of water (μ_{CT}), corresponding to the effective energy of the CT scanner (E_{CT}), was calculated. By experimentally measuring the half-value layer for water at 120kVp, μ_{CT} was found to be 0.165 1/cm. The CT images were then converted to attenuation maps corresponding to photon energy of 140 keV, by linearly scaling with the ratio of μ_{CT} to the known narrow beam linear attenuation coefficient of water at 140 keV (0.153 1/cm) (linear energy translation [90]). The translated CT attenuation maps were then rebinned from 512x512 to 128x128 matrix.

4.2.2. C. SPECT Processing

Each SPECT acquisition was processed in the following way. CT attenuation maps were registered to the SPECT study [123]. The SPECT images were corrected for scatter, and then reconstructed. The reconstructed SPECT images were registered to the reference SPECT image UNIF. All SPECT images were then reoriented to Horizontal Long Axis, Vertical Long Axis, and Short Axis slices.

The SPECT images were corrected for scatter using a dual-energy-window subtraction technique [35]. The scatter fraction used was 0.5.

Each SPECT image was corrected for attenuation, with the CT attenuation map, using OSEM, and using non-uniform Chang's algorithm. For OSEM, 15 subsets consisting of 8 projections per subset and 4 iterations were used. 8 projections per subset were used to ensure that the subset balance condition was maintained [14]. The reconstruction was stopped if the following 2 criteria were satisfied: (i) the reconstructed image was visually judged to be acceptable, and, (ii) between 2 iterations, change in the Chi-squared difference between the current and measured projections, was less than 0.1%. The number of iterations satisfying these criteria was 4 for all SPECT studies. A depth independent Gaussian collimator blur with standard deviation equal to 4.0 mm (corresponding to a SPECT FWHM of 9 mm) was used in the reconstruction.

To apply Chang's method, scatter corrected SPECT projections were reconstructed using filtered backprojection. Following reconstruction, the transverse images were corrected for attenuation using non-uniform Chang's algorithm, with the CT attenuation map. All SPECT images were post-reconstruction filtered by a 3D Butterworth filter (cutoff frequency 0.64 cycles/cm, order 5).

4.2.3. Quantitation

For the phantom, we compared defect studies to the normal phantom study. Three-dimensional automated quantitation methods were used. For defect and normal studies corrected for attenuation with OSEM and Chang's method, 3 parameters were calculated. These were: defect-to-normal Average Radial Maximum ratio for the infero-basal segment (using segmental analysis), Maximum Defect Contrast, and Defect Volume. In addition, we evaluated, using segmental analysis, uniformity of the normal myocardium.

Segmental analysis: The reoriented myocardium was divided into 9 segments by using PERFIT program. These segments were anterior-basal, lateral-basal, inferior-basal, septal-basal, anterior-mid, lateral-mid, inferior-mid, septal-mid, and apical. A radial search for the maximum values was performed according to the improved Bulls-eye scheme [115-116]. For each segment, all radial maximum values were averaged to calculate the Average Radial Maximum (ARM) counts. The division of the myocardium into segments is illustrated in Fig. 4.1. The ARM values were further analyzed to

calculate defect-to-normal ARM ratio for the infero-basal segment, uniformity of normal myocardium and difference from CT.

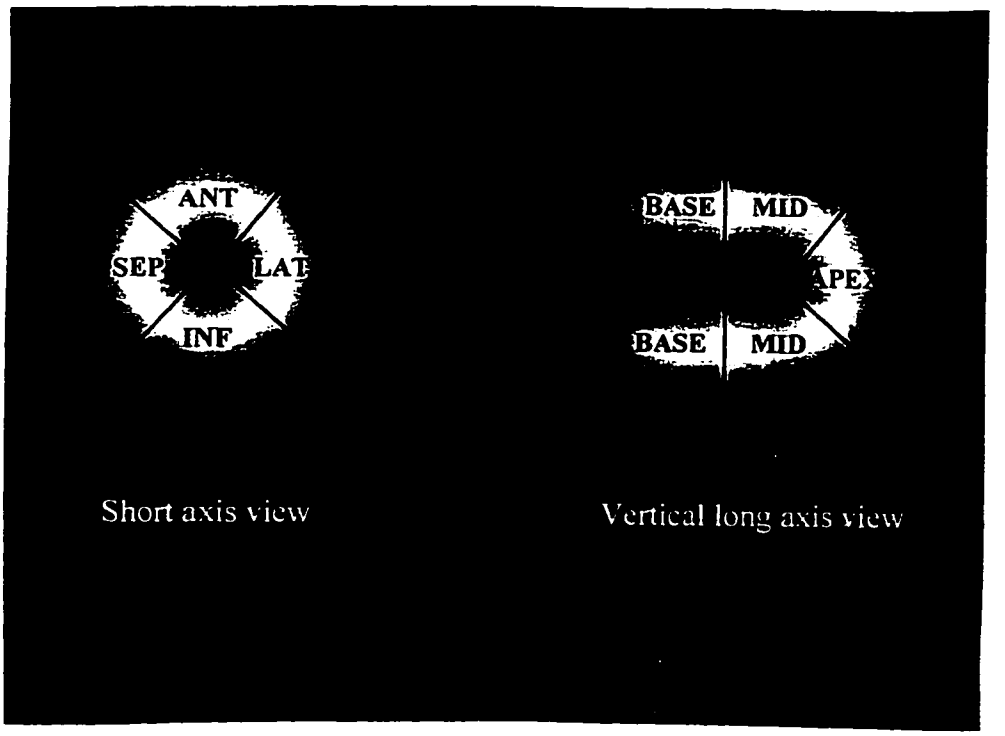

Fig. 4.1. Figure illustrating division of the myocardium for segmental analysis (shown on UNIF OSEM CT images).

Defect-to-normal ARM ratio for the infero-basal segment: For all defect studies, for each reconstruction, the ratios of ARM values between each defect and normal studies were calculated. For the simulated RCA defect, the maximum decrease in ARM values for all the images was found in the infero-basal segment. In this thesis we present the ratios from this segment only.

Uniformity of normal myocardium: To assess the uniformity of counts in the normal myocardium, four ratios were calculated for UNIF projections, for each attenuation correction method. These were the ratios of Anterior basal ARM to Inferior basal ARM, Anterior Mid ARM to Inferior Mid ARM, Lateral Basal ARM to Septal Basal ARM, and Lateral Mid ARM to Septal Mid ARM.

Maximum defect contrast and Defect volume: For all defect studies, for each attenuation correction method, the measured maximum defect contrast and defect volume was

calculated using a method similar to a recently introduced cardiac quantification package [120-121]. The Maximum defect contrast (*MDC*) was defined as follows:

$$MDC = \frac{N - D}{N} \qquad (4.1)$$

where N = maximum voxel value in uniform part of cardiac insert, D = minimum voxel value in defect.

Both normal and the defect studies were used to calculate *MDC*. *N* was the maximum in the normal image. *(N-D)* was calculated in the following way. Each defect study was normalized to the UNIF study, and the normalized defect study was subtracted from the UNIF study; the maximum voxel value in the subtracted image corresponded to *(N-D)*. The normalization method was the same as the one used for Bulls'-eye quantitation [116].

The defect volume was calculated by difference-based region-growing between normal and defect studies (Fig. 4.2). Due to partial volume effect, the defect volume calculated by this method is strongly dependent on the difference threshold used. For patient studies, this threshold can be determined automatically from the normal mean and variation template [120]. Obviously this cannot be done for only one normal phantom. Our aim in this analysis of defect volume was not to determine which attenuation correction method gives a value closest to the known defect volume, but to estimate the variation in defect volumes for all the attenuation correction methods used. Therefore, the same difference threshold was used for images reconstructed with both OSEM and Chang's algorithm.

4.2.4. Error Analysis

Errors in quantitative results due to statistical variations in SPECT data were evaluated. To estimate the statistical variation in SPECT data regardless of the gamma camera used for acquisition, the SPECT measurement simulating normal myocardial perfusion (UNIF), was repeated four times. These measurements were performed using the ADAC Genesys, and the dual-headed Picker PRISM 2000. For the Picker Prism 2000, only one head was

used for acquisition. The activity in the cardiac insert and acquisition parameters were the same as UNIF.

Each repeated acquisition was reconstructed with OSEM using the CT attenuation map and registered to the UNIF image. The variation of ARM counts for each segment, maximum defect contrast and defect volume were estimated by comparing the defect studies to each of the five normal studies.

The variation of ARM counts for each segment, maximum defect contrast and defect volume for Chang's method was not directly available. However, assuming that the variation for Chang's method is equivalent to the corresponding variation for OSEM (which is actually estimated), the quantitative results for OSEM and Chang's method were compared using a Student's t-test.

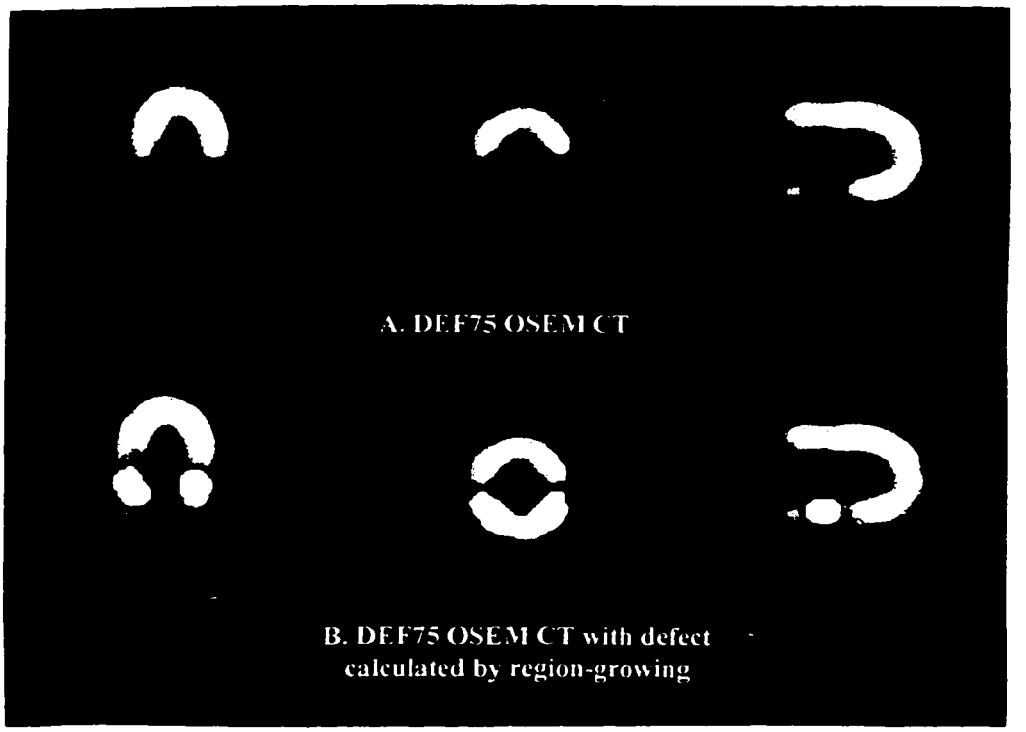

Fig. 4.2. Processed DEF75 images. **A.** DEF75 OSEM CT images. **B.** DEF75 OSEM CT with defect calculated by region-growing.

4.3. Results

4.3.1. Appearance of the attenuation corrected SPECT images

Figure 4.3 shows the UNIF study corrected for attenuation using OSEM and non-uniform Chang's algorithm. Figures 4.4, 4.5 and 4.6 show the DEF 75 study, the DEF 50 study and the DEF 25 study respectively. Table 4.2 shows the ARM ratios for the evaluation of the uniformity of the normal myocardium.

From Fig. 4.3-4.6, it can be seen that for all the SPECT acquisitions, OSEM attenuation correction gives a more correct activity distribution, with respect to both the homogeneity of the radiotracer and the shape of the cardiac insert.

This non-uniformity can be quantified from the uniformity of the normal myocardium in Table 4.2. Since the activity distribution is uniform, all four ratios in this table should be 1.00. OSEM gives values closer to 1.00. The maximum difference between the four ratios for OSEM and Chang's method is 7.9% for the lateral/septal mid segment ratio.

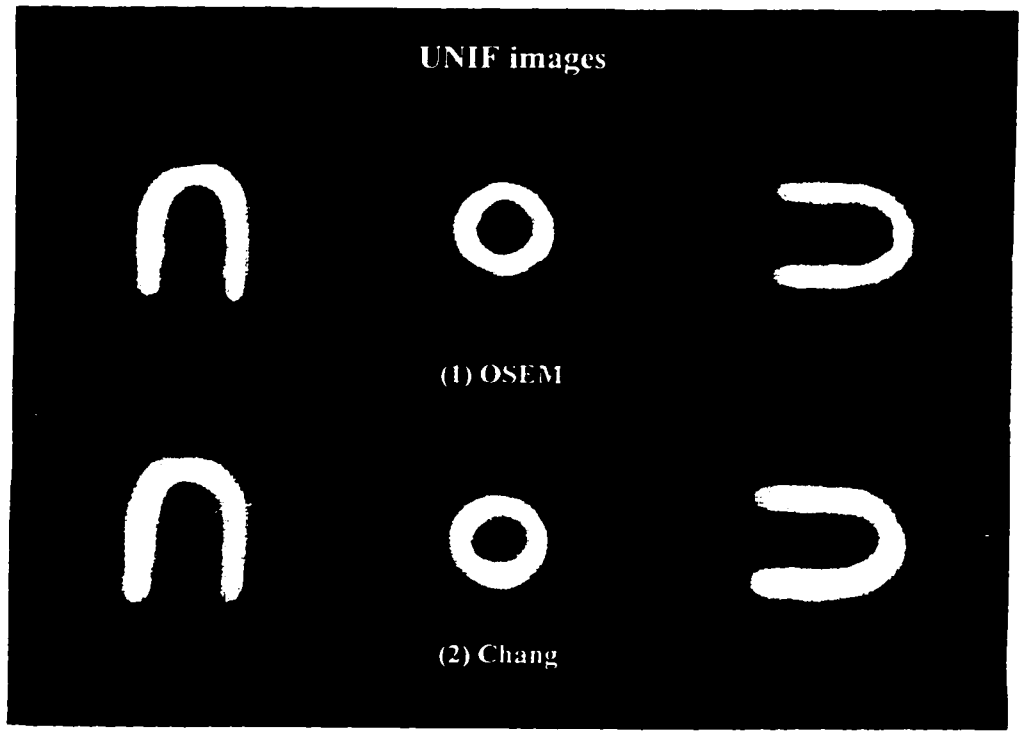

Fig. 4.3. UNIF images. (1) Attenuation corrected using OSEM, (2) Attenuation corrected using Chang's algorithm.

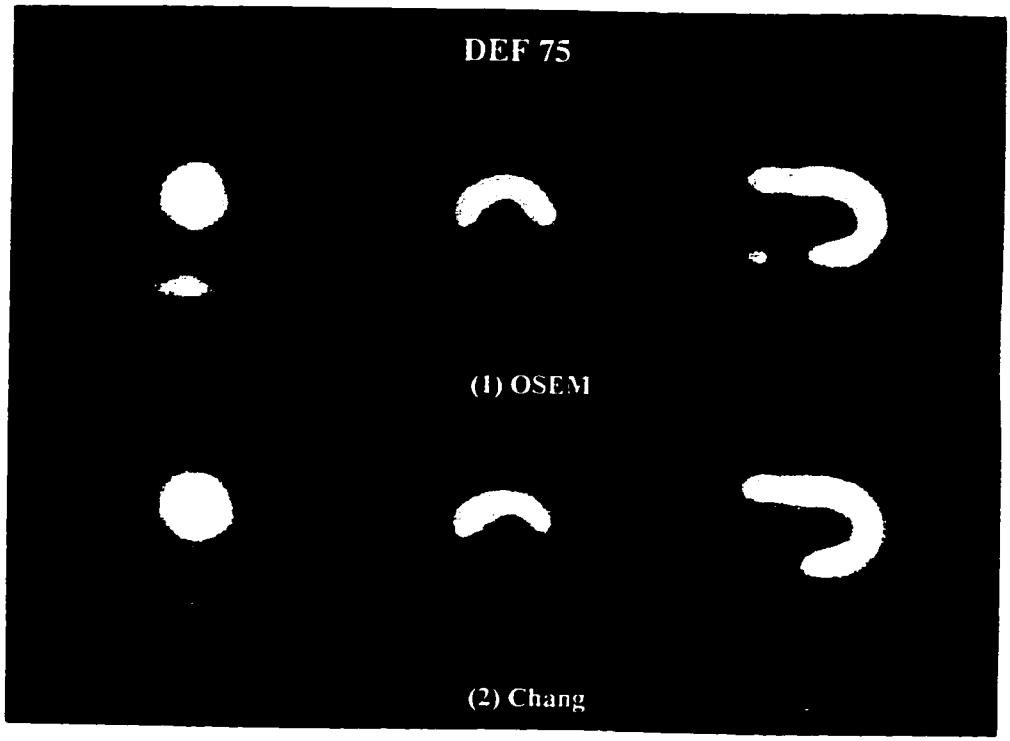

Fig. 4.4. DEF75 images. (1) Attenuation corrected using OSEM, (2) Attenuation corrected using Chang's algorithm.

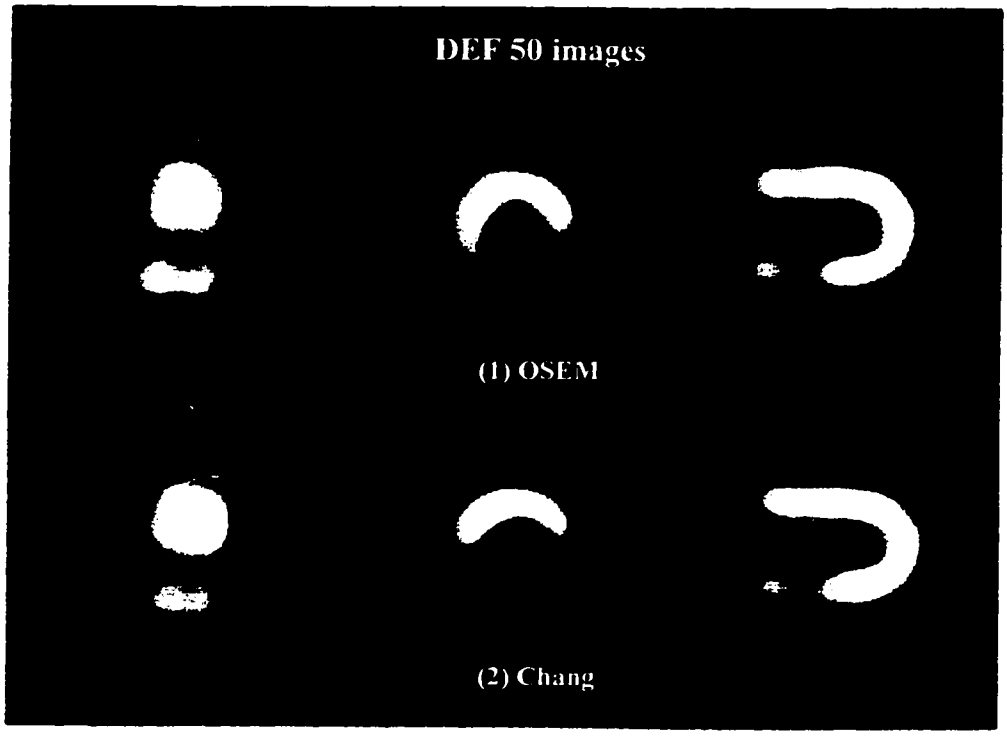

Fig. 4.5. DEF50 images. (1) Attenuation corrected using OSEM, (2) Attenuation corrected using Chang's algorithm.

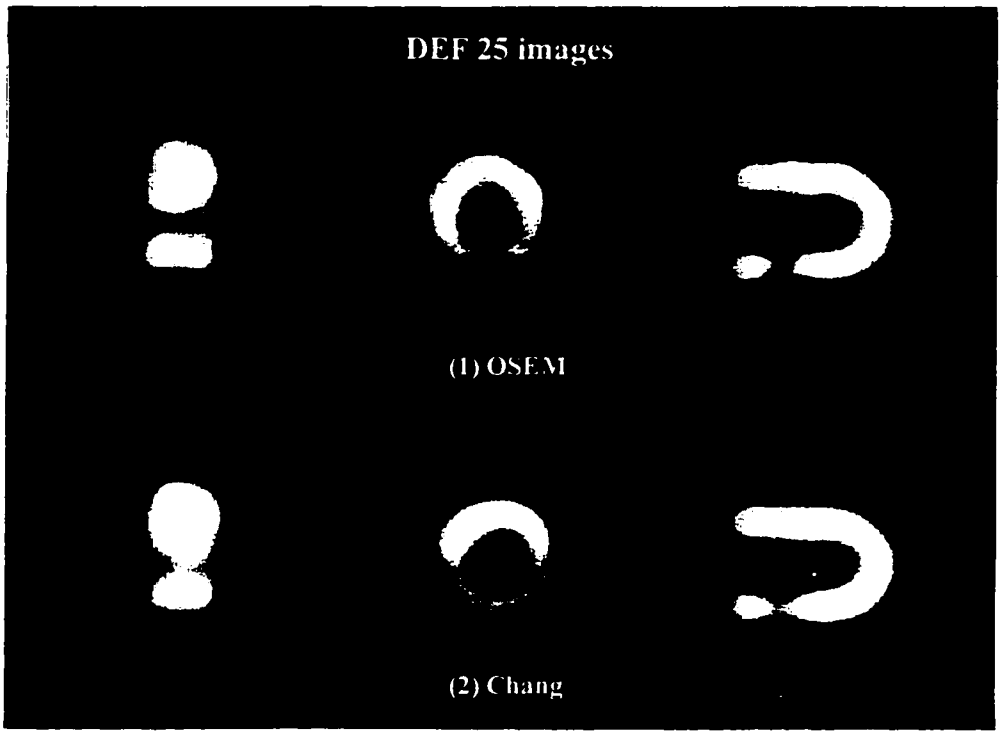

Fig. 4.6. DEF25 images. (1) Attenuation corrected using OSEM, (2) Attenuation corrected using Chang's algorithm.

Table 4.2. Uniformity of normal myocardium: Anterior/Inferior and Lateral/Septal ARM ratios for UNIF.

	Actual	OSEM	Chang
Anterior/Inferior Basal	**1.00**	**0.90**	**0.91**
Anterior/Inferior Mid	**1.00**	**0.91**	**0.89**
Lateral/Septal Basal	**1.00**	**0.99**	**0.93**
Lateral/Septal Mid	**1.00**	**0.89**	**0.82**

4.3.2. Quantitative results

The quantitative results comparing defect studies to normal, for each attenuation correction method, are shown in Fig. 4.7 – 4.9. The dashed lines indicate an estimate of the statistical variation in quantitative results for OSEM reconstruction with the CT attenuation map. For each quantitative parameter and each defect study, the standard deviation due to variation in emission data was calculated. The error in each quantitative parameter was taken to be two times the standard deviation due to variation in emission data.

Fig. 4.7 shows graphs of the defect/normal ARM ratio for the infero-basal segment for each attenuation correction method, for each defect study. The difference in defect/ normal ARM ratio for OSEM and non-uniform Chang's attenuation correction for all three defects are < 3.1%, and within the estimated statistical error range.

Fig. 4.8 shows a graph of maximum defect contrast for each attenuation correction method, for the three defect studies. The difference in maximum defect contrast for OSEM and non-uniform Chang's attenuation correction is 10.5% for the DEF 75 study, 6.4% for the DEF 50 study, and 18.6% for DEF 25 study. It can be seen from Fig. 4.8 that the differences for the DEF 25 and DEF 50 study are within the estimated statistical error. The maximum defect contrast value for DEF 75 for Chang's method is slightly less than the lower limit in the error range; the value is 0.64, and the lower limit is 0.67. In this work only the normal study was repeated, but there would also be variation in the defect study. If the variation in the defect as well as the normal studies were considered, this value would probably lie within the estimated error range.

Fig. 4.9 shows a graph of defect volume for each attenuation correction method. The difference in defect volume for OSEM and non-uniform Chang's attenuation correction for all three defects are < 12.6%, and within the estimated statistical error range.

From the t-test, for DEF 75 maximum defect contrast, OSEM and Chang's method were found to differ significantly ($p<0.05$; the p-value was ~0.04). For all other quantitative results, the methods were found to not differ significantly (the range of p-values was from 0.2 to 1). As mentioned previously, the maximum defect contrast value for DEF 75 for Chang's method is slightly less than the lower limit in the error range (Fig. 4.8). The low p-value corresponds to this trend in the graph. If the defect acquisition

were to be repeated, in addition to the normal phantom study, we would expect the error range to be wider, and the p-value to be larger.

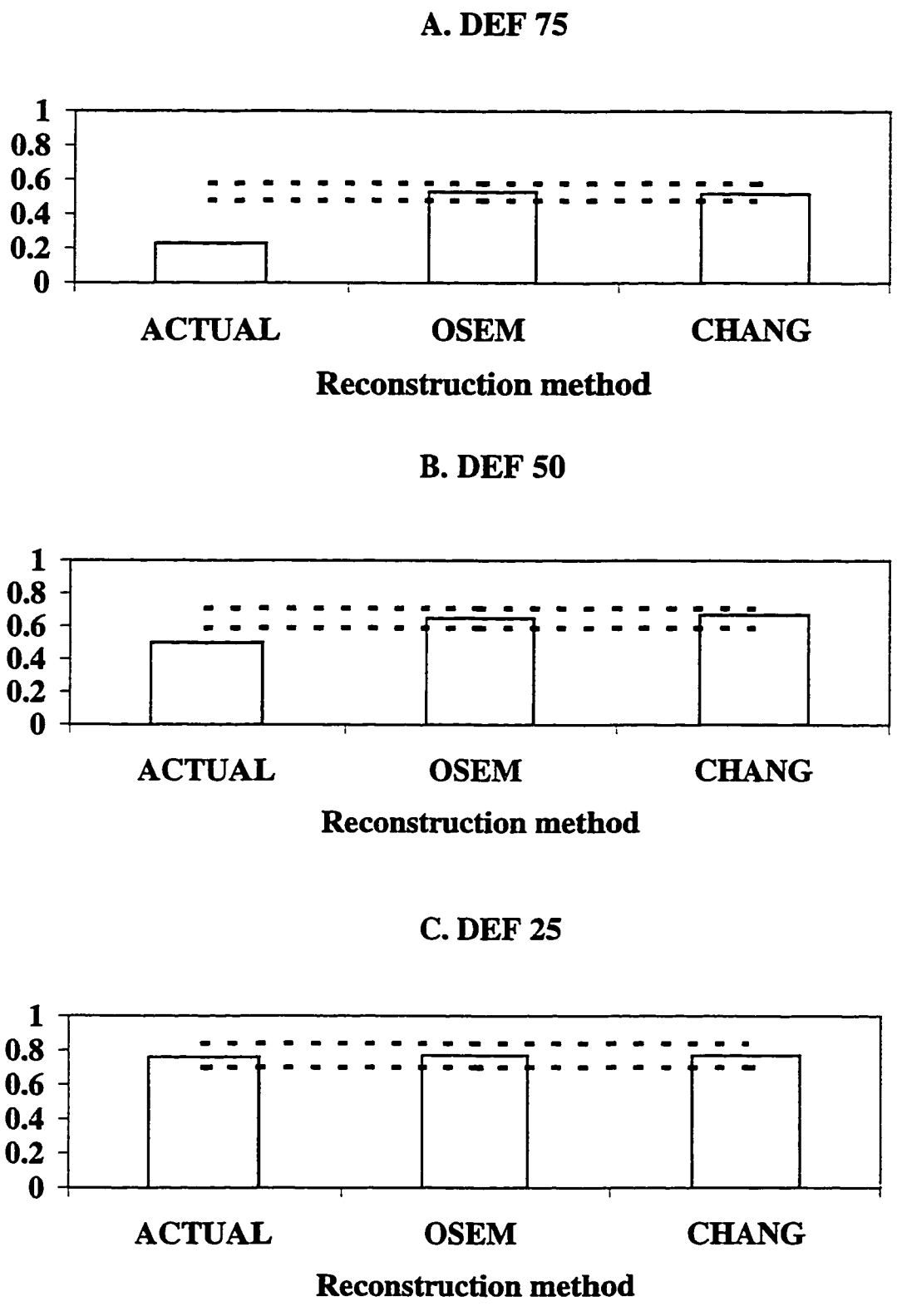

Fig. 4.7. Defect-to-normal ARM ratio for infero-basal segment for each attenuation correction method. **A.** DEF75 **B.** DEF50 **C.** DEF25.

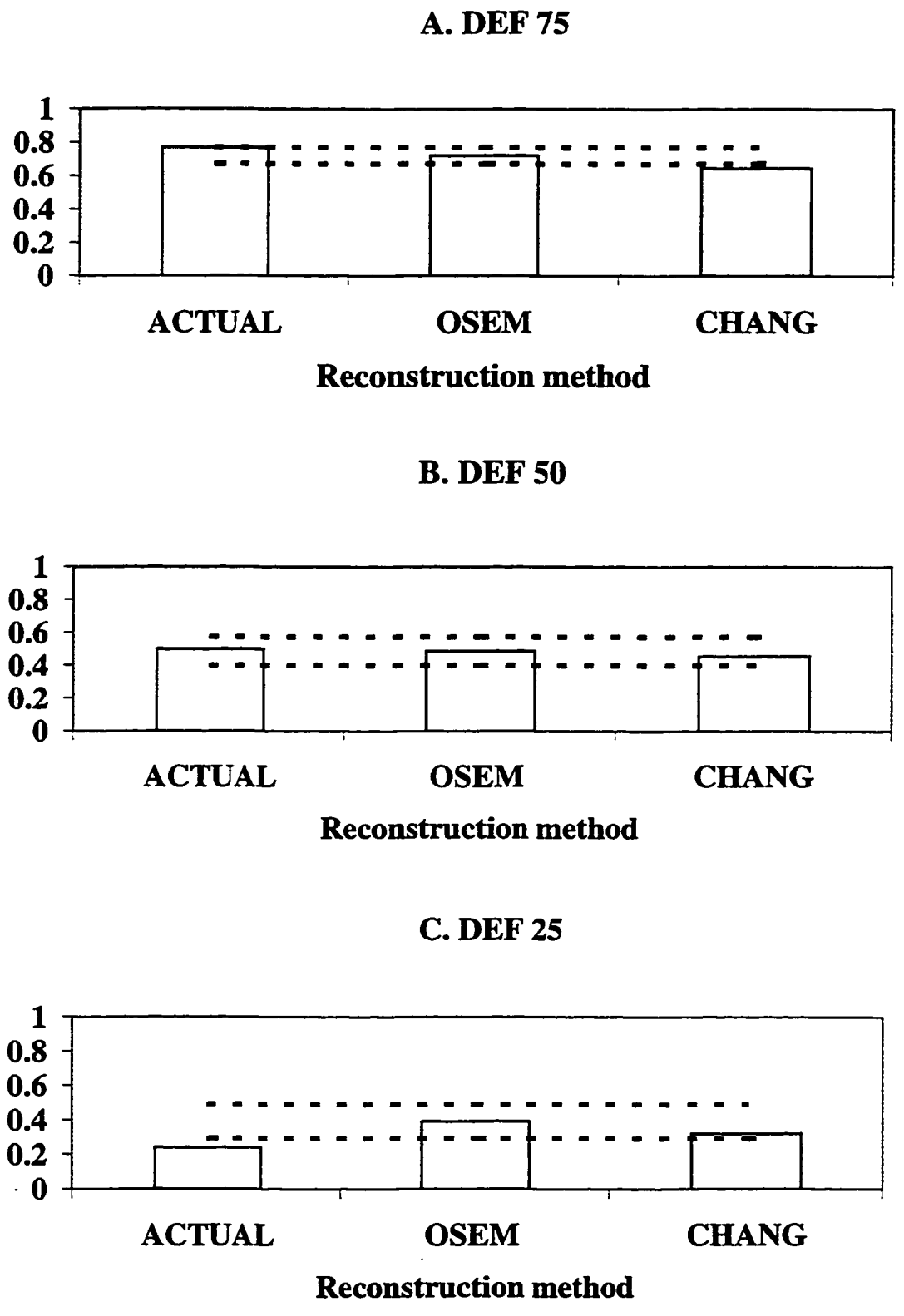

Fig. 4.8 Maximum defect contrast for each attenuation correction method.
A. DEF75. **B.** DEF50. C.DEF25

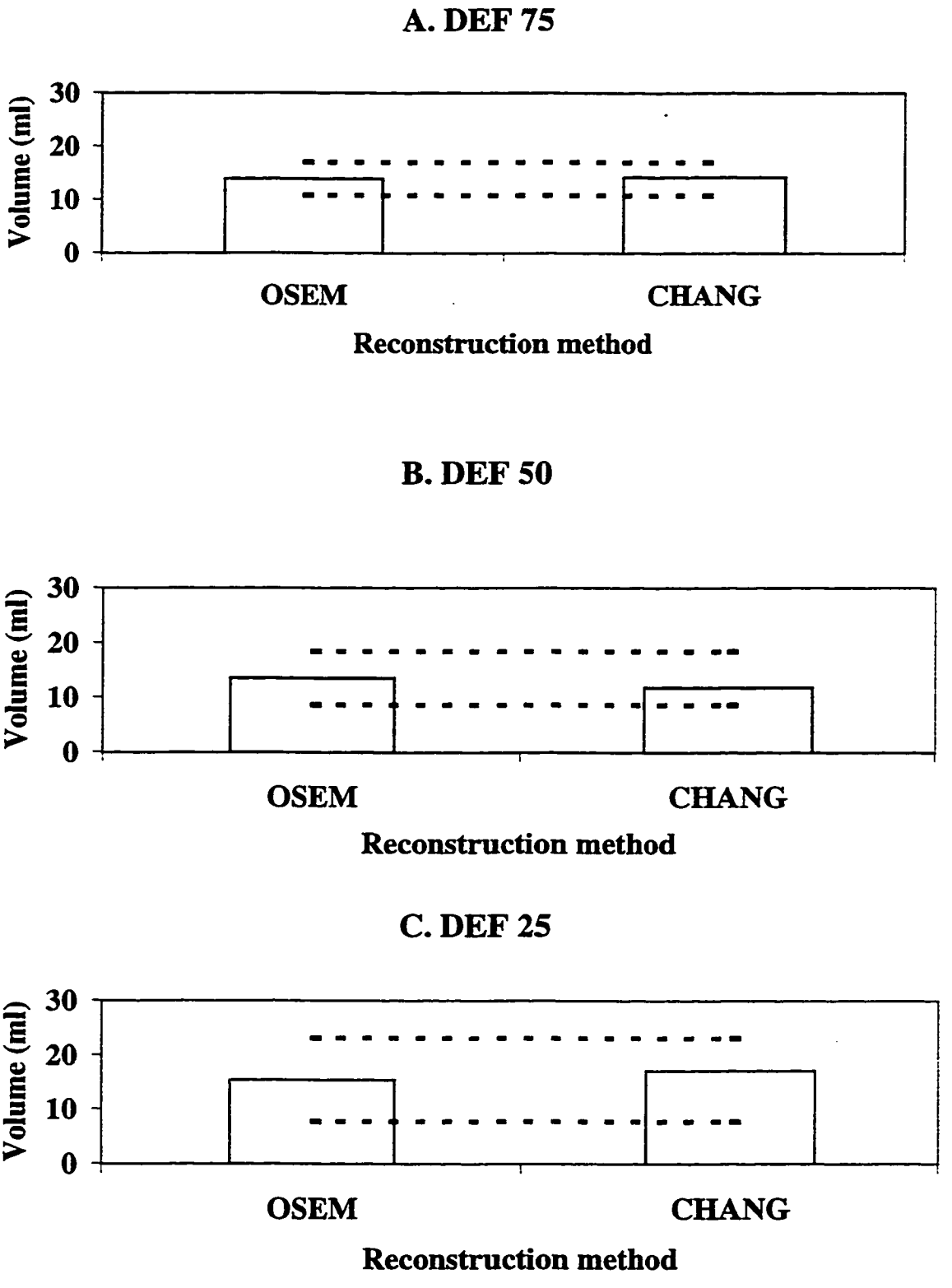

Fig. 4.9. Defect volume for each attenuation correction method. **A.** DEF75 **B.** DEF50. **C.** DEF25

4.3.3. Calculation times

The calculation times for both attenuation correction algorithms are comparable. For reconstructing 31 128x128 slices on a Pentium Pro 200 MHz workstation, the calculation time was 2 minutes (4 seconds/ slice) for Chang's algorithm, and 3 minutes (6 seconds/slice) for OSEM. Since this implementation of the OSEM algorithm stores the entire weight matrix in memory, using OSEM requires more computer memory than Chang's algorithm.

4.4. Discussion

Our results show that the differences in all three quantitative parameters, defect/normal ARM ratio for the infero-basal segment, maximum defect contrast and defect volume, are small, and mostly within the range of estimated statistical error.

From visual inspection of Fig.4.3-4.6, however, it can be seen that OSEM attenuation correction gives a more correct activity distribution, with respect to both the homogeneity of the radiotracer and the shape of the cardiac insert. The difference in uniformity between OSEM and Chang's method was quantified by using segmental analysis. This difference was found to be 7.9% or less for the UNIF study. In a comparison of MLEM and Chang's method for a heart-lung phantom and a patient study, Tsui et al [27] have also found MLEM provides a more correct radiotracer distribution, better anatomic object definition, and fewer streaking artifacts and noise. The non-uniformity is probably due to the nature of Chang's algorithm. Chang's method is applied after the images have been reconstructed by filtered backprojection. Since the correction factor is averaged over all projections, the attenuation correction is not exact.

In contrast with conventional polar plot quantitation, the quantitative parameters in this work were calculated and compared using direct, voxel-based methods. To avoid subjectivity in our comparisons, prior to performing quantitation, all SPECT images were registered to common spatial co-ordinates using automated image registration. From Fig. 4.7 and 4.8, it can be seen that, for both attenuation correction methods, Maximum Defect Contrast values are closer to the actual contrast than the Defect-to-normal ARM ratio for

all three defect studies. It is, therefore, a more accurate and preferred quantitative parameter than Defect-to-normal ARM ratio. This may be because for each SPECT study, the ARM values are calculated by averaging maximum values over a large segment. Using a larger number of smaller segments may bring the Defect-to-normal ARM ratios closer to the actual contrast. For the small defect used (11.2 ml, 10% of myocardium), it is difficult to quantify defect volume accurately because of partial volume effect. This was confirmed visually for all three defect studies - activity in the defect was increased at the edges of the defect. To properly quantify a defect volume of this size, corrections for partial volume effect should be done.

The calculation times for OSEM and Chang's attenuation correction for the phantom are 3 minutes and 2 minutes respectively. It must be noted that the calculation times reported for OSEM are for reconstruction with attenuation correction. But with Chang's method, which is applied post-reconstruction, the images must be reconstructed first using conventional filtered backprojection; this adds to the calculation time.

For non-uniform attenuation correction, Chang's method is implemented widely [75]. Though a few investigators have used OSEM [11, 24-25], it is not yet widely used. In this thesis it is shown that OSEM, while quantitatively equivalent to Chang's method, gives a more correct activity distribution. Similar results have been observed for MLEM, but the disadvantage of the MLEM algorithm is its long computing times. In this chapter, the computing times for OSEM and Chang's method are shown to be comparable.

4.5. Summary

In this work, we compared the effect of using OSEM and Chang's attenuation correction on quantitative cardiac SPECT. It was found that OSEM and Chang's attenuation correction are quantitatively equivalent. OSEM attenuation correction gives a more correct activity distribution, with respect to both the homogeneity of the radiotracer and the shape of the cardiac insert. The calculation times of both methods are comparable. Therefore, in the quantitative comparison of attenuation maps in Chapter 5, OSEM attenuation correction method has been used.

CHAPTER 5: COMPARISON OF X-RAY AND RADIONUCLIDE TRANSMISSION COMPUTED TOMOGRAPHY ATTENUATION MAPS FOR QUANTITATION IN CARDIAC SPECT [2]

5.1. Introduction

As mentioned in Chapter 3, most commercially available gamma camera systems use a stationary [98] or scanning collimated transmission line source [96] to obtain an attenuation map simultaneously with the SPECT acquisition. Since the commercial transmission hardware is expensive, some investigators have tried to estimate attenuation maps using alternate methods, based on fast transmission [92, 127], utilizing emission images [111-112] and utilizing images acquired in a scatter energy window [113].

Several investigators have used a transmission flood source to obtain attenuation maps [27, 108-110]. Galt et. al. [110] have described a method of obtaining attenuation maps by segmenting images obtained using a transmission flood source. The authors have shown that these attenuation maps have improved SPECT quantitation when compared to images with no attenuation correction. However, it is not known how they compare quantitatively to commercially available attenuation maps acquired by scanning line sources, or to attenuation maps with superior spatial resolution obtained from X-ray CT. The primary objectives of this study were to compare quantitatively, in a direct voxel-based fashion, using automated image registration to avoid subjectivity of such comparisons:

i) the effect of using attenuation maps obtained from noisy, poor quality radionuclide transmission images, to attenuation maps obtained using X-ray CT and dual scanning transmission line sources, and

ii) the effect of using attenuation maps obtained by segmenting noisy, poor quality radionuclide transmission images to attenuation maps obtained using X-ray CT and dual scanning transmission line sources. A secondary objective was to compare the effect of

---

[2] The contents of this chapter have been submitted for publication. Comparison of X-ray, radionuclide transmission and segmented attenuation maps in quantitative cardiac SPECT: a phantom study. Dey D, Slomka PJ, Hahn LJ, Kloiber R. J Nucl Cardiol, submitted.

using attenuation maps obtained by segmenting noisy poor-resolution radionuclide transmission images and CT images.

We compared the effect of using five attenuation maps on SPECT images. The attenuation maps were obtained from X-ray CT images (CT), from commercially available dual scanning transmission line source images (TLS), from uncollimated transmission flood source images (TFS), by segmenting and filling CT images with pre-assigned linear attenuation coefficients for lungs, water and spine (CT FILL), and by segmenting and filling TFS images with pre-assigned linear attenuation coefficients for lungs, water and spine (TFS FILL). Experiments were performed simulating defects of various activity concentrations in a region of the myocardial insert corresponding to the area supplied by the right coronary artery (RCA). Attenuation maps were registered to SPECT using automatic image registration. Automated three-dimensional (3-D) quantitation methods were used to compare attenuation-corrected SPECT images.

5.2. Methods

5.2.1. Acquisition

An anthropomorphic phantom (Data Spectrum Corporation, Chapel Hill, North Carolina) with lung, cardiac and spine inserts was used for all acquisitions. For all the acquisitions the lung inserts were filled with dry Styrofoam beads.

5.2.1 A. SPECT acquisition

All SPECT studies were performed with Tc-99m, to simulate Tc-99m sestamibi clinical studies. No background activity was placed in the phantom. "Normal" studies (studies with no myocardial defect) and "defect" studies (studies with myocardial defects of varying specific activity) were acquired. A fillable plastic chamber spanning 180° was used for all defects. The volume of this chamber was 11.2 ml (9.3% of myocardial volume). The defect

was placed in the infero-basal region and was designed to simulate hypoperfusion due to occlusion of a dominant right coronary artery (RCA).

Four types of patient situations were simulated experimentally. These were: a study with no myocardial defect (UNIF), a study in which the decrease in activity per unit volume between the myocardium and the defect was 75% (DEF75), a study in which the decrease in activity per unit volume between the myocardium and the defect was 50% (DEF50), and a study in which the decrease in activity per unit volume between the myocardium and the defect was 25% (DEF25). For UNIF, 660 microcuries of Tc-99m was placed in the myocardial insert. This activity was found to give myocardial count statistics comparable to a typical patient imaging situation for the stress sestamibi protocol (1.8 million counts per study). For the defect studies, the myocardial insert was filled with 600 microcuries of Tc-99m and corresponding ratios in fillable defect. SPECT acquisitions were performed using a single-headed ADAC Genesys gamma camera. All acquisitions were performed in two energy windows: a 20% window centered on the 140 keV Tc-99m peak, and a 20% scatter window centered at 100 keV. The acquisition parameters for all SPECT studies were 128x128 matrix, 120 stops over 360 degrees, 15 seconds per stop, and pixel width of 4.73 mm. The acquired SPECT images have been listed in Table 4.1 in chapter 4.

5.2.1 B. Attenuation map acquisition

Five attenuation maps of the phantom were used. These were obtained from X-ray CT scan (CT), from radionuclide transmission images using dual scanning Gd-157 line sources (TLS), from radionuclide transmission images using an uncollimated flood source filled with Tc-99m (TFS), by segmenting and filling the CT attenuation maps with pre-assigned narrow-beam attenuation coefficients for water, lungs and spine (CT FILL), and by segmenting and filling the TFS attenuation maps with pre-assigned narrow-beam attenuation coefficients for water, lungs and spine (TFS FILL).

CT attenuation maps were acquired on a GE Hispeed CT scanner (General Electric, Milwaukee, Wisconsin), using a voltage of 120 kVp, 512x512 matrix, pixel width of 0.94 mm and contiguous slices with a slice thickness of 5 mm. TLS attenuation maps were obtained by using dual scanning Gd-157 line sources on an Elscint cardiaL camera (Elscint,

Haifa, Israel). The acquisition parameters for the TLS attenuation map were 128x128 matrix, 60 stops over 180 degrees, 20 seconds per stop, and pixel width of 3.46 mm. TFS attenuation maps were obtained using an uncollimated Tc-99m flood source and a collimated single-headed ADAC Genesys (ADAC, Milpitas, California) gamma camera. The uncollimated flood source was filled with 20 mCi of Tc-99m and taped to the counterbalance of the gamma camera opposite the head. The acquisition parameters were 128x128 matrix, 120 stops over 360 degrees, and 15 seconds per stop. The pixel width was 4.71 mm. All attenuation maps were acquired sequential to SPECT, with no activity in the cardiac insert. Prior to each RNT and SPECT acquisition, pixel size calibration was performed according to the protocol established by the National Electrical Manufacturers' Association (NEMA) [128]. The pixel width was therefore known accurately. Table 5.1 lists the attenuation maps compared in this chapter.

Table 5.1. Explanation of acronyms of attenuation maps.

Acronym used	Explanation
CT	X-ray CT attenuation map
TLS	Dual scanning transmission line source attenuation map
TFS	Transmission flood source attenuation map
CT FILL	Segmented CT attenuation map
TFS FILL	Segmented TFS attenuation map

5.2.2. Data processing

All images were analyzed on a Pentium Pro 200 Mhz workstation running Hermes (Nuclear Diagnostics, Stockholm, Sweden). Image analysis was done using Hermes software as well as programs written in the C programming language. The OSEM reconstruction package used was Hermes OSEM reconstruction software written by Richard

Larkin [14]. Hermes Multimodality software was used for all image registration and comparison [122]. Segmental analysis was performed by using the PERFIT program (Hermes, Nuclear Diagnostics, Sweden) [120-121].

For each SPECT study, it was necessary to perform two separate image registrations. All attenuation maps had to be registered to SPECT images for attenuation correction, and attenuation corrected SPECT images had to be registered to a reference SPECT image (UNIF) for quantitation. Automatic three-dimensional volume registration was used for all image registrations. This was done using RNT images in the same spatial orientation as SPECT (as described in section 4.2.2.A).

5.2.3. Attenuation map processing

The five attenuation maps were obtained in the following way. The CT, TLS and TFS acquisitions were converted to linear attenuation coefficients corresponding to 140 keV. In addition, the CT and TFS attenuation maps were segmented and filled with pre-assigned narrow-beam linear attenuation coefficients for water, lungs and spine insert. The narrow-beam values of linear attenuation coefficients used were 0.153 1/cm for water, and 0.291 1/cm for the spine insert; these values were adopted from Table 2 in an investigation by Jaszczak et al [92]. The value used for lung was 0.001 1/cm.

Prior to scanning, the GE CT scanner was calibrated for beam hardening effects with a cylindrical water phantom of diameter 20 cm [126]. To convert CT images to attenuation maps for 140 keV, the linear attenuation coefficient of water (μ_{CT}), corresponding to the effective energy of the CT scanner (E_{CT}), was calculated. By experimentally measuring the half-value layer for water at 120kVp, μ_{CT} was found to be 0.165 1/cm. The CT images were then converted to attenuation maps corresponding to photon energy of 140 keV, by linearly scaling with the ratio of μ_{CT} to the known narrow beam linear attenuation coefficient of water at 140 keV (0.153 1/cm) (linear energy translation [90]). The translated CT attenuation maps were then rebinned from 512x512 to 128x128 matrix.

For TLS and TFS acquisitions, the measured transmission data were converted to integrals of linear attenuation coefficients [78], according to the following equation:

$$\mu(x, y) = [\ln(N_o / t(x, y))] / x_o \qquad (5.1)$$

where $t(x,y)$ = transmission projection counts, N_o = pixel value corresponding to transmission through air, x_o = pixel size in cm.

TLS images were scaled so that the linear attenuation coefficients in the images corresponded to 140 keV. TLS and TFS projections were reconstructed by filtered backprojection with ramp filter, and filtered by a three-dimensional post-reconstruction Butterworth filter. For TLS images, a frequency cutoff of 0.43 cycles/cm and order 5 was used. For TFS images, a frequency cutoff of 0.41 cycles/cm and order 5 was used.

For TFS images, because of scatter, the linear attenuation coefficients thus obtained do not correspond to narrow-beam attenuation coefficients. Regions of interest (ROI) were drawn on the part of the phantom corresponding to water. The TFS images were then scaled by a factor such that the average counts in these ROIs corresponded to 0.153 1/cm.

Two sets of attenuation maps filled with pre-assigned linear attenuation coefficients were obtained: one from CT (CT FILL) and the other from TFS (TFS FILL). For both attenuation maps, the range of linear attenuation coefficients corresponding to water and plastic was determined from the image histogram by thresholding. Voxels corresponding to values below this range were assumed to belong to lung region. Since the density of the styrofoam beads was not known, the lungs in both CT FILL and TFS FILL attenuation maps were filled the with 0.001 1/cm (the average value corresponding to lung on the CT attenuation maps). Voxels corresponding to water and plastic were filled with the narrow-beam linear attenuation coefficient for water (0.153 1/cm). Voxels above this range were filled with the narrow-beam linear attenuation coefficient for spine (0.291 1/cm).

Fig. 5.1 shows one transverse slice through the CT, TLS, TFS , CT FILL and TFS FILL attenuation maps.

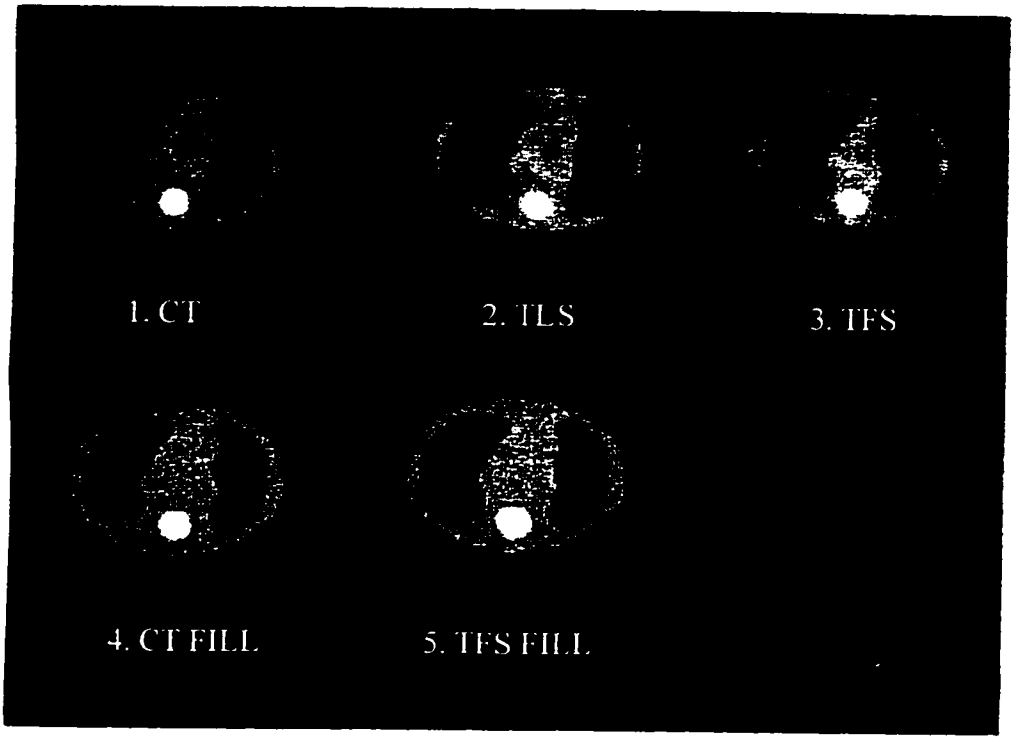

Fig. 5.1. Transverse slice of registered attenuation maps: 1. CT, 2. TLS, 3. TFS , 4. CT FILL, 5. TFS FILL. The spine insert can be seen on all attenuation maps.

5.2.4. SPECT Processing

Each SPECT acquisition was processed in the following way. Each of the five attenuation maps were registered to the SPECT study [123]. The SPECT images were corrected for scatter, and then reconstructed. The reconstructed SPECT images were registered to the reference SPECT image UNIF. All SPECT images were then reoriented to Horizontal Long Axis, Vertical Long Axis, and Short Axis slices.

The SPECT images were corrected for scatter using a dual-energy-window subtraction technique [35]. The scatter fraction used was 0.5. Scatter corrected SPECT projections were reconstructed using Ordered Subsets Expectation Maximization (OSEM) algorithm, with no attenuation compensation, and the five attenuation maps. Since filtered backprojection is commonly used, the projections were also reconstructed using filtered backprojection for comparison. For each SPECT acquisition, 7 reconstructed images were obtained. These were: filtered backprojection (no attenuation compensation), OSEM with no attenuation

compensation, OSEM with CT attenuation map, OSEM with TLS attenuation map, OSEM with TFS attenuation map, OSEM with CT FILL attenuation map, and OSEM with TFS FILL attenuation map.

For all OSEM reconstructions, 15 subsets consisting of 8 projections per subset and 4 iterations were used. 8 projections per subset were used to ensure that the subset balance condition was maintained [14]. As in chapter 4, the reconstruction was stopped if the following 2 criteria were satisfied: (i) the reconstructed image was visually judged to be acceptable, and, (ii) between 2 iterations, change in the Chi-squared difference between the current and measured projections, was less than 0.1%. The number of iterations satisfying these criteria was 4 for all SPECT studies. A depth independent Gaussian collimator blur with standard deviation equal to 4.0 mm (corresponding to a SPECT FWHM of 9 mm) was applied. All reconstructed SPECT images were post-reconstruction filtered by a 3D Butterworth filter (cutoff frequency 0.64 cycles/cm, order 5). The reconstructed SPECT images were registered to common spatial co-ordinates.

5.2.5. Quantitation

For the phantom, defect studies were compared to the normal phantom study. Three-dimensional automated quantitation methods were used. For defect and normal studies reconstructed with each attenuation map, 3 parameters were calculated. These were: defect-to-normal Average Radial Maximum ratio for the infero-basal segment (using segmental analysis), Maximum Defect Contrast, and Defect Volume. In addition, we evaluated, using segmental analysis, uniformity of the normal myocardium and difference from CT.

Segmental analysis: The reoriented myocardium was divided into 9 segments by using PERFIT program, as described in section 4.2.5. The division of the myocardium into segments is illustrated in Fig. 4.2 in Chapter 4. The ARM values were further analyzed to calculate defect-to-normal ARM ratio for the infero-basal segment, uniformity of normal myocardium and difference from CT.

Defect-to-normal ARM ratio for the infero-basal segment: For all defect studies, for each reconstruction, the ratios of ARM values between each defect and normal studies were calculated. For the simulated RCA defect, the maximum decrease in ARM values for all the

images was found in the infero-basal segment. Only the ratios from this segment are presented.

Uniformity of normal myocardium: To assess the uniformity of counts in the normal myocardium, four ratios were calculated for UNIF projections reconstructed with each attenuation map. These were the ratios of Anterior basal ARM to Inferior basal ARM, Anterior Mid ARM to Inferior Mid ARM, Lateral Basal ARM to Septal Basal ARM, and Lateral Mid ARM to Septal Mid ARM.

Difference from CT for normal myocardium: To assess the variation in the same SPECT image due to using different attenuation maps, nine ratios were calculated for the UNIF acquisition, by dividing the ARM counts for each segment by the corresponding ARM counts for the CT attenuation map.

Maximum defect contrast and Defect volume: For all defect studies, for each attenuation map, the measured maximum defect contrast and defect volume was calculated as described in section 4.2.5.

The defect volume was calculated by difference-based region-growing between normal and defect studies. Due to partial volume effect, the defect volume calculated by this method is strongly dependent on the difference threshold used. For patient studies this threshold can be determined automatically from the normal mean and variation template [120]. Obviously this cannot be done for only one normal phantom. Our aim in this analysis of defect volume was not to determine which attenuation map gives a value closest to the known defect volume, but to estimate the variation in defect volumes for all the attenuation maps used. Therefore, we chose a difference threshold for each defect contrast level such that the defect volume corresponding to the TLS attenuation was closest to the actual volume. For each defect contrast level, this difference threshold was used to calculate defect volumes for all attenuation maps.

5.2.6. Error Analysis

Errors in quantitative results due to statistical variations in SPECT data were evaluated. In addition we evaluated, the coefficients of variation in UNIF ARM counts for each segment, due to statistical variations in SPECT data, and CT-TFS registration errors.

Statistical variations in SPECT data: To estimate the statistical variation in SPECT data regardless of the gamma camera used for acquisition, the SPECT measurement simulating normal myocardial perfusion (UNIF), was repeated four times. These measurements were performed using the ADAC Genesys, and the dual-headed Picker PRISM 2000. For the Picker Prism 2000, only one head was used for acquisition. The activity in the cardiac insert and acquisition parameters were the same as UNIF.

Each repeated acquisition was reconstructed with OSEM using the CT attenuation map and registered to the UNIF image. The variation of ARM counts for each segment, maximum defect contrast and defect volume were estimated by comparing the defect studies to each of the five normal studies. The variation of UNIF ARM counts for each segment, was also evaluated by comparing all the normal studies.

For TLS, TFS, CT FILL and TFS FILL attenuation maps, the variation of ARM counts for each segment, maximum defect contrast and defect volume were not directly available. However, with the reasonable assumption that the variations in quantitative results for these attenuation maps are equivalent to the corresponding variations for the CT attenuation map, which are actually estimated, the quantitative results for all five attenuation maps were compared using a Student's t-test.

CT-TFS registration errors: To assess the variability of final UNIF quantitation due to registration error between the transmission maps and CT, the following tests were done. The CT attenuation map was misaligned using 10 different combinations of position and tilt parameters and subsequently registered to the TFS attenuation map; the angles were changed from – 6° to 6° and the shifts between –8 to 8 pixels. (These were realistic misalignments). UNIF projections were reconstructed with the OSEM algorithm, using the misaligned and re-registered CT attenuation maps. The reconstructed projections were reoriented and average radial maximum for each segment were calculated using PERFIT program. For each segment, the mean and standard deviation for all 10 UNIF images were calculated.

5.3. Results

Registered Attenuation maps: From Fig. 5.1, it can be seen that the Teflon spine is clearly visualized in all CT, TLS and TFS attenuation maps. In the CT attenuation map, the plexiglass "top" of the cardiac insert is clearly visualized. In the TLS and TFS attenuation maps, this cannot be distinguished visually from water.

Table 5.2 shows linear attenuation coefficients obtained from the CT, TLS and TFS attenuation maps obtained by ROI analysis. For the TFS images, rather than calculating narrow-beam attenuation coefficients by measuring buildup factor, we scaled the attenuation coefficient corresponding to water to narrow-beam attenuation coefficients. For water and spine, this gives attenuation coefficient values comparable to those obtained from TLS (Table 5.2). The mean counts in the lungs, however, are significantly elevated when compared with CT or TLS (0.019 1/cm as opposed to 0.001 1/cm from CT, and 0.004 1/cm from TLS).

Table 5.2. Attenuation coefficients obtained from CT, TLS, TFS attenuation maps (all units in 1/cm).

	Narrow-beam	CT		TLS		TFS	
		Mean	S.D.	Mean	S.D.	Mean	S.D.
Water	**0.153**	**0.151**	**0.010**	**0.147**	**0.014**	**0.152**	**0.019**
Spine	**0.291**	**0.278**	**0.022**	**0.244**	**0.011**	**0.251**	**0.015**
Lungs		**0.001**	**0.001**	**0.004**	**0.003**	**0.019**	**0.007**

Fig. 5.2 shows the CT attenuation map and registered UNIF images overlaid. Fig. 5.3 shows short axis slices of the processed UNIF images, for each reconstruction. Fig. 5.4 shows short axis slices of DEF75 images registered to UNIF, for each reconstruction. Since all SPECT images were registered to common spatial co-ordinates, the short axis slices in Fig. 5.3 and 5.4 correspond to the same position in the cardiac insert.

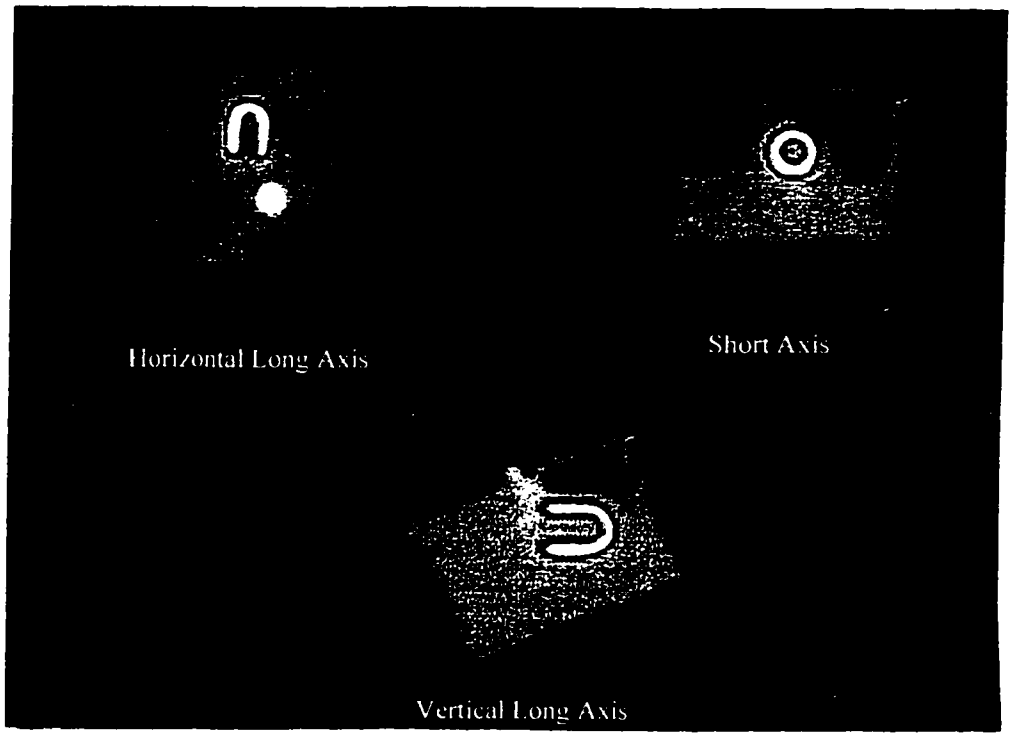

Fig. 5.2. CT attenuation map and registered UNIF (OSEM CT) images shown overlaid. Horizontal Long Axis, Short Axis, Vertical Long Axis.

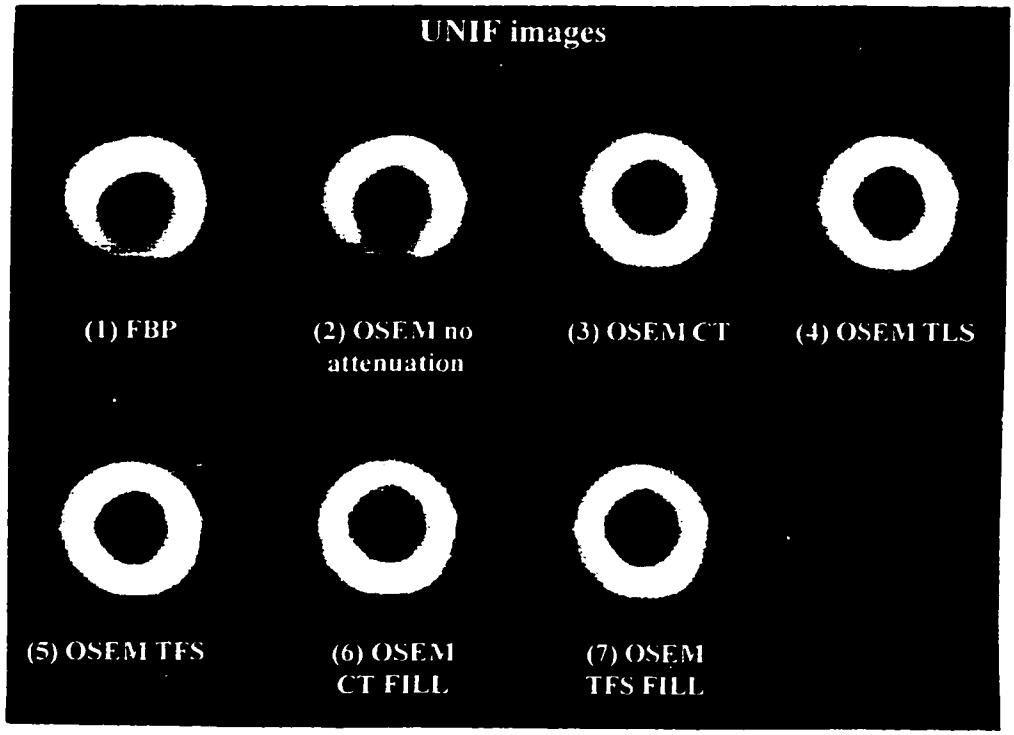

Fig. 5.3. Short-axis slice of processed UNIF images (SPECT study simulating uniform myocardium). (1) FBP, (2) OSEM with no attenuation compensation, (3) OSEM with CT,

(4) OSEM with TLS, (5) OSEM with TFS, (6) OSEM with CT FILL, (7) OSEM with TFS FILL.

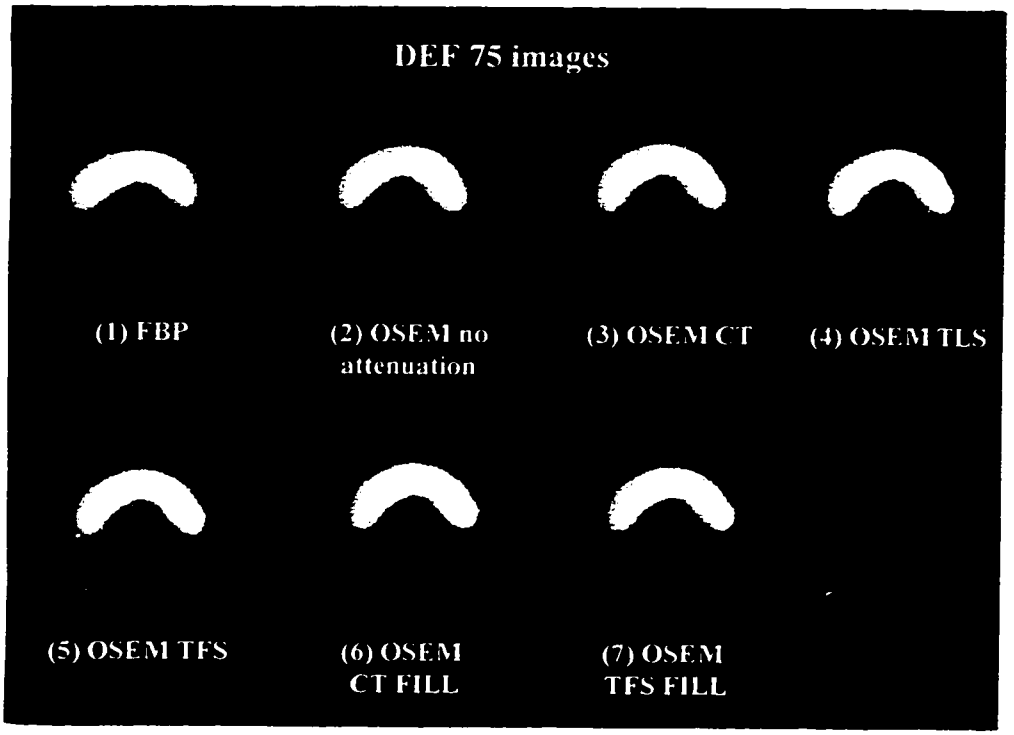

Fig. 5.4. Short-axis slice of processed DEF75 images (SPECT study simulating RCA defect with 75% contrast). (1) FBP, (2) OSEM with no attenuation compensation, (3) OSEM with CT, (4) OSEM with TLS, (5) OSEM with TFS, (6) OSEM with CT FILL, (7) OSEM with TFS FILL. The slices in Fig. 5.3 and 5.4 correspond to the same position in the cardiac insert.

Quantitation: The quantitative results comparing defect studies to normal are presented in Fig. 5.5 – 5.7. Fig. 5.5 shows, for each defect study, a graph of defect-to-normal ARM ratio (for the infero-basal segment), for each reconstruction. Fig. 5.6 shows, for each defect study, a graph of maximum defect contrast for each reconstruction. Since the specific activity of the defect and the myocardium were known for each study, the actual defect contrast and defect-to-normal segment ratio for each study are known. Fig. 5.7 shows, for each defect study, a graph of defect volume for each attenuation map.

In Fig. 5.5-5.7, the dashed lines indicate the estimated error due to statistical variations in the SPECT data, in the quantitative results corresponding to reconstruction with the CT attenuation map. For each quantitative parameter and each defect study, the standard deviation due to variation in emission data was calculated. The error in each quantitative

parameter was taken to be two times the standard deviation due to variation in emission data.

Defect-to-normal ARM ratio for the infero-basal segment: For all three defect studies, the differences in infero-basal segment defect-to-normal ARM ratio due to use of the various attenuation maps are < 9% (Fig. 5.5). These differences are within the statistical error range.

Maximum defect contrast: For all three defect studies, maximum defect contrast for images reconstructed with OSEM with attenuation correction are higher than the images reconstructed with FBP or OSEM with no attenuation correction (Fig. 5.6). The increase is maximum for the low contrast (DEF75) study. For all defect studies, the differences in maximum defect contrast due to use of the various attenuation maps are < 15%.

It can be seen from the graph that, for all defect studies except DEF75, these differences are within the statistical error range. For DEF75, CT FILL and TFS FILL fall just below the lower limit of error. Since only the study simulating normal myocardial perfusion was repeated, these limits may underestimate the actual statistical variation in the emission data; these values are probably within error.

Defect volume: Fig. 5.7 shows, for each defect study, a graph of defect volume for each attenuation map. The volume of the defect was measured to be 11.2 ml, and agrees with the value supplied by the manufacturer of the phantom.

For all the images compared, except DEF25 corrected with TFS attenuation map, the differences of calculated defect volumes for each attenuation map from CT were < 25%. For only the DEF25 study reconstructed using TFS attenuation map, the difference in defect volume with defect volume using CT attenuation map was 42%. All these values are well within the statistical error range (Fig. 5.7).

T-test results: From the t-test, for DEF 75 maximum defect contrast, the CT FILL attenuation map was found to be significantly different from the CT attenuation map ($p<0.05$; the p-value was ~0.04). In addition, for DEF 75 maximum defect contrast, the TFS FILL attenuation map had a low p-value (p~0.08). For all other quantitative results and all other studies, TLS, TFS, CT FILL and TFS FILL attenuation maps were found not to differ significantly from CT (the range of p-values was from 0.2 to 1). As mentioned previously, for the DEF 75 study, the maximum defect contrast values for the CT FILL

and TFS FILL attenuation maps are slightly less than the lower limit in the error range (Fig. 5.6). The low p-values correspond to this trend in this graph. If the defect acquisition were to be repeated in addition to the normal phantom study, we would expect the error range to be wider, and the p-values to be larger.

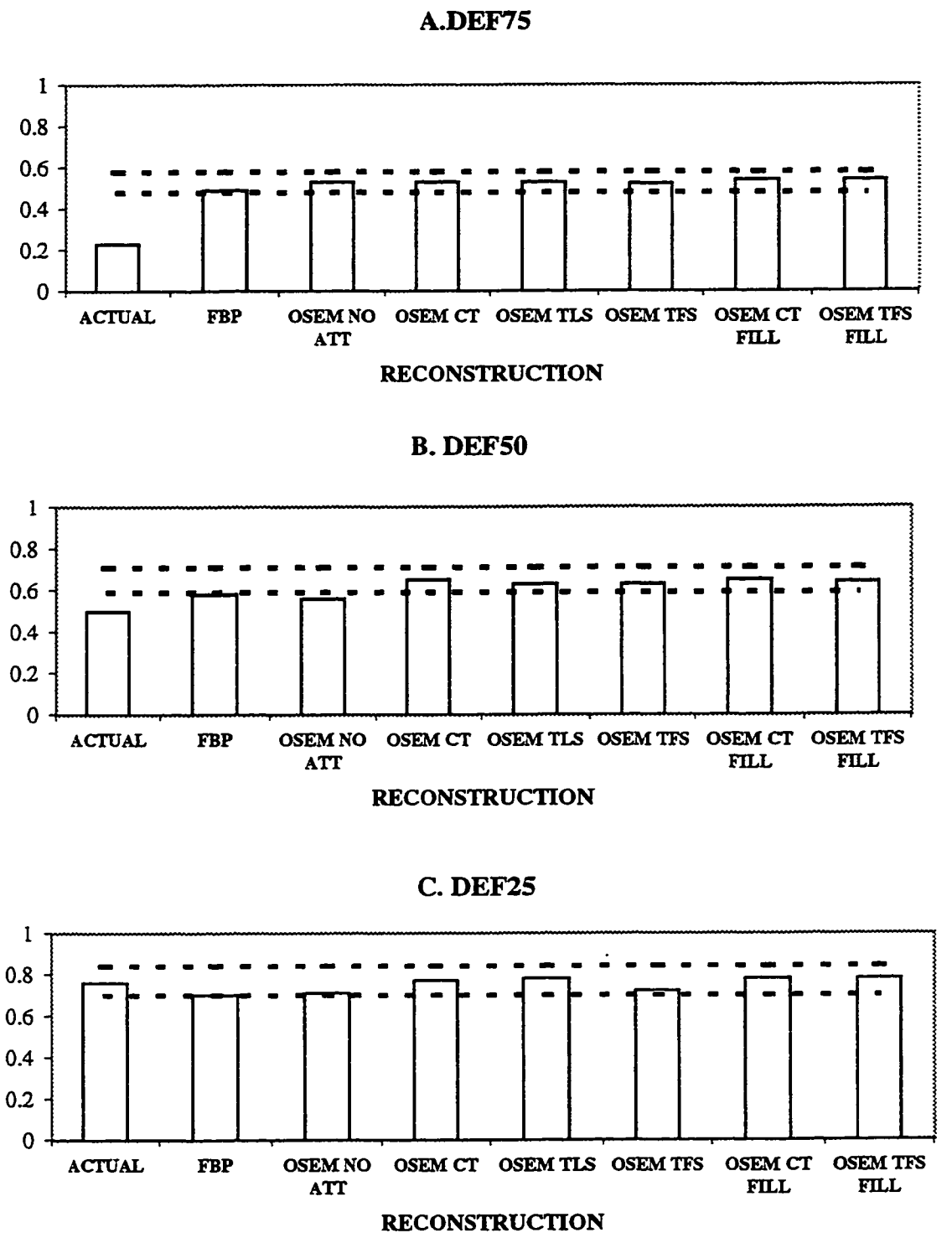

Fig. 5.5. Defect-to-normal ARM ratio for infero-basal segment for each reconstruction. **A.** DEF75 **B.** DEF50 **C.** DEF25.

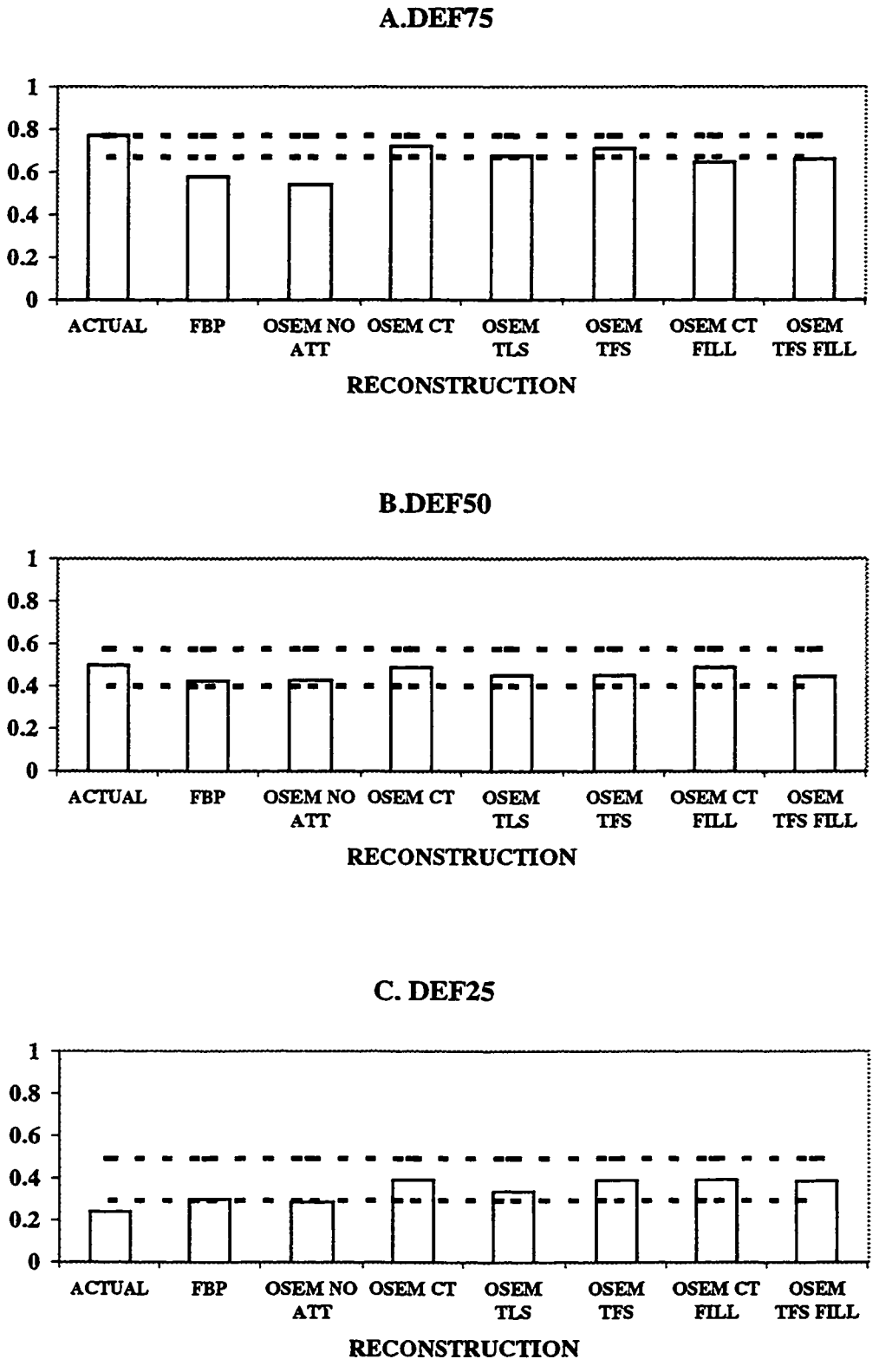

Fig. 5.6. Maximum Defect Contrast for each reconstruction. **A.** DEF75 **B.** DEF50 **C.** DEF25.

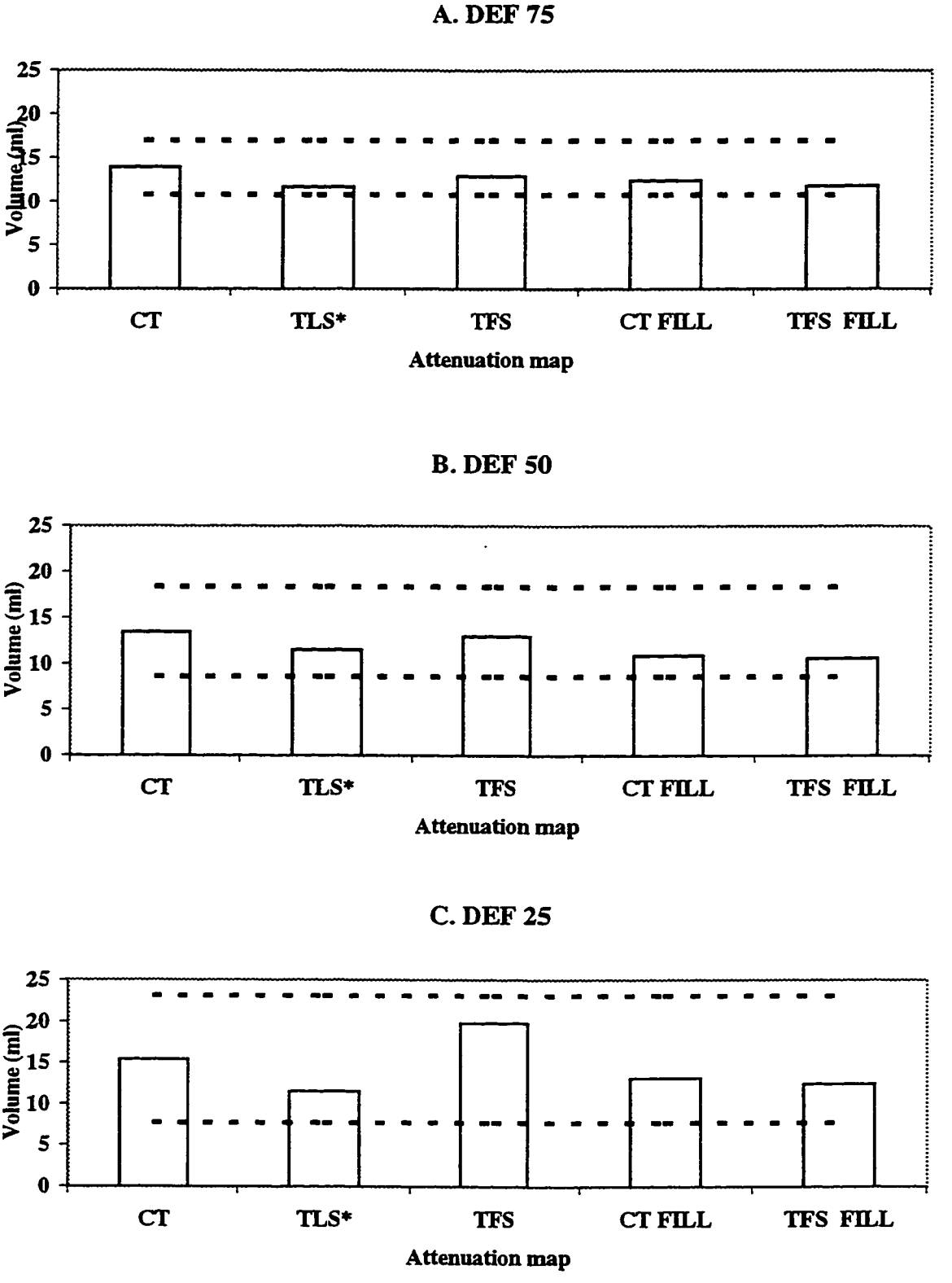

Fig. 5.7. Defect volume for each attenuation map. **A.** DEF75 **B.** DEF50 C.DEF25.(*Thresholds adjusted to give correct volumes for TLS attenuation map).

Uniformity of normal myocardium: Table 5.3 shows ratios of anterior/inferior and lateral/septal ARM values for the basal and mid segments for the different attenuation maps. Ideally, these ratios should be 1.00. It can be seen that uniformity of normal myocardium after attenuation correction is much improved. The TLS attenuation map gives the most uniform myocardium. The anterior/inferior basal and mid segmental count ratios for TLS are more accurate than those corresponding to CT by 10%. These ratios are also more accurate than those corresponding to CT FILL and TFS FILL by 13% and 14%. This slightly decreased activity in the inferior wall for CT, CT FILL and TFS FILL can be visually seen in Fig. 5.3.

Difference from CT: The normal study UNIF was reconstructed using all five attenuation maps. Table 5.4 shows ratios of segmental ARM counts for each attenuation map to segmental ARM counts in CT. From Table 5.4, we can see that between CT and TLS, there is up to 10% difference in ARM counts in each segment. Between CT and TFS, the maximum variation is 16%. For CT FILL and TFS FILL however the variation is < 5%. We found that SPECT images reconstructed using CT, CT FILL and TFS FILL attenuation maps are very similar in appearance to each other (Fig. 5.3, 5.4).

Error Analysis: Table 5.5 shows the errors in ARM counts for each segment, due to statistical variation in SPECT data for CT attenuation map, and CT-TFS registration errors. The effect of CT-TFS registration errors on final quantitative results for 90 measurements (9 segments for each of 10 misalignments) are small, the coefficient of variation is < 2% for all segments (Table 5.5).

Table 5.3. Uniformity of normal myocardium: Anterior/Inferior and Lateral/Septal ARM ratios for UNIF.

	TRUE	FBP	OSEM NO ATT	CT	TLS	TFS	CT FILL	TFS FILL
Anterior/ Inferior Basal	1.00	1.34	1.31	0.90	1.02	0.97	0.90	0.91
Anterior/ Inferior Mid	1.00	1.54	1.48	0.90	1.00	0.97	0.87	0.86
Lateral/ Septal Basal	1.00	0.97	1.10	0.98	0.99	1.05	1.00	1.01
Lateral/ Septal Mid	1.00	1.05	1.12	0.90	0.90	0.93	0.88	0.89

Table 5.4. Difference from CT for normal myocardium: Ratio of ARM counts for each segment to corresponding ARM for CT.

Segment	CT	TLS	TFS	CT FILL	TFS FILL
Anterior Basal	1.00	1.02	1.12	1.01	0.99
Lateral Basal	1.00	1.01	1.16	1.01	1.00
Inferior Basal	1.00	0.90	1.04	1.01	0.98
Septal Basal	1.00	0.99	1.08	0.99	0.97
AnteriorMid	1.00	1.00	1.08	1.01	1.00
Lateral Mid	1.00	0.94	1.10	0.98	0.98
Inferior Mid	1.00	0.90	1.00	1.05	1.04
Septal Mid	1.00	0.96	1.06	1.01	0.99
Apex	1.00	1.00	1.05	1.02	1.03

Table 5.5. Error in ARM counts for normal myocardium due to a) Statistical variation in emission data, b) CT-TFS registration errors.

Segment	a) Statistical variation of emission data: Coefficient of Variation (%)	b) CT-TFS registration errors: Coefficient of Variation (%)
Anterior Basal	**3.1**	**0.37**
Lateral Basal	**5.3**	**0.45**
Inferior Basal	**3.2**	**0.65**
Septal Basal	**2.6**	**0.39**
Anterior Mid	**1.8**	**0.36**
Lateral Mid	**2.9**	**1.02**
Inferior Mid	**3.5**	**0.38**
Septal Mid	**2.1**	**0.40**
Apex	**3.1**	**0.53**

5.4. Discussion

Quantitative results: Our results indicate that the differences in all 3 quantitative parameters (defect-to-normal ARM ratio for the infero-basal segment, maximum defect contrast, defect volume) due to use of the five attenuation maps are mostly small and within the range of the estimated statistical error.

The TFS attenuation map was obtained by linear scaling of RNT images obtained by using an uncollimated flood source. Thus, it has the most scatter and noise, with the value of the attenuation coefficient for lungs deviating the most from both CT and TLS attenuation maps (Table 5.2). Our results show that even using this noisy, poor quality attenuation map, the quantitative results are not significantly different from CT. Our results also show that attenuation maps obtained by segmenting noisy RNT attenuation maps yield quantitative results similar to CT. It can be seen that quantitative results using both CT FILL and TFS FILL attenuation maps are within error range of those obtained using CT (Fig. 5.5-5.7).

These results suggest that quantitative results using segmented CT images are not significantly different than those obtained by using CT images linearly translated to the SPECT emission energy. Furthermore, the segmented CT map has more precise geometric delineation of the phantom outer boundary, lungs and spine than the segmented TFS map. Precision of delineation, therefore, causes no significant difference in the final quantitative results.

Galt et al [110] have estimated attenuation maps by segmenting sheet source transmission images using a similar segmentation algorithm. This work compares use of such attenuation maps to use of dual scanning line source and CT attenuation maps. Although several investigators have used a transmission sheet source to obtain attenuation maps [78, 27, 108-110], there are several disadvantages to using a sheet source which makes it difficult to apply this method to routine clinical practice [78]. For example, for single-headed gamma cameras with no counter-balance, a special holder is required to keep the source in place, and this arrangement is cumbersome when used clinically [78]. For multiple-headed cameras, the source may partially or completely block the other camera heads [78]. If Tc-99m is used, the sheet source must be prepared each day, mounted to the holder before the transmission scan, and unmounted after; all these require a technologist's time and exposure [78]. If an uncollimated sheet source is used (as in this work), the added exposure to both the technologist and the patient is significant. While the problem of designing a special holder can be overcome, as in our case, if a single-headed gamma camera with a counterbalance is used, the time required to acquire such transmission maps is clinically not feasible. Using segmentation, Galt et al [110] have shown that the acquisition time can be shortened to 11 min [110]. If applied to clinical practice, the most evident problem with this method is that of registering transmission images to SPECT. If the transmission images are acquired following SPECT acquisition in the same spatial orientation as SPECT, the transmission images are contaminated by scattered emission photons, and the segmentation algorithm may not work well for all patient studies. Because of these difficulties, we are now investigating emission-based and scatter window based methods for patient studies.

It is conceivable that with segmentation, attenuation maps using fast transmission methods, emission-based methods or scatter window based methods may be comparable to

using dual scanning line source or CT attenuation maps; however, further work using such attenuation maps needs to be done to verify this. Pan et al [113] have achieved good agreement in the estimation of the body regions by segmenting photopeak images and using the scatter window, for phantoms and patients. As pointed out by the authors, segmentation of the lungs has to be more automated before the method can be applied clinically.

Since in patients, as opposed to phantom studies, the density of lungs and soft tissue varies, the validity of assigning a uniform attenuation coefficient to each region should be verified by patient studies. However, we would like to point out that attenuation maps have been obtained by segmenting transmission images and successfully applied to attenuation correction in cardiac positron emission tomography [129-130]. Xu et al [129] have performed PET attenuation correction for a phantom and patients using attenuation maps obtained by segmenting fast transmission images; the segmentation scheme was based on thresholding the transmission image histogram, similar to the method outlined in this paper. Meikle et al [130] have used attenuation maps obtained by smoothing and segmentation from fast transmission images for attenuation correction in a phantom and patients.

From Table 5.2, it can be seen that there is a 4.5% difference between the linear attenuation coefficient value obtained for Teflon from CT attenuation map and its corresponding narrow-beam value. This is probably because linear scaling of CT images by the ratio of linear attenuation coefficients for water is not exactly accurate for materials containing high atomic number such as bone; it has been shown by LaCroix et. al. to cause errors in spinal bone attenuation coefficient of up to 42% [90].

Uniformity of normal myocardium: From Table 5.3, it can be seen that of all five attenuation maps, the TLS attenuation map gives a more uniform normal myocardium than CT, TFS, CT FILL and TFS FILL. From Table 5.3, it can be seen that for TLS, attenuation coefficients for water and spine are smaller than their corresponding narrow-beam attenuation coefficients. The CT attenuation map is scaled to narrow-beam linear attenuation coefficients, and CT FILL and TFS FILL attenuation maps are filled with pre-assigned narrow-beam linear attenuation coefficients. When CT attenuation maps scaled to the slightly lower value of the linear attenuation coefficient for water for TLS are used, both

the anterior/inferior basal and anterior/inferior mid segmental ratios improve to 0.93. Therefore, CT attenuation maps translated to linear attenuation coefficient of water corresponding to TLS gives better quantitative results than CT attenuation maps translated to the narrow-beam linear attenuation coefficient of water. For SPECT scatter correction, we are using a dual-energy window scatter subtraction method using a scatter subtraction factor of 0.50. This result is therefore not surprising since our scatter fraction is not exact. These results suggest that, if CT attenuation maps translated to narrow-beam attenuation coefficients are used, the scatter fraction must be estimated more precisely for accurate quantitation. Similar results have been observed by Hasegawa et. al. [89], who found that the use of CT attenuation maps overestimated the activity in the cardiac chamber by about 10%, and that this error was reduced to 5% when the CT attenuation maps were modified to an "effective" linear attenuation coefficient that includes scatter. This trend agrees with our results in Table 5.3.

Our results from Table 5.4 show that there may be up to 10% difference in the ARM values of normal myocardium between CT and TLS attenuation maps. This difference may be reduced if the scatter fraction in SPECT data is estimated accurately.

Error analysis: There are errors in quantitative results due to statistical variations in emission and transmission data. A simulation study has shown that for clinical transmission and emission statistics, the statistical noise in attenuation corrected reconstructed images are dominated by the emission statistics [131]. In this study, we repeated the normal phantom acquisition only. To estimate the true statistical variation, each defect acquisition should be repeated also.

Effects of TLS-TFS or TFS–TFS registration errors were not evaluated in this work, but we expect them to be less than the CT-TFS registration errors due to the fact that the radionuclide transmission images are closer in appearance to each other.

Future work: Since in patients, as opposed to phantom studies, the density of lungs or soft tissue varies, the use of attenuation maps obtained by segmenting and filling RNT images with pre-assigned linear attenuation coefficients should be validated by patient studies. It has been shown that TLS gives a more uniform normal myocardium than CT and that this is largely use of an approximate constant scatter fraction. We are currently working on more

exact estimation of the scatter fraction in SPECT. We are currently evaluating attenuation maps obtained by segmenting images acquired using emission-based and scatter window-based methods for patient studies.

5.5. Summary

In summary, attenuation maps obtained by scaling or segmenting noisy transmission flood source images are comparable to those obtained using X-ray CT and dual scanning transmission line sources, and can be used in cardiac SPECT without significant loss in quantitative accuracy.

PART II: CORRELATIVE IMAGE REGISTRATION

CHAPTER 6: CORRELATIVE IMAGE REGISTRATION – a literature review

6.1. Introduction

There are several instances in medical imaging in which it would be desirable to compare two sets of images on a voxel-by-voxel basis. The pair of image volumes to be compared may be from the same subject and same modality (intrasubject and intramodality), from different subjects within the same modality (intersubject and intramodality), or from the same subject but different modalities (intrasubject and intermodality/multimodality). For example, in Nuclear Medicine imaging, SPECT and PET mostly depict physiological function, and the images may have little anatomic information. Merging functional and anatomical images may therefore aid accurate anatomical localization of abnormalities [132, 133]. Voxel-by-voxel comparison of patient images, to a composite normal image for identification and localization of abnormalities [120-121] can facilitate clinical diagnosis. Assessment of prognosis of disease, or evaluation of therapy or surgery, may be facilitated by voxel-by-voxel comparison of serial scans of the same patient.

Unless the images are mapped into common data co-ordinates, such voxel-by-voxel comparisons are not possible. The term "image registration" refers to the spatial mapping of two or more images into common data co-ordinates. The term "correlative (or multimodality) image registration" indicates registration of images obtained from a single subject using different modalities (e.g. SPECT and CT or SPECT and MRI).

Some of the clinical applications of image registration include [133]:

(i) mapping of functional SPECT (or PET images) to anatomical CT (or MRI images) for accurate anatomical localization of abnormalities, (ii) mapping of SPECT (or PET images) to an anatomic atlas for structural localization, (iii) mapping functional and/or anatomical images with 3-D treatment plans for dosimetry and treatment planning, (iv) comparison of SPECT or PET scans with a composite normal control image to identify

and localize abnormalities, (v) comparison of serial SPECT, PET or planar images of the same organ for imaging before and after surgery or other treatment, (vi) comparison of SPECT, PET or planar images of the same subject with two different radiopharmaceuticals to compare different functional assays, and (vii) quantitative assessment of SPECT or PET guided by analysis of registered anatomical CT or MRI images.

Several image registration algorithms have been proposed [120, 124, 132-143]. The bulk of them are applicable to brain imaging. Image registration algorithms can be broadly classified as prospective and retrospective. Prospective methods assume at the time of acquisition that it is known that the image will be used for matching, and special measures are included in the imaging protocol for registration. The use of stereotactic frames and external markers are examples of prospective registration. Retrospective methods are able to register the images without any modification to the imaging protocol. Retrospective methods are clinically more attractive since use of stereotactic frames or external markers inconvenience patient comfort and may not be clinically feasible. Several retrospective image registration algorithms have been proposed [120, 124, 132-133, 138-145]. Retrospective image registration methods are usually dependent on the image data and type of application, and no single method has been shown to work well on all data sets [132-133]. Since SPECT depicts function, retrospective registration of SPECT to anatomical CT or MRI images is particularly difficult. To use correlative image registration clinically, therefore, access to a wide range of registration algorithms is necessary [133]; in some cases, stereotactic frames or external markers have to be used.

6.2. Image registration techniques

6.2.1 Introduction

Any image registration method produces a set of equations that transforms the co-ordinates of each point in one image into the co-ordinates of the physically corresponding point in the other image. Typically, the transformation may include translation, rotation, and isotropic or anisotropic scaling of pixel coordinates. Non-rigid warping

transformations could also be used. If I and I' are two digital images (we want to register I to I'), with corresponding points P and P', then the coordinates of P and P' can be related as follows:

$$(x',y',z') = T(x,y,z,\mathbf{p})$$

where (x,y,z) are the co-ordinates of P, (x',y',z') are the co-ordinates of P', T is the registration function (the co-ordinate transformation) and **p** is a set of unknown parameters (eg. translations, rotations, scaling etc) of the registration function [133].
The image registration process can be divided into three general steps:

1. Selecting the mathematical criteria/ function between the two images that has to be optimized. This could be a predefined mathematical criteria or one determined by selecting corresponding points (control points or control features) in I and I'.
2. Determining the parameters **p** of the registration function T.
3. Resampling $I(T(x',y',z')$. This resampled image is registered to I'.

The most commonly used transformations that match the two images are rigid, affine and curved [132-133]. Rigid transformations are composed of translation, rotation, reflection and linear scaling. They are used when there are no spatial distortions or variability in geometric structures between the two images. They can be used, for example, for multimodality registration of brain images. A transformation is called affine when any straight line in the first image is mapped into a straight line into the second image, while parallelism is preserved. Examples of affine transformations include both uniform and non-uniform scaling, and shearing. Curved transformations may map a straight line into a curve. Curved transformations are also known as warping transformations. Warping may be used when one of the images has to be deformed to fit the other image, as in matching patient images with atlas data or in matching objects that change shape in between scans, e.g. abdominal studies [132]. These transformations may be global, that is, applied over the entire image, or local, applied locally.

Image registration can be performed in two or three dimensions. When 2-D methods are used for data obtained from 3-D patients, it is assumed that the images in the different

modalities are acquired in exactly the same plane. To meet this assumption, special positioning techniques are needed, which complicates the clinical imaging acquisition protocol. This is especially true for tomographic modalities, where a small variation in patient position may result in large changes in the reconstructed image. Such 2-D registration methods therefore cannot be retrospective, and the accuracy is rarely adequate [132]. Some registration methods are implemented in 2-D only for reasons of simplicity, computing power or memory usage. These techniques can be extended to 3-D, so the principles on which they are based on do not suffer from the limitations of the 2-D approach [132].

Based on the amount of interaction necessary, Van den Elsen et al [132] have classified registration methods as interactive or manual, semi-automatic and automatic. Manual methods need human interference for the determination of the transformation, for example, selection of landmarks on the two images. In semi-automatic methods, a computer determines the transformation, while user interaction is required to select image properties to be used in the registration, and/or starting, guidance or stopping of the registration procedure. Most registration methods fall into the semi-automatic category [132].

Many algorithms have been proposed for image registration. They can broadly be classified as stereotactic frame-based, landmark-based, surface-based, or voxel-based [132-133]. The review in this chapter is brief and concentrates mostly on the registration methods relevant to this thesis. More extended reviews of registration methods can be found in [132] and [133].

6.2.2. Stereotactic frame-based registration

Stereotactic frame based registration utilizes a rigid frame that is attached to the patient's head during both imaging and possibly surgery (or therapy), to define a consistent co-ordinate system within which to localize targets. The frame is usually attached by pins or screws fixed to shallow drill holes in the skull. The frame includes interchangable N-shaped or V-shaped fiducial marker plates for each modality. The markers are oriented such that enough cross-sections are present to determine the position

and orientation for each slice. Such fiducial markers are suited for CT, MRI, and may support PET [134-135] and digital subtraction angiography [140]. Frame-based registration is very accurate [146]. The accuracy is approximately 1 mm for DSA, CT and MRI within the scan plane and about half the slice thickness normal to the scan plane [132]. However the use of frames is inconvenient for the patient; the method cannot be applied retrospectively, and is applicable to brain only [132].

6.2.3. Landmark-based registration

Landmarks are used to identify corresponding points on two sets of images and to determine the parameters of the registration function. The landmarks can be external markers, anatomic markers or a combination of both. External markers are usually added to the skin of the patient. The markers may be detected manually, semi-automatically or automatically. The transformations used are generally global, and rigid or affine [132].

Like the stereotactic frame, external markers are also inconvenient and cannot be applied retrospectively [132-133]. Since acquisition of the two images can be separated by days, to reproduce the positions of the same markers can be problematic [132]. Indicating anatomic landmarks on the images is usually labour-intensive, and the accuracy of registration depends on correct identification of corresponding landmarks in all modalities [132-133]. The repeated precise application of external markers and identifying anatomical landmarks requires considerable operator expertise [133]. Despite such difficulties, landmark-based techniques are the most frequently applied registration method for registering multimodality extracranial images [133]. It has been argued that for the thorax and abdomen, external markers attached to the skin can be affected by movement of the skin relative to the internal structures [139-140], which can affect the registration accuracy. This would particularly be a problem with obese patients [140].

6.2.4. Surface-based registration

A popular surface-based 3-D registration method to register brain images, known as the "head and hat" algorithm, has been described by Pelizzari et al [138]. This algorithm was

originally used to register brain PET and MRI/ CT images. A surface model ("head") is extracted from the higher resolution image and related to a set of points ("hat") extracted from the contours of the lower resolution image, by a rigid or affine transformation. The "hat" is fitted on the "head" using an iterative search strategy that minimizes the mean-squared distance between the "hat" points and the "head" surface. Some user interaction is allowed to select the starting point, so that the algorithm converges to global minima rather than local ones, and to readjust the transformation parameters, for faster convergence.

An accuracy of one or two pixels of the lower resolution image has been achieved in phantom studies for CT, MRI and PET [147]. The method has been applied in registration of brain SPECT and MRI images [148]. Yu et al [140] have registered CT and PET scans of the thorax using a variation of this technique. Pallotta et al [144] have used surface matching of transmission attenuation maps for intersubject registration of PET images.

Surface-based registration requires delineation of corresponding surfaces in each of the image data sets. Since surface segmentation algorithms are strongly data and application dependent [132-133], surface-based registration methods cannot be successfully applied to a wide range of patient studies, especially in the case of functional images.

6.2.5. Moments-based registration

Another approach in image registration is the principal axes transformation, based on spatial moments matching [124, 149]. A rigid body is uniquely located by the knowledge of the position of its center of mass and its orientation with respect of its center of mass. The center of mass and principal axes (orthogonal axes about which the moments of inertia are minimum) can be determined for any rigid body. The registration consists of translating the image to its center of mass and rotating to align the image about the principal axes and scaling [124]. It can be applied to both surfaces and volumes. Registration errors of about 1 mm have been reported for volume registration of brain MRI, CT and PET images [124]. Moments-based registration methods are sensitive to incomplete scan coverage in either data sets and to differences in the volumes to be

registered [132-133]. It can be used as a first approximating step before applying another registration algorithm [120].

6.2.6. Voxel-based registration

A few voxel-based registration algorithms have been proposed [120, 141-143]. Woods et al [141] have described an automated voxel-based technique for MRI-PET registration of the brain. The MRI images are first edited to exclude non-brain structures such as skull, scalp and meninges. The edited MRI images are then partitioned into 256 components based on the MRI voxel values. The algorithm tries to register the images by iteratively maximizing the uniformity of the PET voxel values within each MRI partition. This is done by iterative minimization of a weighted average of the standard deviation of the PET voxel values corresponding to each MRI partition [141]. The algorithm is based on the following assumption: all voxels with a particular uniform value in the MRI images represent the same tissue type, and since the MRI and PET images come from the same subject, the corresponding PET voxel values should also be similar to each other.

Woods et al [141] have shown that this method provides robust and accurate registration if the skull, scalp and meninges are edited first. The registration error is less than one pixel of the lower resolution image. If the non-brain structures are not edited first, non-brain structures in the MRI images with voxel intensities similar to those for brain are often segmented into the same partitions as brain structures. This increases the standard deviations and makes the convergence criterion relatively insensitive to spatial orientation. Woods' algorithm, initially validated for MRI-PET registration, has also been applied successfully to MRI-SPECT registration [150].

Strother et al [146] have quantitatively compared 5 techniques for intrasubject image registration of the brain. Among the techniques compared were stereotactic frame-based registration, the "head and hat" method, landmark-based method, and Woods' method. This study found that fiducial markers that are not rigidly attached to the patient are inaccurate in comparison with the other techniques. Woods' method and stereotactic frame-based registration were found to be the most accurate.

Recently, voxel-based multimodality image registration using maximization of mutual information or relative entropy has been proposed [142]. The method applies mutual information criterion to measure the statistical dependence between the corresponding voxels in the two image data sets; it is assumed to be maximal if the two images are geometrically aligned. Maes et al [142] have used this criteria to automatically register MRI, CT and PET images, without any editing of the non-brain structures.

Correlation-based methods have been utilized for intramodality image registration [143, 145]. These methods are based on maximizing the correlation coefficient between two image data sets [143]. The technique is search-based, and iterative; for each iteration, the correlation coefficient is recalculated. Bacharach et al [145] have used this method for registering cardiac PET scans using attenuation maps to correct for changes in patient positioning. Collins et al [143] have used a principal axes transformation followed by a 3-D cross-correlation method for intersubject registration of MRI volumes to standardized atlas co-ordinates. Since pixel values in different modalities are usually not related, correlation-based methods are generally not successful for multimodality image registration [132-133].

Attenuation maps have previously been used for intersubject registration of PET images, but not for multimodality image registration. Pallotta et al [144] have used surface matching of transmission attenuation maps for intersubject PET registration. Bacharach et al [145] have used correlation of transmission attenuation maps for intersubject registration of cardiac PET scans. However, general use of attenuation maps for image registration is relatively unexplored.

6.3. Summary

To summarize, many multimodality image registration algorithms have been described in the literature. Most of them have been applied to the brain. Most current retrospective image registration methods are dependent on the image data and the type of scan; no single method has been shown to work well on all data sets, especially in the case of functional images [133]. To use correlative image registration clinically, therefore, access to a wide range of registration algorithms is necessary [133]; in some cases, stereotactic

frames or external markers have to be used. Attenuation maps have been utilized for intersubject registration of PET images, but not for multimodality image registration.

CHAPTER 7: APPLICATION OF RADIONUCLIDE TRANSMISSION ATTENUATION MAPS IN AUTOMATIC THREE-DIMENSIONAL MULTIMODALITY REGISTRATION[3]

7.1. Introduction

Correlative registration of images obtained from a single subject using different modalities (e.g. SPECT and CT or SPECT and MRI) is becoming increasingly useful for both research and patient care [133]. While most of the published work on multimodality image registration has been mainly devoted to brain imaging [124, 134-136, 138, 141-143], a few multimodality image fusions have been reported in other anatomical regions such as chest, abdomen, and pelvis [137, 139-140]. A large number of the proposed image registration algorithms use external markers or a combination of external markers and anatomical landmarks. Use of such markers or stereotactic frames can complicate acquisition protocols and may not be clinically feasible. In addition, external markers can be used for the brain but not for the thoraco-abdominal region because variable displacement of the skin relative to internal organs adversely affects the image registration [139]. Most automatic approaches are specific to a particular type of SPECT scan, and no single method works well on all image data sets as differences in the appearance of functional images may affect registration [133]. For the thorax and abdomen, in particular, there is a great need for robust automatic image registration methods, and very few have been proposed so far [139].

In this paper we propose a fully automated method for three-dimensional (3-D) image registration of X-ray Computed Tomography (CT) and SPECT, using radionuclide transmission (RNT) attenuation maps. This method is not specific to a particular type of SPECT scan, and does not require external markers. RNT attenuation maps, in the same

---

[3] The contents of this chapter have been submitted for publication. Application of radionuclide transmission computed tomography attenuation maps in automatic three-dimensional multimodality registration. Dey D, Slomka PJ, Hahn LJ, Kloiber R. J Nucl Med, submitted.

spatial orientation as SPECT, can now be acquired routinely using instrumentation for non-uniform attenuation correction (used mainly for cardiac SPECT imaging). Our work indicates that, in addition to non-uniform attenuation correction, RNT attenuation maps can be used to register SPECT images to CT robustly using automatic volume registration algorithms. Such an approach is independent of the quality of the functional scan.

Though in this work, we have shown preliminary results with an anthropomorphic cardiac phantom only, transmission attenuation maps in the same orientation as SPECT can potentially be applied to automatic multimodality image registration for SPECT scans of the brain, heart, lungs, breasts and abdomen, including oncological scans.

7.2. Methods

7.2.1. Image acquisition

We obtained CT scans, and SPECT scans paired with RNT attenuation maps of an anthropomorphic cardiac phantom with lung, cardiac and spine inserts (Data Spectrum Corporation, Chapel Hill, North Carolina).

CT: CT images were acquired on a GE Hispeed CT scanner (General Electric, Milwaukee, Wisconsin), using a peak voltage of 120 kV, 512x512 matrix, pixel size 0.94 mm/pixel and contiguous slices with slice thickness 5 mm.

SPECT-RNT: For SPECT acquisition, 660 microcuries of Tc-99m was placed in the myocardial insert. No background activity was placed in the phantom. SPECT acquisition was performed using a single-headed ADAC Genesys (ADAC, Milpitas, California) gamma camera. The acquisition parameters were 128x128 matrix, 120 stops over 360 degrees, 15 seconds per stop, and pixel size of 4.73 mm.

Following SPECT acquisition, radioactivity in the phantom was allowed to decay for over 48 hours. RNT images in the same orientation as SPECT were then obtained by using an uncollimated Tc-99m flood source and the collimated single-headed ADAC Genesys gamma camera. The flood source was filled with 20 mCi of Tc-99m and taped to the counterbalance of the gamma camera opposite the head. The acquisition

parameters were 128x128 matrix, 120 stops over 360 degrees, 15 seconds per stop, and pixel size of 4.73 mm.

7.2.2. Image pre-processing

In this work we registered RNT maps to both original CT images in Hounsfeld Units (HU) and to CT attenuation maps corresponding to 140 keV (CTMAP). To convert CT images to attenuation maps for 140 keV, the linear attenuation coefficient of water (μ_{CT}) corresponding to the effective energy of the CT scanner (E_{CT}) was calculated. By experimentally measuring the half-value layer for water at 120kVp, μ_{CT} was found to be 0.165 1/cm.

The CT images were converted to attenuation maps corresponding to photon energy of 140 keV by linearly scaling with the ratio of μ_{CT} to the known narrow beam linear attenuation coefficient of water at 140 keV (0.153 1/cm) (linear energy translation [90]) . The images were then rebinned from 512x512 to 128x128 matrix.

RNT: The measured transmission data were converted to integrals of linear attenuation coefficients [78], according to equation 5.1. These projections were then reconstructed by filtered backprojection with ramp filter and filtered by a three-dimensional post-reconstruction Butterworth filter. A frequency cutoff of 0.41 cycles/cm and order 5 was used. Because of scatter, the linear attenuation coefficients thus obtained do not correspond to narrow-beam attenuation coefficients. The mean counts corresponding to water in the phantom were determined by region-of-interest (ROI) analysis. The RNT images were then scaled by a factor such that the mean counts corresponding to water were equal to the narrow-beam linear attenuation coefficient for water at 140 keV (0.153 1/cm) .

SPECT: The SPECT images were corrected for scatter using a dual-energy-window subtraction technique [35]. The scatter fraction used was 0.5. Scatter corrected SPECT projections were reconstructed using an Ordered Subsets Expectation Maximization (OSEM) algorithm [14] with attenuation correction, using the CT attenuation map (CTMAP).

7.2.3. Automatic volume registration

Fig. 7.1 shows our SPECT-CT image registration technique. RNT attenuation maps, acquired in the same orientation as SPECT, were registered to CT and CTMAP images using automatic volume registration as described below. The 6 transformation parameters thus obtained (3 shifts and 3 angles) were applied to SPECT images. Since the RNT and SPECT images were acquired in the same orientation, this effectively registered the SPECT images to CT.

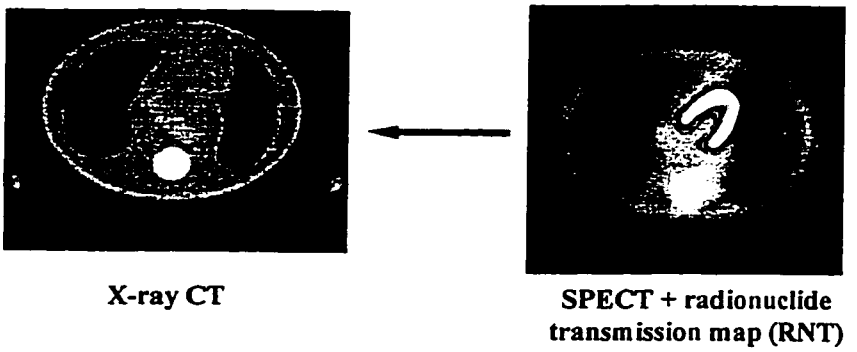

Fig. 7.1. Method for automatic SPECT-CT registration for anthropomorphic cardiac phantom using radionuclide transmission (RNT) attenuation maps.

All image registrations were done using Hermes Multimodality software (Hermes, Nuclear Diagnostics, Stockholm, Sweden) [122] on a Pentium Pro 200 MHz workstation. Image registrations were performed in two steps. First, an approximate image alignment was done using a technique based on principal-axes transformation [124]. Then a simplex minimization algorithm [125] was applied to the initial principal axes transformed image

by independently adjusting six transformation parameters: X shift, Y shift, Z shift, XY tilt, XZ tilt, and YZ tilt. Since the pixel sizes were known, the scaling in X,Y, and Z were constrained for all registrations.

We registered each set of images, using simplex minimization of 2 different convergence criteria – count difference [120], and uniformity index. Count difference is defined as the sum of the differences between the voxel values of the volumes to be registered [120]. Uniformity index, similar to the criterion used by Woods et al [141], is defined the sum of the voxel variances on the RNT image corresponding to each voxel intensity for the CT image. Our method differs from the method used by Woods et al in the minimization technique used [125].

The result of each image registration was visually assessed on all image slices in different orientations simultaneously. Two visual presentation techniques were used to verify the registered image accuracy: (1) a roving window display technique [120], (2) image overlay of the registered image with the image to be registered to [120].

7.2.4. Experiments

7.2.4 A. Comparison of automatic volume registration with manual landmark-based registration method :

To compare automated volume registration using count difference and uniformity index criteria to the commonly used method of registration using markers, the following tests were done.

Landmarks: A set of 9 landmarks were selected on the anthropomorphic cardiac phantom. 8 of these were plastic screws at various positions. The remaining landmark was the end of the spine insert. RNT images were registered to CTMAP using these landmarks.

The registered RNT images were then misaligned 6 times using various combinations of shifts and rotations; the angles were changed from – 6° to 6° and the shifts between –8 to 8 pixels. (These were realistic misalignments). The misaligned images were re-registered using landmarks.

Registration with simplex minimization of Count Difference: RNT images were registered to CTMAP using simplex minimization of count difference. The registered RNT images were misaligned 6 times using the same combinations of position and tilt parameters as for landmark registration. The angles were changed from – 6° to 6° and the shifts between –8 to 8 pixels. Each set of images were re-registered using simplex minimization of count difference.

Registration with simplex minimization of Uniformity Index: RNT images were registered to CTMAP using simplex minimization of uniformity index. The registered RNT images were misaligned 6 times using the same combinations of position and tilt parameters as for landmark registration. The angles were changed from – 6° to 6° and the shifts between –8 to 8 pixels. Each set of images were re-registered using simplex minimization of uniformity index.

In total, 26 registrations were performed, 6 for the manual landmark-based method, and 10 each for automatic volume registration using count difference and uniformity index.

3-D displacement from marker registration: For each of the misalignment tests, the six transformation parameters for each image registration method (landmark, automated volume registration using count difference and uniformity index) differ slightly from each other. For automatic volume registration using count difference and uniformity index, the *displacement from marker registration* was defined as the 3-D distance in mm corresponding to the differences in all six transformation parameters from the parameters corresponding to marker registration. For each misalignment test, 3-D displacement from marker registration for count difference and uniformity index was calculated for 5 anatomical markers at different positions in the phantom. From these numbers, the average 3-D displacements from marker registration were calculated for both convergence criteria.

3-D Registration reproducibility error: The reproducibility of marker registration, and automatic image registration were assessed in the following way.

For each misalignment test, the transformation parameters obtained after re-registration differ very slightly from zero. 3-D registration reproducibility error was defined as the 3-D distance in mm corresponding to these small residual errors in all six transformation parameters [151]. For each of the 26 misalignment tests corresponding to the 3

registration methods, 3-D registration reproducibility error was calculated for 5 anatomical markers at different positions in the phantom. For each registration method, the average 3-D registration reproducibility errors were calculated.

7.2.4 B. RNT-CT registration

RNT images were registered to the original CT images (in Hounsfeld Units) using simplex minimization of count difference and uniformity index. The registered RNT images were misaligned using 10 different combinations of position and tilt parameters; the angles were changed from – 6° to 6° and the shifts between –8 to 8 pixels. Each set of images were re-registered using automatic volume registration.

For each misalignment test, 3-D registration reproducibility errors for 5 anatomical markers were evaluated, and the average 3-D registration reproducibility error was calculated.

7.2.4 C. Effect of missing slices on RNT-CT registration

To assess the effect of missing slices on RNT-CT registration, 6 pairs of CT and RNT images were created by removing slices from the top and bottom. The percentage of slices missing varied from 9% to 53%. The truncated images were registered using simplex minimization of uniformity index.

Due to the missing slices, the transformation parameters differ from the transformation parameters corresponding to the untruncated data. 3-D registration error was defined as the 3-D distance in mm corresponding to these differences in the transformation parameters. For each registration, the 3-D registration errors for 5 anatomical markers were evaluated and the average 3-D registration error was calculated.

7.2.4 D. Effect of variability in CT voxel values on RNT-CT registration

To assess the effect of variability of CT voxel values on RNT-CT registration, 12 CT images were generated by varying the original CT voxel values in steps of 2 HU (These were realistic variations which could be expected in clinical situations). The resulting CT and RNT images were registered using simplex minimization of uniformity index.

Due to the variation in CT voxel values, the transformation parameters differ from those corresponding to the original CT data. 3-D registration error was defined as the 3-D distance in mm corresponding to these differences in the transformation parameters. For each registration, 3-D registration errors for 5 anatomical markers were evaluated and the average registration error calculated.

In addition, errors were evaluated qualitatively. For all experiments, the result of each image registration was visually assessed on all image slices in different orientations simultaneously, using roving window display and image overlay techniques.

7.3. Results

Fig. 7.1 describes the principle of our automatic SPECT-CT registration method using RNT attenuation maps. Fig. 7.2 shows volume rendered CT and SPECT images registered by this method.

7.3.1. Comparison of automatic volume registration with manual landmark-based image registration

From visual assessment, CTMAP and RNT images could be registered successfully using automatic volume registration with count difference and uniformity index as well as manual landmark-based image registration. The differences in registration parameters were not discernible by visual analysis.

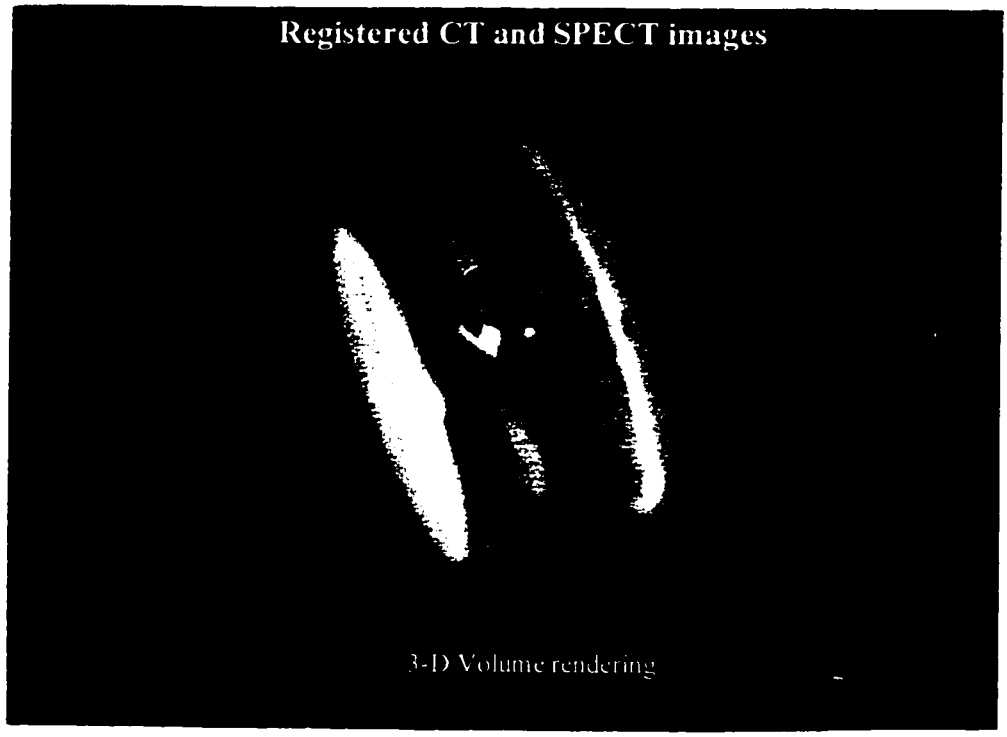

Fig. 7.2. Registered CT and SPECT images of the anthropomorphic cardiac phantom (3-D volume rendering).

Calculation times: All image registrations were performed on a Pentium Pro 200 MHz computer. For automatic volume registration using count difference, the average number of iterations was 96; each iteration took about 3.7 seconds. Each iteration involved trilinear interpolation of the whole dataset. The total calculation time for each registration was about 6.0 minutes. For uniformity index, the average number of iterations was 94; each iteration took about 2.7 seconds. Therefore the total calculation time for each registration took about 4.0 minutes. For manual landmark-based registration, the typical time to register the images was about 10 minutes; most of this time was spent in manually identifying and marking the landmarks. Both CTMAP and RNT images were in 128x128 matrix.

3-D displacement from marker registration: For all registration methods (automatic volume registration with count difference, uniformity index, and manual landmark-based image registration) there were small differences in the transformation parameters for each

misalignment test. Table 7.1 shows 3-D displacement from marker registration for automatic volume registration with count difference and uniformity index.

Table 7.1. 3-D displacement from marker registration for automatic volume registration with count difference and uniformity index (mean +/- s.d.).

	3-D displacement from marker registration (mm)
Count Difference	**2.5 +/- 1.2**
Uniformity index	**3.3 +/- 1.3**

Assessment of registration reproducibility: The results of the assessment of registration reproducibility for manual landmark-based registration, automatic volume registration using count difference, and uniformity index are shown in Tables 7.2 and 7.3. Table 7.2 shows the error in transformation parameters; Table 7.3 shows the 3-D registration reproducibility error.

From Table 7.3, it can be seen that the registration reproducibility of the automatic and manual image registration methods are comparable. All three values are within 1 standard deviation of each other. From Tables 7.1 and 7.3 it can be seen that the 3-D displacement from marker registration for both count difference and uniformity index are less than 3.5 mm. These values are less than one pixel and one slice separation, and within one standard deviation of reproducibility error for marker registration (2.3 +/- 1.0 mm). For the cardiac phantom, therefore, automatic volume registration with count difference and uniformity index is comparable to manual landmark-based registration.

Table 7.2. Registration reproducibility for manual landmark-based registration, automatic volume registration using count difference and uniformity index: error in transformation parameters (mean +/- s.d.).

Transformation parameters	Count Difference (n=10)	Uniformity Index (n=10)	Manual landmark-based registration (n=6)
X shift (mm)	0.4 +/- 0.1	0.4 +/- 0.4	1.3 +/- 0.8
Y shift (mm)	0.6 +/- 0.4	0.4 +/- 0.2	1.5 +/- 0.9
Z shift (mm)	0.3 +/- 0.3	1.7 +/- 0.3	0.2 +/- 0.2
XY tilt (degrees)	0.2 +/- 0.2	0.6 +/- 0.2	0.2 +/- 0.2
XZ tilt (degrees)	0.1 +/- 0.1	0.1 +/- 0.1	0.2 +/- 0.1
YZ tilt (degrees)	0.8 +/- 0.3	0.1 +/- 0.1	0.2 +/- 0.1

Table 7.3. 3-D registration reproducibility error in mm (mean +/- s.d.) for automatic volume registration using count difference and uniformity index, and manual landmark-based registration.

Image Registration method	3-D registration reproducibility error (mm)
Count difference	1.2 +/- 0.7
Uniformity index	2.1 +/- 0.5
Manual landmark-based method	2.3 +/- 1.0

7.3.2. RNT-CT registration

RNT images could be successfully registered to CT images (in HU) using count difference and uniformity index. For RNT-CT registration, for count difference, the average number of iterations was 120, and the time per iteration was 3.9 seconds. The total time per registration was therefore 7.8 minutes. For uniformity index, the average number of iterations was 96; each iteration took about 2.7 seconds. Therefore the total time for each registration was about 4.3 minutes. The matrix sizes for RNT and CT images were 128x128 and 512x512, respectively. For RNT-CT registration using simplex minimization of count difference, the 3-D registration reproducibility error was 1.0 +/- 0.6 mm. For uniformity index, the 3-D registration reproducibility error was 2.0 +/ 0.4 mm.

7.3.3. Effect of missing slices on RNT-CT registration

From visual assessment, for each pair of truncated RNT-CT images, automatic volume registration using uniformity index was found to register the images successfully. Fig. 7.3 shows the effect of missing slices on RNT-CT registration. From Fig. 7.3, it can be seen that the registration error remained relatively stable and at less than 5 mm for up to 54% slices missing from both volumes. If more than 54% of slices were missing from the volumes, the heart was severely truncated in the inter-slice direction.

7.3.4. Effect of variability in CT voxel values on RNT-CT registration

From visual assessment, for each CT image with altered CT voxel values, automatic volume registration using uniformity index was found to be successful. Fig. 7.4 shows the effect of variation in CT voxel values on RNT-CT registration. From Fig. 7.4, for differences in CT voxel values of +/- 10 HU, the registration error is less than 2 mm. These errors are comparable to the 3-D registration reproducibility error for RNT-CT image registration (2.0 mm).

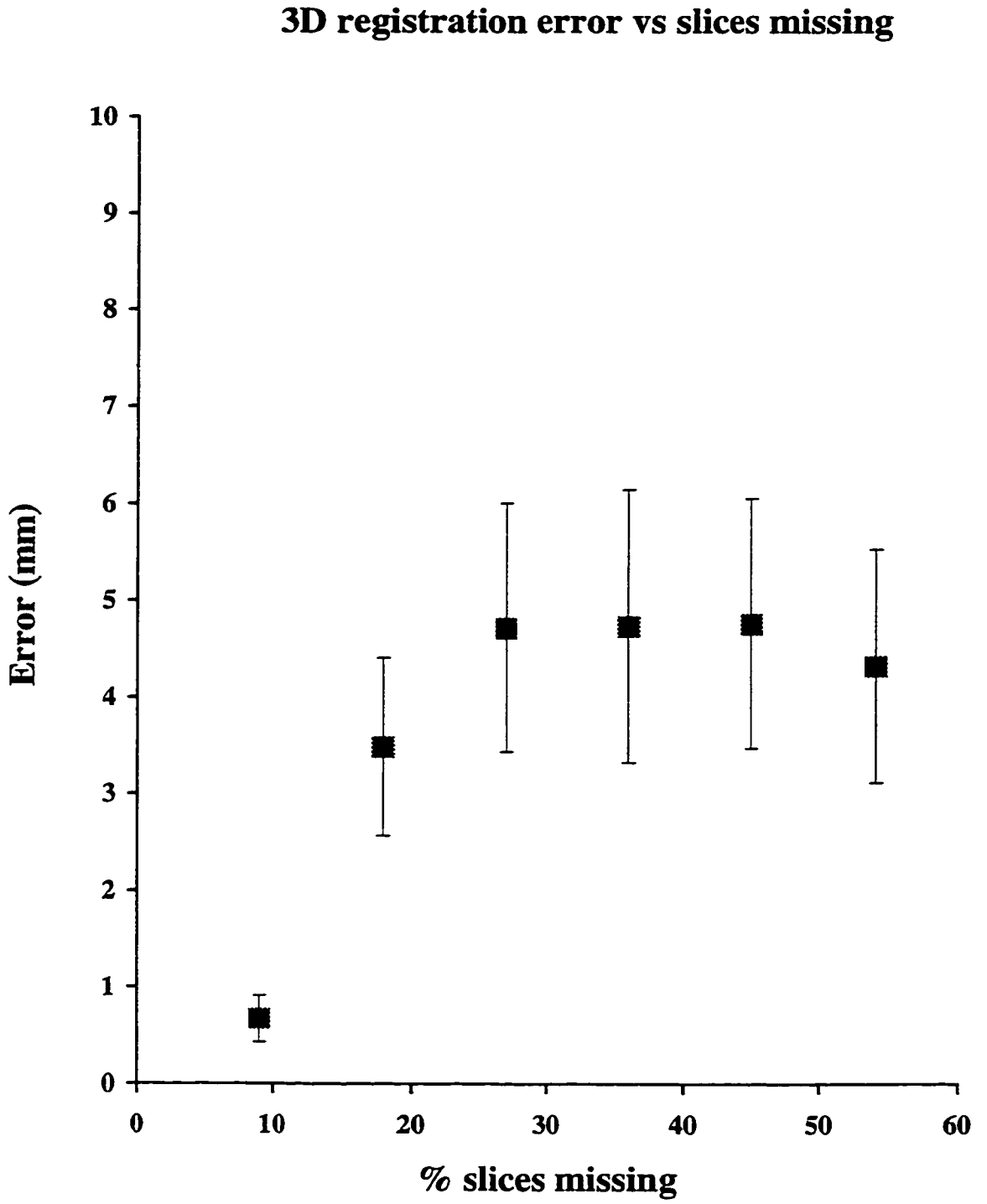

Fig. 7.3. Plot of 3-D registration error (mm) versus slices missing. Slices were removed from top and bottom for both RNT and CT images.

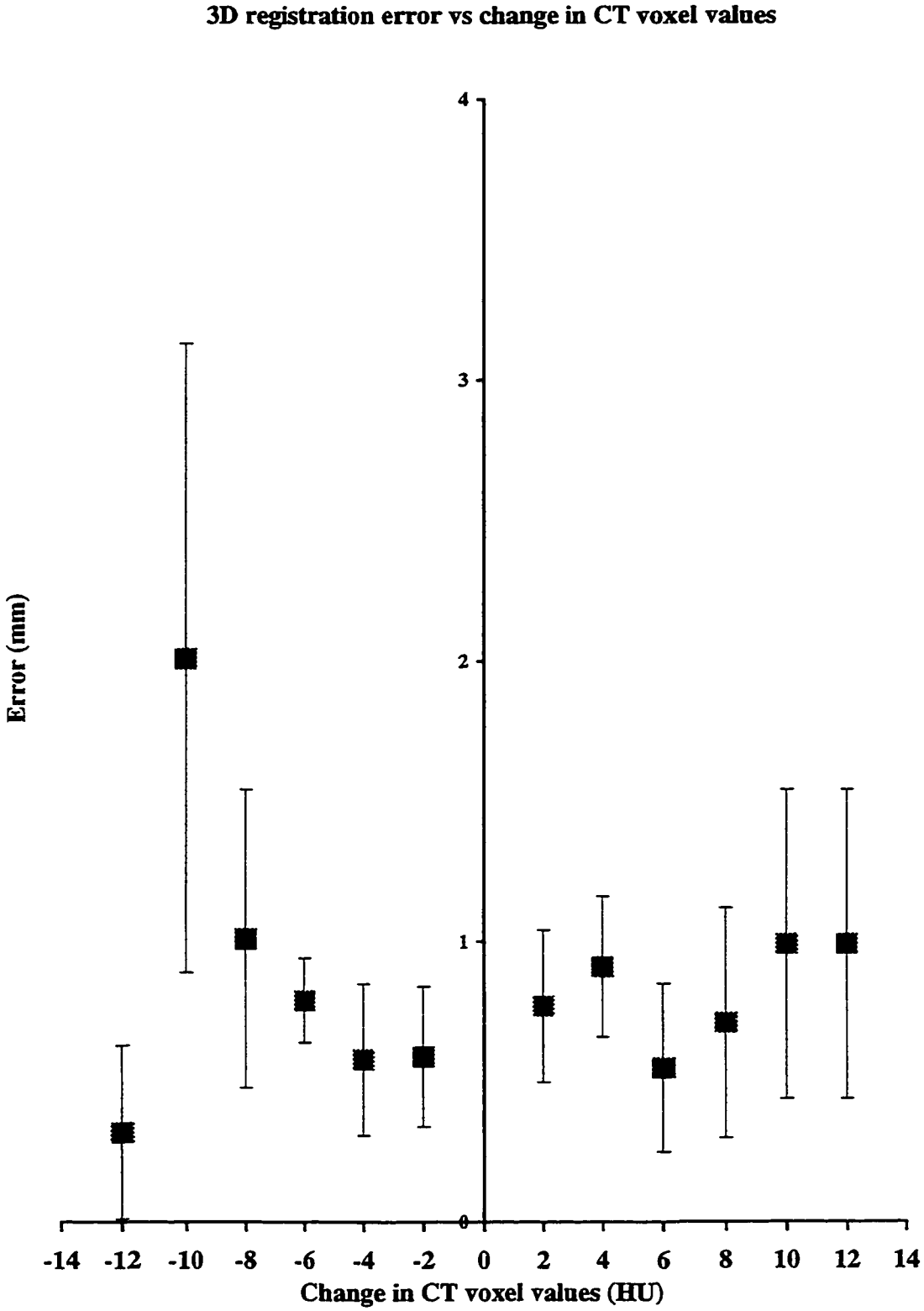

Fig. 7.4. Plot of 3-D registration error (mm) versus change in CT voxel values (HU).

7.4. Discussion

Comparison of automatic volume registration with manual landmark-based image registration: From our results, automatic volume registration using count difference and uniformity index are comparable to manual landmark-based image registration. The 3-D registration reproducibility error for all three registration methods are comparable, and the 3-D displacement from marker registration for both count difference and uniformity index are less than 3.4 mm, which is less than the dimensions of one voxel. The average times required to register the images using both count difference and uniformity index are less than that using landmarks. Automatic volume registration requires no operator intervention, and avoids difficulties associated with fiducial markers.

RNT-CT registration: Our results indicate that RNT maps can be successfully registered to raw CT images (in HU) using simplex minimization of count difference and uniformity index. With uniformity index, the registration algorithm was robust to missing slices of up to 54%, and was not affected significantly (< 2 mm) by realistic variation in CT voxel values.

Application of our method and future work: For a large majority of SPECT scans, there are no robust automated algorithms for multimodality image registration, and external markers or external markers and anatomical landmarks have to be used. Use of external markers or stereotactic frames are often not clinically feasible. For SPECT imaging in the thorax and abdomen, even external markers are not appropriate since variable displacement of the markers from internal organs affect image registration [139].

In this chapter, we have described a method for automated SPECT-CT image registration using RNT attenuation maps. Although we acquired RNT attenuation maps sequentially using an uncollimated flood source, for most current gamma cameras, RNT attenuation maps can be acquired simultaneously with SPECT [75]. Therefore acquiring the RNT maps does not increase patient imaging time significantly. The method is clinically feasible and can be implemented easily. Since RNT attenuation maps represent anatomy, they are independent of abnormal physiology, and are not affected by the

features and quality of SPECT images. The registration method is therefore also not affected by features and quality of SPECT images and is potentially applicable for automatic SPECT-CT registration for a wide range of SPECT scans. The method can potentially be applied to automatic multimodality registration of SPECT scans of the brain, heart, lungs, breasts and abdomen.

Our method could particularly benefit the correlation of oncological scans to CT. Accurate anatomical localization of the tumour can aid clinical diagnosis and treatment. As mentioned earlier, for oncological scans in the thorax and abdomen, even external markers are not appropriate because of variable displacement of external markers from internal organs. Our method could also be applied to SPECT imaging using newer agents targeting specific brain functions, for example, Dopamine D2-receptor imaging using I-123 labeled pharmaceuticals [152-153]. Since these images lack any anatomical information, accurate anatomical localization of the SPECT images is critical.

In addition to multimodality image registration for a single subject, transmission attenuation maps can also be used for inter-subject registration of SPECT images, which is useful for comparing serial SPECT scans, and for quantitative SPECT analysis. A common technique for quantifying cardiac and brain SPECT images is to compare each SPECT scan, on a voxel-by-voxel basis, to a database of normal patient studies [120-121, 151]. To perform voxel-by-voxel comparisons, it must be possible to accurately map patient images to common data co-ordinates. In a recent related work [chapters 4 and 5 of this thesis], we have used radionuclide RNT images to register SPECT images of an anthropomorphic cardiac phantom simulating different patient situations. Since anatomical RNT images are not influenced by abnormal physiology, they are more suitable for inter-subject registration than SPECT images. In recent studies, RNT attenuation maps have been utilized for inter-subject registration of cardiac PET images [144-145], however they have not been previously for multimodality registration.

Obtaining RNT maps in the same orientation as SPECT requires a gamma camera equipped with transmission imaging hardware. As mentioned in Chapter 3, such hardware is expensive. Transmission imaging can complicate the acquisition procedure, and slightly increase the dose to the patient. Some manufacturers acquire the RNT maps

sequentially [75]. This increases the acquisition time by about five minutes; the chances of patient motion between the emission and transmission scan are also increased.

7.5. Summary

To summarize, we have described an automated, clinically feasible method for SPECT-CT image registration, using radionuclide transmission attenuation maps. Such registration is not affected by features and quality of SPECT images, and avoids difficulties associated with the use of fiducial markers. The technique described in this preliminary work can potentially be extended to a wide variety of SPECT images.

CHAPTER 8: SUMMARY AND FUTURE WORK

8.1. Summary

8.1.1. Discussion

In this thesis, different methods and approaches to improve SPECT images corrupted by non-uniform attenuation and scatter, using radionuclide transmission attenuation maps, were quantitatively evaluated. In chapter 4, OSEM reconstruction and Chang's method have been quantitatively compared. They are shown to be quantitatively equivalent, however, OSEM attenuation correction gives a more correct activity distribution, with respect to both the homogeneity of the radiotracer and the shape of the cardiac insert. The calculation times for both methods are comparable.

In chapter 5, attenuation maps obtained by segmenting poor quality RNT images acquired using a transmission flood source have been compared to those obtained from X-ray CT and dual scanning line source RNT images. The differences in quantitative results due to using all five attenuation maps are small, and within the range of estimated error due to statistical variation of emission data. The quantitative results obtained using noisy poor quality attenuation maps are not significantly different from CT. Attenuation maps obtained by segmenting noisy RNT attenuation maps also yield quantitative results similar to CT. Such attenuation maps can be used in cardiac SPECT with no significant loss in quantitative accuracy. As discussed in chapter 5, estimating attenuation maps by utilizing the scatter window and emission-based methods are clinically more feasible than obtaining attenuation maps with a transmission flood source. These results strongly encourage further work in estimation of attenuation maps for patient studies by utilizing the scatter window and emission-based methods (section 8.2).

In chapter 7, it is shown that attenuation maps in the same orientation as SPECT can be used for correlative image registration. This can aid image interpretation and clinical diagnosis, and can be important in planning and evaluation of surgery and therapy. Using current commercial transmission hardware, for most current gamma cameras, attenuation maps can be acquired simultaneously with SPECT. The method is clinically feasible, does not significantly increase patient imaging time and can be implemented easily.

There are several implications of the results presented in this thesis, that can be applied to patient imaging situations. For non-uniform attenuation correction, Chang's method is implemented by a few gamma camera manufacturers [75]. Though a few investigators have used OSEM [11, 24-25], it is not yet widely used. In this thesis it is shown that OSEM, while quantitatively equivalent to Chang's method, gives a more correct activity distribution. Similar results have been observed for MLEM, but the drawback with the MLEM algorithm was its computing times. The computing times for OSEM and Chang's method are shown to be comparable. Thus the results encourage replacement of Chang's method with iterative methods.

For single headed gamma cameras, no commercially available transmission hardware is available. In such cases, our results verify that attenuation maps obtained by segmenting RNT images acquired using a transmission flood source can be used in cardiac SPECT with no significant loss in quantitative accuracy.

The results in Chapter 5 indicate that accurate estimation of the scatter fraction is essential for quantitative SPECT. As discussed in Chapter 5, if attenuation maps scaled to narrow-beam attenuation coefficients are used, the scatter fraction must be estimated precisely for accurate quantitation. There is up to 10% difference in the ARM values of normal myocardium between CT and TLS attenuation maps; this difference may be reduced if the scatter fraction in SPECT data is estimated accurately.

As discussed in chapter 7, for a large majority of SPECT scans, there are no working automated algorithms for multimodality image registration, and external markers or external markers and anatomical landmarks have to be used. The automated SPECT-CT image registration described in chapter 7 is clinically feasible and can be implemented easily. Since the registration method is not affected by features and quality of SPECT images, it can potentially be applied for automatic SPECT-CT registration for a wide range of scans.

Strengths of this study: The principal strengths of this study are that automatic 3-D image registration and quantitation methods were used. The use of automatic methods reduces intra-observer variability. The use of automated 3-D image registration methods

minimizes the effect of registration errors on quantitative results. As shown in Chapter 5, such errors are very small (<2%).

In contrast with conventional polar plot quantitation, the quantitative comparisons in this work were objective, direct and voxel-based. Usually, the cardiac images are reoriented individually, which leads to intra-operator variability, and polar plots are calculated by mapping maximal count values into a 2-D circular plot (see Chapter 3 of this thesis). In our method, to avoid subjectivity in our comparisons, prior to performing quantitation, all SPECT images were registered to common spatial co-ordinates using automated image registration. Instead of polar plot quantitation, three-dimensional voxel-based quantitation methods were used. The comparisons are therefore not based on mapped maximal count values, but on the counts in each voxel. Since the quantitation was three-dimensional, the results are representative of the entire volume and not of a particular 2-D slice.

Limitations of this study: The principal limitation of this study is that an anthropomorphic phantom with no background activity was used for all experiments. In patients there is often significant liver and visceral uptake. Such uptake varies from patient to patient. The radiotracer concentration in the liver can be twice or more than the concentration in the myocardium. As discussed in Chapter 3, scattered photons from the abdomen can affect the radiotracer concentration in the heart. For abdominal radiotracer uptake, estimation of an accurate pixel-by-pixel scatter fraction would be expected to be even more important. Abdominal activity can also make segmentation of the attenuation maps into soft tissue and lungs more difficult.

In patients, the lung density has been known to vary over the extent of the lung [78], and this is not adequately represented in the phantom where the lung density is uniform. The effect of segmenting and filling the lungs with a constant linear attenuation coefficient may therefore be more significant for patients than for the phantom. This effect of such segmentation can be evaluated for patients (section 8.2).

Image registration using RNT attenuation maps was applied to images of the anthropomorphic phantom only. The method has to be tested to patient image data. The method also needs to be tested for MRI-SPECT registration. Rigid transformations were

used image registration in the phantom. For patient image registration in the thorax and abdomen, which are strictly not rigid, it has been suggested that warping is necessary [139-140]. Automatic volume registration using RNT maps was compared with markers, however, validation of the registration method with stereotactic-frame based registration was not performed.

8.1.2. Conclusions

It has been shown in chapter 4 that OSEM and Chang's attenuation correction are quantitatively equivalent; however, OSEM attenuation correction gives a more correct activity distribution, with respect to both the homogeneity of the radiotracer and the shape of the cardiac insert. This difference in homogeneity between OSEM and Chang's method was found to be 7.9% or less for the UNIF study. Since the calculation times of both methods are comparable, OSEM attenuation correction is clinically applicable and preferred.

It has been shown in chapter 5 that attenuation maps obtained by segmenting RNT images acquired using a transmission flood source are comparable to those obtained from X-ray CT and dual scanning line source RNT images. Attenuation maps obtained by segmenting RNT images acquired using a transmission flood source can therefore be used in cardiac SPECT without significant loss in quantitative accuracy.

It has been shown in chapter 7 that radionuclide transmission attenuation maps can be used for fully automated 3-D SPECT-CT image registration. Such registration is not affected by features and quality of SPECT images, and avoids difficulties associated with the use of fiducial markers. The technique described in this preliminary work can potentially be extended to SPECT imaging of various organs.

It has been shown in chapter 3 and 5 that attenuation correction using RNT attenuation maps improves homogeneity of radiotracer distribution of an anthropomorphic phantom. Several investigators have found that attenuation correction using RNT attenuation maps have improved interpretation of myocardial perfusion SPECT images [19, 93, 114]. Attenuation maps have also been used in SPECT scatter correction [44, 46]. It has been shown in this thesis that, in addition to such use in non-uniform attenuation correction

and scatter correction, RNT attenuation maps can be applied to automated SPECT-CT image registration. In summary, therefore, use of RNT attenuation maps can improve the interpretation and quantitation of SPECT images. The objectives of this thesis have been fulfilled.

8.2. Future work

8.2.1. Attenuation maps estimated from images acquired in a scatter window

As mentioned above, in the experiments for this dissertation, no background activity was placed in the phantom. If there is no background activity, the images acquired in the scatter window do not indicate the body outline, and they cannot be used to estimate attenuation maps. This is demonstrated in the scatter window images of the phantom shown in Fig. 8.1.

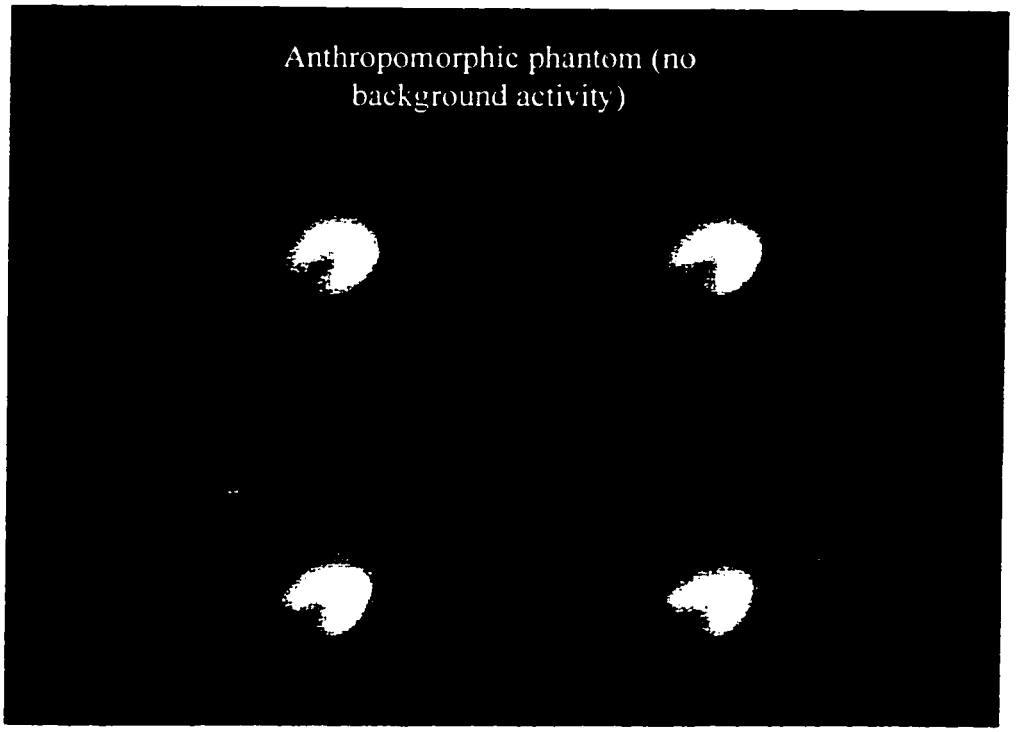

Fig. 8.1. Scatter window images of the anthropomorphic phantom (no background activity).

However, in patients, since there is background activity, the scatter window images indicate a rough body outline, and roughly the position of the lungs. Fig. 8.2 shows Tc-99m sestamibi images acquired in a 20% scatter window centered at 110 keV for a female patient. These images were reconstructed using OSEM and post-reconstruction filtered by a 3-D Butterworth filter (frequency cutoff 0.40 cycles/cm, order 5). The position of the lungs, mediastinum and chest wall can be identified visually. The contours of the breasts, though not as clearly seen laterally, are still visible. Lungs and soft tissue could potentially be delineated either manually or using automatic edge detection. The appropriate attenuation coefficients could be substituted into the segmented image. Pan et al [113] have suggested deforming the boundaries of one patient's transmission map to the current patient's body outline, heart and liver location.

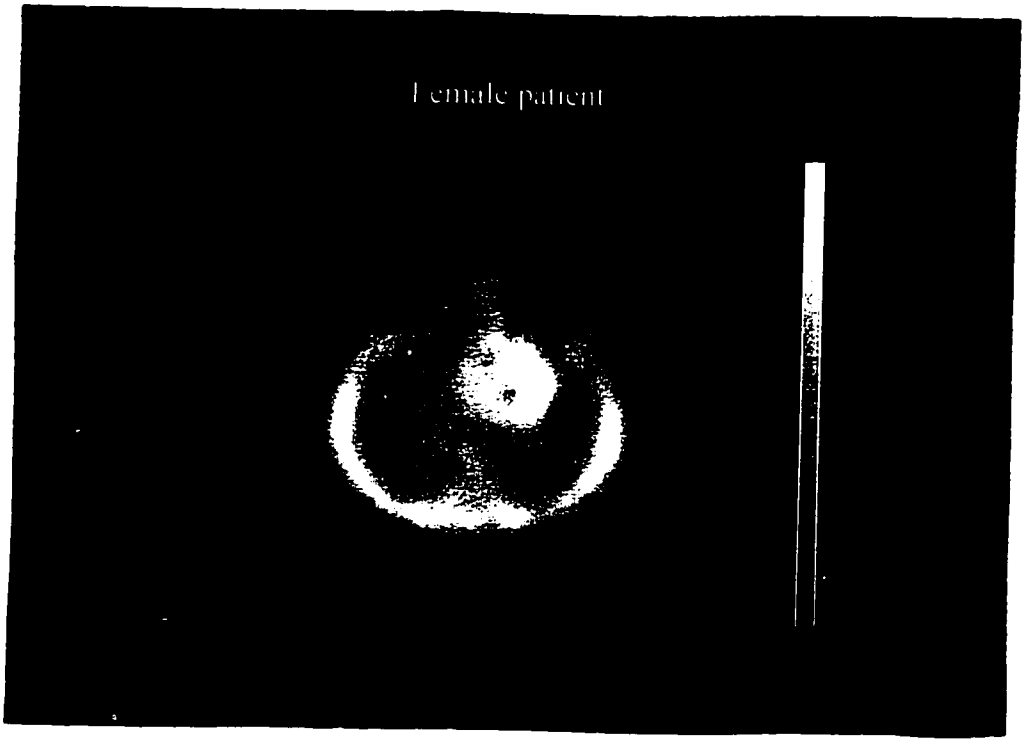

Fig. 8.2. Tc-99m sestamibi scatter window images of a female patient.

Pan et al [113] have estimated attenuation maps from images acquired in a scatter window for 16 Tc-99m sestamibi patients. For one patient, the segmented scatter window attenuation maps have been compared to a transmission attenuation map acquired with a Gd-153 line source and a slant-hole collimator. For Tc-99m, the scatter window is centered between 100-110 keV. If Gd-153 is used, the scatter window and transmission energy windows overlap, and transmission attenuation maps cannot be acquired simultaneously as the scatter window images. However if a lower energy transmission source such as Am-241 is used, the scatter window images could be acquired simultaneously with the RNT maps. For each patient, then, the comparison of attenuation maps estimated from scatter window and conventional RNT attenuation maps could be performed quite easily.

As mentioned in Chapter 3, some manufacturers acquire RNT attenuation maps sequentially, this increases the acquisition time. Using fast transmission and segmentation, the additional time required to perform transmission imaging could be reduced significantly. If fast transmission projections were acquired (for example, over 2-3 minutes) the effect of using segmented fast transmission RNT maps to conventional transmission attenuation maps could be evaluated quite easily.

To evaluate the effect of assigning a uniform linear attenuation coefficient to the lung, lung regions in the transmission attenuation maps can be segmented and filled with a uniform attenuation coefficient corresponding to lung; and the effect of using these segmented attenuation maps can be compared to conventional transmission attenuation maps.

8.2.2. Scatter correction

The scatter correction method used in this dissertation was dual energy window scatter subtraction, where a constant fraction of counts acquired in a scatter window was subtracted from the photopeak projection data. This fraction, k, was taken to be 0.5. The results from Chapter 5 emphasize the need to estimate the scatter fraction more

accurately. Since the images were not acquired in scatter rejection windows on either side of the photopeak, the TEW method cannot be applied for this data.

It has been shown that the scatter contribution per pixel can be modeled by a mathematical function whose parameters can be estimated from transmission attenuation maps [46]. For the anthropomorphic phantom data in this dissertation, RNT attenuation maps are available, and this method can be implemented easily. I expect this scatter correction technique to give better results than dual energy subtraction using a scatter fraction of 0.5.

8.2.3. Comparison of quantitative methods

Automated, direct and voxel-based quantitative methods were used in this dissertation. The defects estimated by region growing could be displayed in 3 orientations directly on the images, or on a composite normal template. From such quantification, for each defect study, quantitative parameters could be calculated; these were defect/normal ARM ratio, maximum defect contrast, and defect volume. These quantitation methods are based on the clinical quantitation package PERFIT [120-121]. PERFIT has been validated for angiographically verified patients, both normal and with coronary artery disease [120-121]. However, results from PERFIT have not yet been compared with conventional polar plot quantitation. The advantage of including the phantom data from this dissertation in such a comparison is that for the phantom, the activity concentration in the defect and normal myocardium, as well as defect volume are known from experiment.

8.2.4. Image registration

The image registration technique using attenuation maps proposed in chapter 7 can potentially be extended to a wide variety of SPECT images. An area of particular interest is intersubject registration of brain SPECT scans to a composite normal database for localization and quantitation of abnormalities. In brain SPECT, a wide range of radiopharmaceuticals are used to obtain 3-D brain images for assessing diseases such as Alzheimer's and Parkinson's disease, depression, head trauma, etc. Although SPECT

images provide physiological information, they frequently lack anatomical details. This is particularly true for newer agents targeting specific brain functions, such as I-123-labelled radiotracers targeting certain dopamine receptors, and showing activity only in the basal ganglia. Currently, the images are assessed visually which results in high intra-observer variability. Subtle changes in image appearance are also often clinically important. One approach to improve the image interpretation is to apply quantitation software which performs 3-D statistical comparisons of individual voxels with a database of normal studies [151]. To perform such comparisons, however, it must be possible to register patient images to common 3-D reference coordinates, sometimes using image warping schemes. Several approaches have been tried, but most of them are specific to a particular type of SPECT scan or require use of external markers or stereotactic frames which may not be clinically feasible. Using commercially available transmission hardware, attenuation maps can be acquired in the same spatial orientation as SPECT. Such attenuation maps can be used in image registration. The method is clinically feasible and can be implemented easily.

I plan to apply image registration using RNT attenuation maps to SPECT images of the brain. I intend to evaluate the intersubject brain SPECT registration using RNT maps for phantoms and for patient data, adopt and further develop current brain quantitation techniques for intersubject registration using RNT maps, evaluate the effect of intersubject warping on both RNT and abnormal SPECT images, and test the fusion of additional MRI/CT images using RNT maps for further improvement of the anatomical reference for SPECT.

REFERENCES

1. Anderson EE. *Introduction to modern physics*. Saunders College Publishing: 1982.
2. Sorenson JA, Phelps ME. *The physics of Nuclear Medicine*. W.B. Saunders Company: 1987.
3. Anger H. Scintillation camera. *Rev Sci Instrum* 1958; 29: 27.
4. Slomka PJ. *Automated analysis of Nuclear Medicine images*. Ph.D. dissertation. University of Western Ontario, London, Canada; 1995.
5. Adams R. The Scintillation gamma camera. In: *Nuclear Medical Physics* (edited: Williams LE). CRC Press Inc. 1987; 2: 89-154.
6. Graham SL. Automatic tuning of scintillation cameras: a review. *J Nucl Med Tech* 1986; 14: 105-110.
7. Simmons GH. On-line correction for factors that affect uniformity and linearity. *J Nucl Med Tech* 1988; 16: 82-89.
8. Rosenfeld A, Kak AC. *Digital picture processing*. Academic Press inc: 1982.
9. Budinger TF, Gullberg GT, Huesman RH. Emission Computed Tomography. In: *Image Reconstruction from projections: Implementations and applications* (edited: Herman GT). Springer-Verlag 1979; 146-246.
10. King MA, Tsui BMW, Pan TS et al. Attenuation compensation for cardiac single photon emission computed tomographic imaging. Part 2. Attenuation compensation algorithms (review). *J Nucl Cardiol* 1996; 3: 55-63.
11. Hutton BF, Hudson HM, Beekman FJ. A clinical perspective of accelerated statistical reconstruction. *Eur J Nucl Med* 1997; 24: 797-808.
12. Shepp LA, Vardi Y. Maximum Likelihood reconstruction for emission tomography. *IEEE Trans Med Imaging* 1982; 1: 113-121.
13. Lange K, Carson R. EM reconstruction algorithms for emission and transmission tomography. *J Comput Assist Tomogr* 1984; 8: 306-316.
14. Hudson HM and Larkin RS. Accelerated image reconstruction using ordered subsets of projection data. *IEEE Trans Med Imag* 1994; 13: 601-609.

15. Tsui BMW, Zhao X, Frey EC et al. Comparison between ML-EM and WLS-CG algorithms for SPECT image reconstruction. *IEEE Trans Nucl Sci* 1991; 38: 1766-1772.

16. Lalush DS, Tsui BMW. A fast and stable maximum a posteriori conjugate gradient reconstruction algorithm. *Med Phys* 1995; 22: 1273-1284.

17. Knesaurek K, Machac J. Non-uniform attenuation correction in SPET using a modified conjugate gradient reconstruction method. *Nucl Med Comm* 1997; 18: 431-436.

18. Fessler JA. Penalized weighted least-squares image reconstruction for positron emission tomography. *IEEE Trans Med Imag* 1994; 13: 290-300.

19. Ficaro EP, Fessler JA, Shreve PD et al. Simultaneous Transmission/Emission myocardial perfusion tomography: Diagnostic accuracy of attenuation-corrected ^{99m}Tc-sestamibi Single Photon Emission Computed Tomography. *Circulation* 1996; 93: 463-473.

20. Llacer J, Veklerov E. Feasible images and practical stopping rules for iterative algorithms for emission and transmission tomography. *IEEE Trans Med Imag* 1987;6: 106-114.

21. Llacer J, Veklerov E, Coakley KJ et al. Statistical analysis of maximum likelihood estimator images of human brain FDG PET studies. *IEEE Trans Med Imag* 1993; 12: 215 – 231.

22. Miller TR, Wallis JW. Clinically important characteristics of maximum-likelihood reconstruction. *J Nucl Med 1992*; 33: 1678-1684.

23. Snyder DL, Miller MI. The use of sieves to stabilize images produced with the EM algorithm for emission tomography. *IEEE Trans Nucl Sci* 1985; 32: 3864-3872.

24. Iida H, Narita Y, Kado H et al. Effects of scatter and attenuation correction on quantitative assessment of regional cerebral blood flow with SPECT. *J Nucl Med* 1998; 39: 181-9.

25. Meikle, SR, Hutton BF, Bailey DL et al. Accelerated EM reconstruction in total-body PET: potential for improving tumour detectability. *Phys Med Biol* 1994; 39: 1689-1704.

26. Byrne CL. Accelerating the EMML algorithm and related iterative algorithms by rescaled block-iterative methods. *IEEE Trans Imag Proc* 1998: 7: 100-9.
27. Tsui BMW, Gullberg GT, Edgerton ER et al. Correction of nonuniform attenuation in cardiac SPECT imaging. *J Nucl Med* 1989; 30: 497-507.
28. Cullom, SJ. Principles of cardiac SPECT. In: *Cardiac SPECT imaging* (edited: DePuey EG, Berman DS, Garcia EV). Lippincott-Raven publishers: 1996; 1-19.
29. Hutton BF. Cardiac single-photon emission tomography: is attenuation correction enough ? (editorial) *Eur J Nucl Med* 1997; 24: 713-715.
30. Chang LT. A method for attenuation correction in radionuclide computed tomography. *IEEE Trans Nucl Sci* 1978; 25; 638-643.
31. Maze A, Le Cloirec J, Collorec R et al. Iterative reconstruction methods for non-uniform attenuation distribution in SPECT. *J Nucl Med* 1993; 1204-1209.
32. Morozumi T, Nakajima M, Ogawa K et al. Attenuation correction methods using the information of attenuation distribution for single photon emission CT. *Med Imaging Technol* 1988; 2: 20-28.
33. Bellini S, Piacentini M, Cafforio C et al. Compensation of tissue absorption in emission tomography. *IEEE Trans Acoust Speech Signal Proc* 1979; 27: 213-218.
34. Tanaka E, Toyama H, Murayama H. Convolution image reconstruction for quantitative single photon emission computed tomography. *Phys Med Biol* 1984; 29: 1489-1500.
35. Jaszczak RJ, Floyd CE, Coleman RE. Scatter compensation techniques for SPECT. *IEEE Trans Nucl Sci* 1985; 32: 786-793.
36. Gagnon D, Todd-Pokropek A, Arsenault A et al. Introduction to holospectral imaging in nuclear medicine for scatter subtraction. *IEEE Trans Med Imag* 1989; 8: 245-250.
37. Mas J, Hannequin P, Ben Younes R et al. Scatter correction in planar imaging and SPECT by constrained factor analysis of dynamic structures (FADS). *Phys Med Biol* 1990; 35: 1451-1465.
38. Buvat I, Benali H, Frouin F et al. Target apex-seeking in factor analysis of medical image sequences. *Phys Med Biol* 1993; 38: 123-128.
39. Koral KF, Wang X, Rogers WL. SPECT Compton scattering correction by analysis of energy spectra. *J Nucl Med* 1988; 29: 195-202.

40. Koral KF, Swailem FM, Buchbinder S et al. SPECT dual-energy-window Compton correction: scatter multiplier required for quantification. *J Nucl Med* 1990; 31: 90-98.

41. Ogawa K, Harata Y, Ichihara T et al. A practical method for position-dependent Compton scatter compensation in single photon emission CT. *IEEE Trans Med Imag* 1991; 10: 408-412.

42. King MA, deVries DJ, Pan TS et al. An investigation of the filtering of TEW scatter estimates used to compensate for scatter with ordered subset reconstructions. *IEEE Trans Nucl Sci* 1997; 44: 1140-45.

43. Ichihara T, Ogawa K, Motomura N et al. Compton scatter compensation using the triple-energy window method for single- and dual-isotope SPECT. *J Nucl Med* 1993; 34: 2216-2221.

44. Narita Y, Eberl S, Iida H et al. Monte Carlo and experimental evaluation of accuracy and noise properties of two scatter correction methods for SPECT. *Phys Med Biol* 1996; 41: 2481-2496.

45. Axelsson B, Msaki P, Israelsson A. Subtraction of Compton-scattered photons in single-photon emission computerized tomography. *J Nucl Med* 1984; 25: 490-494.

46. Meikle SR, Hutton BF, Bailey DL. A transmission dependent method for scatter correction in SPECT. *J Nucl Med* 1994; 35: 360-367.

47. Buvat I, Rodriguez-Villafuerte M, Todd-Pokropek A et al. Comparative assessment of nine scatter correction methods based on spectral analysis using Monte Carlo simulations. *J Nucl Med* 1995; 36: 1476-1488.

48. Glick SJ, Hawkins WG, King MA et al. The effect of intrinsic attenuation correction methods on the stationarity of the 3-D modulation transfer function of SPECT. *Med Phys* 1992; 19: 1105-1112.

49. Knesaurek K, King MA, Glick SJ et al. Investigation of causes of geometric distortion in 180° and 360° angular sampling in SPECT. *J Nucl Med* 1989; 30: 1666-75.

50. Tsui BMW, Hu HB, Gilland DR et al. Implementation of simultaneous attenuation and detector response correction in SPECT. *IEEE Trans Nucl Sci* 1988; 35: 778-783.

51. Glick SJ, Penney BC, King MA et al. Noniterative compensation for the distance dependent detector response and photon attenuation in SPECT imaging. *IEEE Trans Med Imag* 1994; 13: 363-374.

52. Boulfelfel D, Rangayyan RM, Kloiber R. Two-Dimensional Restoration of single Photon Emission Computed Tomography Images Using the Kalman Filter. *IEEE Trans Med Imag* 1994; 13: 102.

53. Larock MP, Braat SH, Sochor H et al. *New developments in myocardial imaging: Technetium 99m-Tc sestamibi.* Martin Dunitz: 1993.

54. Pohost GM, Henzlova MJ. The value of thallium imaging (editorial). *N Engl J Med* 1992; 323:190-192.

55. Maddahi J, Rodrigues E, Kiat H et al. Detection and evaluation of coronary artery disease by Thallium-201 myocardial perfusion scintigraphy. In: *Cardiac SPECT imaging* (edited: DePuey EG, Berman DS, Garcia EV). Lippincott-Raven publishers: 1996; 103 – 120.

56. Leppo JA. Dipyridamole thallium imaging: the lazy man's stress test. *J Nucl Med* 1989; 30: 281-287.

57. Iskandrian A. Adenosine myocardial perfusion imaging. *J Nucl Med* 1994; 35: 734-736.

58. Pennel DJ, Underwood SR, Swanton RH et al. Dobutamine thallium myocardial perfusion tomography. *J Am Coll Cardiol* 1991; 18: 1471-1479.

59. Baim DS. Interventional catheterization techniques. In: *Heart Disease: A textbook of cardiovascular medicine.* Philadelphia: W.B. Saunders Company; 1988: 1379-94.

60. Abrams HL, Adams DF. The coronary arteriogram: structural and functional aspects. *N Engl J Med* 1969; 281: 1276-85.

61. Kennedy JW. Complications associated with cardiac catheterization and angiography. *Cathet Cardiovasc Diagn* 1982; 8:5-11.

62. Berman DS, Kiat H, Maddahi J. The new Tc-99m myocardial perfusion agents: 99-m-Tc-sestamibi and 99-m-Tc-teboroxime. *Circulation* 1991; 84: 17-21.

63. Berman DS, Kiat HS, Van Train KF et al. Myocardial perfusion imaging with technetium-99m-sestamibi: comparative analysis of available protocols. *J Nucl Med* 1994; 35: 681-688.

64. Johnson LL. Myocardial perfusion imaging with technetium-99-m-teboroxime. *J Nucl Med* 1994; 35: 689-92.

65. Berman DS, Kiat H, German G et al. ^{99m}Tc-sestamibi SPECT. In: *Cardiac SPECT imaging* (edited: DePuey EG, Berman DS, Garcia EV). Lippincott-Raven publishers: 1996; 121 – 146.

66. Wackers FJ. Myocardial perfusion imaging. In: *Diagnostic Nuclear Medicine* (edited: Gottschalk A, Hoffer PB, Potchen EJ). Golden's diagnostic radiology: 1988; 291-354.

67. Kiat H, German G, Friedman J et al. Comparative feasibility of separate or simultaneous rest thallium-201/stress technetium-99m dual isotope cardiac SPECT. *J Nucl Med* 1994; 35: 542-548.

68. Heo J, Wolmer I, Kegel J et al. Sequential dual-isotope SPECT imaging with thallium-201 and technetium-99m-sestamibi. *J Nucl Med* 1994; 35: 549-553.

69. Tamaki N, Mukai T, Ishii Y et al. Comparative study of thallium emission myocardial tomography with 180° and 360° acquisition. *J Nucl Med* 1982; 23: 661-666.

70. Maublant JC, Peycelon P, Kwiatkowski F et al. Comparison between 180° and 360° data collection in technetium-99m MIBI SPECT of the myocardium. *J Nucl Med* 1989; 30: 295-300.

71. LaCroix KJ, Tsui BMW, Hasegawa BH. A comparison of 180° and 360° acquisition for attenuated-compensated Thallium-201 SPECT images. *J Nucl Med* 1998; 39: 562-574.

72. Ficaro EP, Pitt SR, Wawrzynski PE et al. Diagnostic accuracy of 180° and 360° reconstructions for uncorrected and attenuation corrected Tc-99m cardiac SPECT. *J Nucl Med* 1996; 37: 81P (abstract).

73. Galt JR, Germano G. Advances in instrumentation for cardiac SPECT. In: *Cardiac SPECT imaging* (edited: DePuey EG, Berman DS, Garcia EV). Lippincott-Raven publishers: 1996; 91-102.

74. ACC/ AHA/ SNM policy statement: standardization of cardiac tomographic imaging. *J Nucl Med* 1992; 33: 1434-35.

75. Slomka PJ, Dey D. Review of instrumentation developments at the SNM 1996 annual meeting. *J Nucl Med* 1996; 37: 25N-33N.

76. DePeuy EG. Artifacts in SPECT myocardial perfusion imaging. In: *Cardiac SPECT imaging* (edited: DePuey EG, Berman DS, Garcia EV). Lippincott-Raven publishers: 1996; 169 – 200.

77. *Radiological health handbook.* Washington: US Dept. Health Education and Welfare 1970; 86-139.

78. King MA, Tsui BMW, Pan TS. Attenuation compensation for cardiac single-photon emission computed tomographic imaging. Part 1. Impact of attenuation and methods of estimating attenuation maps (review). *J Nucl Cardiol* 1995;2:513-524.

79. Eisner RL, Tamas MJ, Cloninger K et al. Normal SPECT thallium-201 bulls'-eye display: gender differences. *J Nucl Med* 1988; 29: 1901-1909.

80. Luo DS, King MA, Morgan HT et al. Investigations into possible causes of hot inferior wall artifacts in attenuation corrected cardiac perfusion images. *IEEE Trans Nucl Sci* 1997; 44: 1146-53.

81. King MA, Xia W, deVries D et al. A Monte Carlo investigation of artifacts caused by liver uptake in single photon emission computed tomography perfusion imaging with technetium 99m-labeled agents. *J Nucl Cardiol* 1996; 3: 18-29.

82. Cooper JA, Neumann PH, McCandless BK. Detection of patient motion during tomographic myocardial perfusion imaging. *J Nucl Med* 1993; 34: 1349-1355.

83. Eisner RL, Noever T, Nowak D et al. Use of cross-correlation function to detect patient motion during SPECT imaging. *J Nucl Med* 1987; 28: 97-101.

84. Mannting F, Mannting MGM. Gated SPECT with technetium-99-m-sestamibi for assessment of myocardial perfusion abnormalities. *J Nucl Med* 1993; 34: 601-608.

85. Germano G, Kiat H, Kavanagh PB et al. Automatic quantification of ejection fraction from gated myocardial perfusion SPECT. *J Nucl Med* 1995;36: 2138-2147.

86. Germano G, Chua T, Kiat H et al. A quantitative phantom analysis of artifacts due to hepatic activity in technetium-99m myocardial perfusion SPECT studies. *J Nucl Med* 1994; 35: 356-359.

87. Eisner RL, Schmarkey LS, Martin SE et al. Defects on SPECT perfusion images can occur due to abnormal segmental contraction. *J Nucl Med* 1994; 35: 638-643.

88. Fleming JS. A technique for using CT images in attenuation correction and quantification in SPECT. *Nucl Med Comm* 1989; 10: 83-97.

89. Hasegawa BH, Lang TF, Brown JK et al. Object-specific attenuation correction of SPECT with correlated dual-energy X-ray CT. *IEEE Trans Nucl Sci* 1993; 40: 1242-1252.

90. LaCroix KJ, Tsui BMW, Hasegawa BH et al. Investigation of the use of X-ray CT images for attenuation compensation in SPECT. *IEEE Trans Nucl Sci* 1994; 41: 2793-2799.

91. Ficaro EP, Fessler JA, Rogers WL et al. Comparison of Americium-241 and Technetium-99m as transmission sources for attenuation correction of Thallium-201 SPECT imaging of the heart. *J Nucl Med* 1994; 35: 652-663.

92. Jaszczak RJ, Gilland DR, Hanson MW et al. Fast transmission CT for determining attenuation maps using a collimated line source, rotatable air-copper-lead attenuators and fan-beam collimation. *J Nucl Med* 1993; 34: 1577-1586.

93. Pruvulovich EM, Lonn AHR, Bomanji JB et al. Effect of attenuation correction on myocardial thallium-201 distribution in patients with a low likelihood of coronary artery disease. *Eur J Nucl Med* 1997; 24: 266-275.

94. Stone CD, McCormick JW, Gilland DR et al. Effect of registration errors between transmission and emission scans on a SPECT system using sequential scanning. *J Nucl Med* 1998; 39: 365-373.

95. Matsunari I, Boning G, Ziegler SI et al. Effects of misalignment between transmission and emission scans on attenuation corrected cardiac SPECT. *J Nucl Med* 1998; 39: 411-416.

96. Tan P, Bailey DL, Meikle SR et al. A scanning line source for simultaneous emission and transmission measurements in SPECT. *J Nucl Med* 1993;34: 1752-1760.

97. Tung CH, Gullberg GT, Zeng GL et al. Nonuniform attenuation correction using simultaneous transmission and emission converging tomography. *IEEE Trans Nucl Sci* 1992; 39: 1134-1143.

98. Datz FL, Gullberg GT, Zeng GL et al. Application of convergent-beam collimation and simultaneous transmission emission tomography to cardiac single photon emission computed tomography. *Sem Nucl Med* 1994; 24: 17-37.

99. Kemp BJ, Prato FS, Nicholson RL et al. Transmission computed tomography of the head with a SPECT system and a collimated line source. *J Nucl Med* 1995; 36: 328-335.

100. Chang W, Loncaric S, Huang G, Sanpitak P. Asymmetrical fan transmission CT on SPECT systems. *Phys Med Biol* 1995; 40: 913-928.

101. Manglos SH, Bassano DA, Thomas FD et al. Imaging of the human torso using cone-beam transmission CT implemented on a rotating gamma camera. *J Nucl Med* 1992; 33: 150-156.

102. Manglos SH, Gagne GM, Bassano DA. Quantitative analysis of image truncation in focal-beam CT. *Phys Med Biol* 1993; 38: 1443-1457.

103. Loncaric S, Chang W, Huang G. Using simultaneous transmission and scatter SPECT imaging from external sources for the determination of the thoracic u-map. *IEEE Trans Nucl Sci* 1994; 41: 1601-1606.

104. Pan TS, King MA, Penney BC et al. Reduction of truncation artifacts in fan-beam transmission by using parallel bean emission data. *IEEE Trans Nucl Sci* 1995; 42: 1310-1320.

105. Gregoriou, GK, Tsui BMW, Gullberg GT. Effect of truncated projections on defect detection in attenuation-compensated fanbeam cardiac SPECT. *J Nucl Med* 1998; 39: 166-175.

106. Tsui BMW, Lewis DP, Lalush DS et al. Reconstruction of truncated projection data from an L-shaped dual detector system for attenuation compensation in myocardial SPECT. *J Nucl Med* 1996; 37: 210P.

107. Celler A, Sitek A, Harrop R. Reconstruction of multiple line source attenuation maps. *IEEE Trans Nucl Sci* 1997; 44: 1503-1508.

108. Cao ZJ, Tsui BMW. Performance characteristics of transmission imaging using a uniform sheet source with a parallel-hole collimator. *Med Phys* 1992; 19: 1205

109. Malko JA, Van Heertum RL, Gullberg GT et al. SPECT liver imaging using an iterative attenuation correction algorithm and an external flood source. *J Nucl Med* 1985; 26: 701-5.

110. Galt JR, Cullom SJ, Garcia EV. SPECT quantification: a simplified method of attenuation and scatter correction for cardiac imaging. *J Nucl Med* 1992; 33: 2232-2237.

111. Madsen MT, Kirchner PT, Edlin JP et al. An emission-based technique for obtaining attenuation correction data for myocardial SPECT studies. *Nucl Med Comm* 1993; 14: 689-95.

112. Wallis, JW, Miller TR, Koppel P. Attenuation correction in cardiac SPECT without a transmission measurement. *J Nucl Med* 1995; 36: 506-12.

113. Pan TS, King MA, Luo DS et al. Estimation of attenuation maps from scatter and photopeak window single photon emission computed tomographic images of technetium 99m-labeled sestamibi. *J Nucl Cardiol* 1997; 4:42-51.

114. Kluge R, Sattler B, Seese A, Knapp WH. Attenuation correction by simultaneous emission-transmission myocardial single-photon emission tomography using a technetium-99m-labelled radiotracer: impact on diagnostic accuracy. *Eur J Nucl Med* 1997;24:1107-1114.

115. Garcia EV, Cooke CD, Van Train KF et al. Technical aspects of myocardial SPECT imaging with Technetium-99m sestamibi. *Amer J of Cardiol* 1990; 66:23E-31E.

116. Garvin AA, Cullom SJ, Garcia EV. Myocardial perfusion imaging using Single-Photon Emission Computed Tomography. *Amer J of Cardiac Imaging* 1994; 8: 189-198.

117. Garcia E, Van Train K, Maddahi J et al. Quantification of rotational thallium-201 myocardial tomography. *J Nucl Med* 1985; 26: 17-26.

118. Van Train KF, Areeda J, Garcia E et al. Quantitative analysis of stress Tl-201 myocardial scintigrams: a multicenter trial validation utilizing standard normal limits. *J Nucl Med* 1986; 27: 17-25.

119. Van Train KF, Areeda J, Garcia E et al. Quantitative same-day rest-stress technetium-99m-sestamibi SPECT: definition and validation of stress normal limits and criteria for abnormality. *J Nucl Med* 1993; 34: 1494-1502.

120. Slomka PJ, Hurwitz GA, Stephenson J et al. Automated alignment and sizing of myocardial stress and rest scans to three-dimensional normal templates using an image registration algorithm. *J Nucl Med* 1995; 36: 1115-1122.

121. Slomka PJ, Hurwitz GA, St. Clement G et al. Three-dimensional demarcation of perfusion zones corresponding to specific coronary arteries: application for automated interpretation of myocardial SPECT. *J Nucl Med* 1995; 36:2120-2126.

122. Slomka PJ, Hurwitz GA, Stephenson J et al. A volume-based image registration toolkit for automated comparison of paired nuclear medicine images. *Med Phys* 1995; 22:1017 (abstract).

123. Dey D, Slomka PJ, Hahn LJ et al. Application of radionuclide transmission computed tomography attenuation maps in automatic three-dimensional multimodality image registration. *J Nucl Med*, submitted.

124. Alpert NM, Bradshaw JF, Kennedy D et al. The principal axes transform – a method for image registration. *J Nucl Med* 1990; 31:626-633.

125. Press WH, Teukolsky SA, Vetterling WT et al. *Numerical recipes in C*, 2nd edition. New York: Cambridge University Press; 1992; 408-412.

126. Goodsitt M. Beam hardening errors in post-processing dual energy quantitative computed tomography. *Med Phys* 1995; 22: 1039-1047.

127. Hahn LJ, Swerhone D, Kloiber RK. Fast sequential fan-beam transmission CT using a collimated line source and uncollimated rotating single head gamma camera. *Eur J Nucl Med* 1994; 21(10): S137 (abstract).

128. National Electrical Manufacturers Association. Performance measurements of scintillation cameras. *National Electrical Manufacturers Association* 1986.

129. Xu EZ, Mullani NA, Gould KL et al. A segmented attenuation correction for PET. *J Nucl Med* 1991; 32: 161-165.

130. Meikle SR, Dahlbom M, Cherry SR. Attenuation correction using count-limited transmission data in positron emission tomography. *J Nucl Med* 1993; 34: 143-150.

131. Tung C, Gullberg GT. A simulation of emission and transmission noise propagation in cardiac SPECT imaging with non-uniform attenuation correction. *Med Phys* 1994; 21: 1565-1576.

132. Van den Elsen P, Pol EJ, Viergiver MA. Medical image matching – a review with classification. *IEEE Eng Med Biol* 1993; 3: 26-39.

133. Weber DA, Ivanovic M. Correlative image registration. *Semin Nucl Med* 1994; 24: 311-23.

134. Schad LR, Boesecke R, Schlegel W et al. Three-dimensional image correlation of CT, MR and PET studies in radiotherapy treatment planning of brain tumors. *J Comput Assist Tomogr* 1987; 11: 948-54.

135. Zhang J, Levesque MF, Wilson CL et al. Multimodality imaging of brain structures for stereotactic surgery. *Radiol* 1990; 175: 435-41.

136. Henri CJ, Collins DL, Peters TM. Multimodality image integration for stereotactic surgical planning. *Med Phys* 1991; 18: 167-177.

137. Kramer EL, Noz ME, Sanger JJ et al. CT-SPECT fusion to correlate radiolabeled monoclonal antibody uptake with abdominal CT findings. *Radiology* 1989; 172: 862-865.

138. Pelizzari CA, Chen GTY, Spelbring DR, Weichselbaum RR, Chen CT. Accurate three-dimensional registration of CT, PET, and/or MR images of the brain. *J Comput Assist Tomogr* 1989; 13: 20 - 26.

139. Pereault C, Schvartz C, Wampach H, Liehn JC, Delisle MJ et al. Thoracic and abdominal SPECT-CT image fusion without external markers in endocrine carcinoma. *J Nucl Med* 1997; 38: 1234-1242.

140. Yu JN, Fahey FH, Gage HD, Edes CG, Harkness BA, Pelizzari CA et al. Intermodality retrospective image registration in the thorax. *J Nucl Med* 1995; 36: 2333-2338.

141. Woods RP, Mazziotta JC, Cherry SR. MRI-PET registration with automated algorithm. *J Comput Assist Tomogr* 1993; 17: 536-546.

142. Maes F, Collignon A, Vandermeulen D et al. Multimodality image registration by maximization of mutual information. *IEEE Trans Med Imag* 1997; 16: 187-198.

143. Collins DL, Neelin P, Peters TM, Evans AC. Automatic 3D intersubject registration of MR volumetric data in standardized Talairach space. *J Comput Assist Tomogr* 1994; 18: 192-205.

144. Pallotta S, Gillardi MC, Bettinardi V et al. Application of a surface matching image registration technique to the correlation of cardiac studies in positron emission tomography by transmission images. *Phys Med Biol* 1995; 40: 1695–1708.

145. Bacharach SL, Douglas MA, Carson RE et al. Three-dimensional registration of cardiac positron emission tomography attenuation scans. *J Nucl Med* 1993; 34: 311-321.

146. Strother SC, Anderson JR, Xu XL et al. Quantitative comparisons of image registration techniques based on high resolution MRI of the brain. *J Comput Assist Tomogr* 1994; 18: 954-962.

147. Turkington TG, Jaszczak RJ, Pelizzari CA et al. Accuracy of registration of PET, SPECT and MR images of a brain phantom. *J Nucl Med* 1993; 34: 1587-1594.

148. Holman BL, Zimmermann RL, Johnson KA et al. Computer-assisted superimposition of magnetic resonance and high resolution Technetium-99m-HMPAO and Thallium-201 SPECT images of the brain. *J Nucl Med* 1991; 32: 1478-1484.

149. Faber TL, Stokely EM. Orientation of 3-D structures in medical images. *IEEE Trans Pat Anal and Mach Intel* 1988; 10: 626-633.

150. Pfluger T, Vollmar C, Tatsch K et al. 3D image fusion (MR Imaging/ SPECT) of the brain: assessment of the registration error of 3 different matching algorithms. *Radiology* 1997; 205(P): 440 (abstract).

151. Radau PE, Slomka PJ, Julin P, Hurwitz GA. Automated alignment and quantitative analysis of brain studies utilizing the clinical software BRASS. *Eur J Nucl Med* 1997; 24: 900 (abstract).

152. Ichise M, Ballinger JR, Vines D et al. Simplified quantification and reproducibility studies of dopamine D2-receptor binding with iodine-123-IBF SPECT in healthy subjects. *J Nucl Med* 1997;38:31-37.

153. Tihonen J, Kuikka J, Bergstrom K et al. Altered striatal dopamine re-uptake site densities in habitually violent and non-violent alcoholics. *Nature Medicine* 1995; 1: 654-657.

IMAGE EVALUATION TEST TARGET (QA-3)

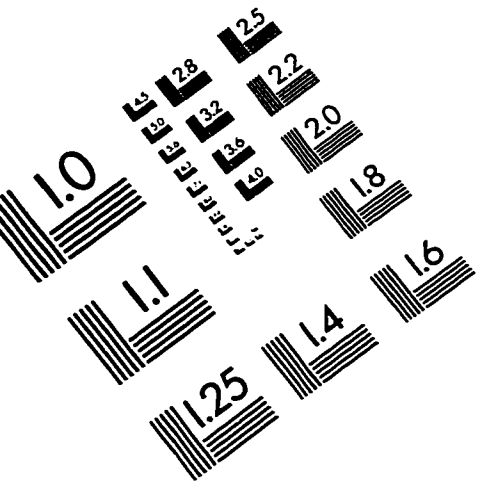

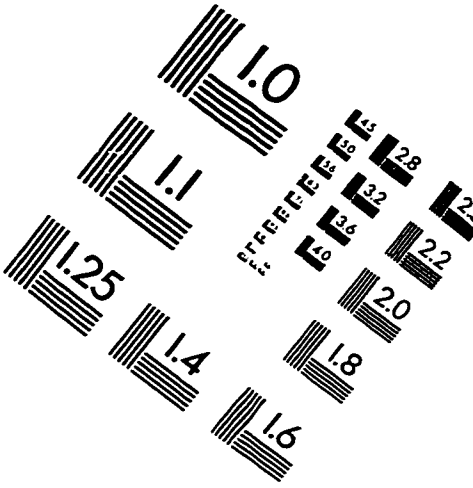

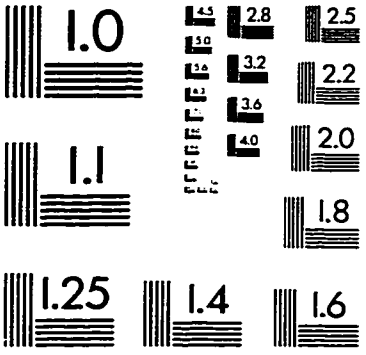

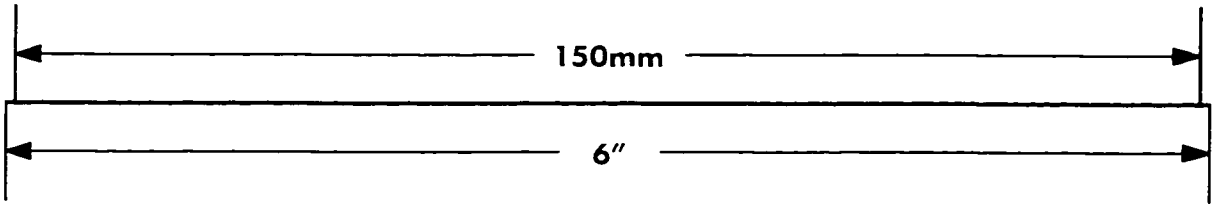

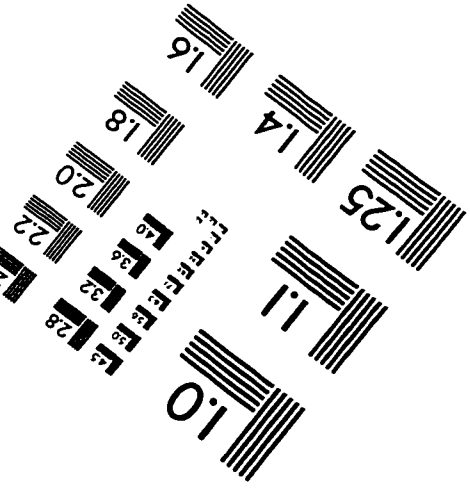

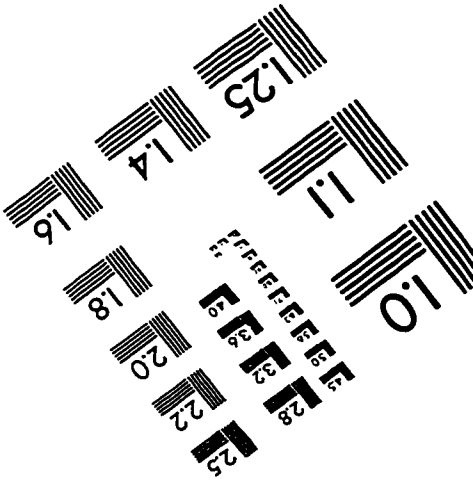

APPLIED IMAGE, Inc
1653 East Main Street
Rochester, NY 14609 USA
Phone: 716/482-0300
Fax: 716/288-5989